Dynamic Contrast-Enhanced MR Microscopy: Functional Imaging in Preclinical Models of Cancer

by

Ergys Subashi

Graduate Program in Medical Physics
Duke University

Date:_____

Approved:

_____
G. Allan Johnson, Supervisor

_____
Bastiaan Driehuys

_____
David Kirsch

_____
James MacFall

_____
Timothy Turkington

Dissertation submitted in partial fulfillment of the requirements for the degree of Doctor of Philosophy in the Graduate Program in Medical Physics in the Graduate School of Duke University

2014

ABSTRACT

Dynamic Contrast-Enhanced MR Microscopy: Functional Imaging in Preclinical Models of Cancer

by

Ergys Subashi

Graduate Program in Medical Physics
Duke University

Date:_____

Approved:

_____
G. Allan Johnson, Supervisor

_____
Bastiaan Driehuys

_____
David Kirsch

_____
James MacFall

_____
Timothy Turkington

An abstract of a dissertation submitted in partial fulfillment of the requirements for the degree of Doctor of Philosophy in the Graduate Program in Medical Physics in the Graduate School of Duke University

2014

Abstract

Dynamic contrast-enhanced (DCE) MRI has been widely used as a quantitative imaging method for monitoring tumor response to therapy. The pharmacokinetic parameters derived from this technique have been used in more than 100 phase I trials and investigator led studies. The simultaneous challenges of increasing the temporal and spatial resolution, in a setting where the signal from the much smaller voxel is weaker, have made this MR technique difficult to implement in small-animal imaging.

This dissertation describes and compares a family of high spatiotemporal resolution methods referred to as DCE magnetic resonance microscopy (DCE-MRM). An interleaved 3D radial trajectory with a quasi-uniform distribution of points in k-space is used for sampling temporally resolved volumes. The effect of the acquisition on spatial and temporal resolution is studied in phantoms and in vivo. The statistical variation of the DCE-MRM measurement is further analyzed by considering the fundamental sources of error in the MR signal. The technique is applied for measuring the extent of the opening of the blood-brain barrier in a mouse model of pediatric glioma and for identifying distinctive regions of therapeutic effect in a model of colorectal adenocarcinoma.

It is shown that 4D radial keyhole imaging does not degrade the system spatial and temporal resolution at a cost of 20-40% decrease in signal-to-noise ratio. The

concentration of the contrast agent, measured in-vitro and in-vivo, is within the theoretically predicted limits. The uncertainty in measuring the pharmacokinetic parameters is of the same order, but always higher than, the uncertainty in measuring the pre-injection longitudinal relaxation time ($T1_0$). The histogram of the time-to-peak (TTP) provides useful knowledge about the spatial distribution of microvascular density and permeability. Two regions with distinct kinetic parameters are identified by setting a threshold on the TTP map. The effect of bevacizumab, as measured by a decrease in microvascular permeability, is confined to one of these regions. DCE-MRM studies contribute unique insights into the response of the tumor microenvironment to therapy.

To Behije and Oli

Table of Contents

List of Tables

List of Figures

List of Abbreviations

1-,2-,3-,4-D	1,2,3,4 Dimensional
AIF	Arterial Input Function
AUC	Area Under the Curve
BBB	Blood-Brain Barrier
BW	Bandwidth
CA	Contrast Agent
CIVM	Center for In Vivo Microscopy
CNS	Central Nervous System
CT	Computed Tomography
DAM	Double Angle Method
DCE	Dynamic Contrast-Enhanced
DCF	Density Compensation Factor
DIPG	Diffuse Intrinsic Pontine Glioma
EES	Extravascular-Extracellular Space
FA, α	Flip Angle
FFT	Fast Fourier Transform
FID	Free Induction Decay
FOV	Field of View

FT	Fourier Transform
H&E	Hematoxylin and Eosin
HGG	High Grade Glioma
IP	Intraperitoneal
MR	Magnetic Resonance
MRI	Magnetic Resonance Imaging
MRM	Magnetic Resonance Microscopy
N_B	Number of Baselines
NEX (NA)	Number of Excitations (Averages)
NMR	Nuclear Magnetic Resonance
PDF	Probability Distribution Function
PET	Positron Emission Tomography
pHGG	Pediatric High Grade Glioma
PSF	Point-Spread Function
QIBA	Quantitative Imaging Biomarker Alliance
RARE	Rapid Acquisition with Relaxation Enhancement
RF	Radiofrequency
ROI	Region of Interest
RSNA	Radiological Society of North America

SE	Spin Echo
SI	Signal Intensity
SNR	Signal-to-Noise Ratio
SPECT	Single Photon Emission Computed Tomography
SPGR	Spoiled Gradient-Recalled
TE	Echo Time
TP	Time Point
TR	Repetition Time
TTP	Time to Peak
Tx	Treatment
UFC	Uniform Frequency Cutoff
UND	Undersampled
UTE	Ultra Short Echo
VEGF	Vascular Endothelial Growth Factor
VFA	Variable Flip-Angle
VFC	Variable Frequency Cutoff
WIS	Wash-in Slope
WOS	Wash-out Slope
WT	Wild-Type

Acknowledgments

"You got to know when to hold 'em, know when to fold 'em, know when to walk away, know when to run…" That's how my Ph.D. advisor, **Dr. G. Allan Johnson**, responded to one of my questions during our weekly meeting. And he sang it loudly! My feelings of gratitude towards Al are composed of much finer distinctions than my vocabulary has room for. If I attempted to provide a list, I fear I might quickly reach the incomplete set. It has been a privilege to be part of the team of people at the Center for In Vivo Microscopy. Al's foresight, encouragement, and enthusiasm have shaped me into a better researcher, team player, colleague, and teacher. No book can teach such things.

I am especially thankful to **Dr. Yi Qi** for her continuous teachings and insight. My dissertation research would not have been possible without Yi's care and work ethic. Our collaboration has taught me the importance of discipline and attention to detail. Through Yi, I experienced firsthand the quality of work achieved only when one deeply loves what they are doing.

I am also grateful to my committee members, **Dr. Bastiaan Driehuys**, **Dr. David Kirsch**, **Dr. James MacFall**, and **Dr. Timothy Turkington** for their guidance and support. I would not be at this point in my graduate career were it not for their dedication and commitment to create the best environment for students to thrive.

I am thankful for several collaborative projects related to my dissertation work. In particular, I would like to gratefully acknowledge the help of **Dr. Kingshuk Choudhury**, **Dr. Oren Becher**, **Everett Moding**, and **Francisco Cordero**. The opportunity to discuss my research with scientists in other fields has broadened my perspective and taught me how to be a careful listener and critical thinker.

The faculty and staff of CIVM reserve a special place in my heart and memories. Thank you for the fun, the challenge, and the affection. I am just beginning to understand how precious this environment has been in my training. Thank you **Tawynna Gordon**, **Lucy Upchurch**, and **Sally Zimney** for your thoughtful suggestions, for making my life more organized, and for yelling at me when I made a mess. I apologize for all the times I have been a headache and hope you know that I truly cherish every moment together. I am also grateful to **James Cook** for helping me deal with painful debugging problems and to **Gary Cofer**, **Dr. John Nouls**, **Dr. Zackary Cleveland**, **Dr. Cristian Badea**, **Dr. Alexandra Badea**, and **Dr. Laurence Hedlund** for technical advice and practical wisdom.

I will always treasure my friendship with current and past students at Duke, especially **Prachi Pandit**, for wise words, breathtaking jokes, (un)necessary details about healthy food (and its iron content), and for being a wonderful triathlon training partner, **Samuel Johnston**, **Evan Calabrese**, **Matthew Freeman**, **Sivaram Kaushik**, and **Rohan**

Virgincar for the laughs, the sports, and the beers, and **Luke Xie**, **Darin Clark**, **Russell Dibb**, and **Scott Robertson** for stimulating discussions and insight. The wisdom of **Lee Stunja**, **Jered Wells**, and **Ross McGurk** remains an inspiration at every crossroad in my life. I am deeply grateful to **Darlena Kern** for her heartening enthusiasm, caring encouragement, and love for ice cream. Thank you for all the timeless memories.

I feel eternally indebted to my **mom**, my **dad**, **Oli**, **Hasan Subashi, Ellen Bergman**, **Melanie Helm**, and **Karl Bergman**. I treasure your love in ways that words cannot describe and hope to be as precious to you as you are to me. No matter where the future takes me, I will carry deep in my heart your devotion, care, and encouragement.

Ergys Subashi
Duke University
June 2014

1. Introduction

1.1 Motivation

Cancer is the leading cause of mortality and has the highest economic impact worldwide due to premature death and disability (John and Ross 2010). The emotional stress and anxiety following the diagnosis with this disease affect the patient, family members, and the community at-large in immeasurable ways. However, research in basic and applied sciences has led to a rapid increase in our understanding of cancer biology and consequently in the number of therapies available to the patient (Stevens, Jensen et al. 2011). In the past decade, the 5-year survival rate has drastically increased for virtually every type of cancer diagnosed in the western industrialized countries (Verdecchia, Francisci et al. 2007).

The advancements in biomedical sciences in general, and cancer biology in particular, would have been technically impossible without the use of small animals as research models. It is known from comparative genomics that any mammal may be used as such a model since the genetic content has only had minute changes during the era of mammalian evolution (Paigen 1995). But the technical and practical advantages of handling, maintaining, grooming, and cost have made the laboratory mouse and rat by far the most common experimental research species in the biosciences. The complete map of the genome of the laboratory mouse (Chinwalla, Cook et al. 2002), the laboratory

rat (Jacob, Brown et al. 1995), and of the anatomy of their respective brains (Johnson, Badea et al. 2010; Johnson, Calabrese et al. 2012) are some of the major breakthroughs reflecting the importance of these two species as research models in the preclinical domain.

Magnetic resonance imaging (MRI) has become one of the most powerful research and clinical tools in scientific fields ranging from physics to biology, psychology to economics, and radiology to neurology. The soft tissue contrast achieved without the use of ionizing radiation, and the availability of pulse-sequences exploiting various contrast mechanisms inherent in living tissue, have made the use of MR images invaluable in the clinical domain. Furthermore, research in small animal models has been revolutionized by pioneering work in magnetic resonance microscopy and histology (Eccles and Callaghan 1986; Johnson, Benveniste et al. 1993) which gave rise to a new paradigm in the biomedical sciences. These techniques are of critical importance to the cancer research community where it has become increasingly more evident that the study of histologically and genetically accurate models of human tumors is only possible in vivo (Becher and Holland 2006). Therefore, novel MR methods that provide precise measurements of heterogeneity in the tumor microenvironment would undoubtedly accelerate research and may provide crucial information about cancer biology and pharmacology.

1.2 Background: Functional Imaging

Functional imaging, in the context of in vivo cancer imaging, can be defined as a set of techniques involving one or more modalities used to study physiologic processes in tumors. Depending on the modality and specific method, the "function" imaged may be: perfusion (blood flow), water diffusion, temperature, rate of transport across the endothelium barrier, volume of extravascular-extracellular space, volume of plasma space, acidity (pH), partial oxygen pressure, and blood pressure. Tumor functional studies are generally not possible in vitro and are complementary to immunohistochemical and morphological studies.

1.2.1 Dynamic MRI in oncology

Dynamic contrast-enhanced MRI is subdivided into two broad methods able to measure the time dependent concentration of an injected contrast agent as it permeates the tissue of interest. The essential difference between these techniques lies in the weighting mechanism used to generate image contrast. Susceptibility based methods, known as dynamic susceptibility contrast-enhanced (DSC) MRI, employ T2 or T2* weighted imaging sequences able to detect a decrease in signal intensity in regions of contrast flow. Microscopic gradients caused by the compartmentalization of the contrast agent in blood vessels (Villringer, Rosen et al. 1988) lead to a large reduction in signal intensity in T2 (T2*)-weighted images making DSC-MRI one of the most common

methods for measuring perfusion and perfusion-related parameters. A typical DSC-MRI perfusion study can provide estimates of absolute blood flow (in units of ml/s), blood volume (ml), and average time for contrast to pass through the vascular network (mean transit time, in units of seconds). In humans, first-pass hemodynamic phenomena have a temporal range of a few seconds (Padhani and Husband 2001) necessitating the use of pulse sequences with acquisition times not higher than $1 - 2$ sec.

Relaxivity based methods, referred to as dynamic relaxivity contrast-enhanced (DRCE) or simply as dynamic contrast-enhanced (DCE) MRI, employ T1-weighted imaging sequences able to detect an increase in signal intensity in regions of contrast accumulation. Dipole-dipole interactions between contrast agent and nearby water molecules lead to a reduction in T1, making DCE-MRI a unique technique for measuring exchange rates between compartments with concentration gradients. A typical DCE-MRI study would provide estimates of the rate of transport of the contrast agent across the endothelium barrier (in units of ml/s), volume of extravascular-extracellular space (ml), and volume of plasma space (ml). The signal intensity changes related to contrast exchange kinetics vary extensively among tumors and are known to have a temporal range in the order of minutes (Padhani and Husband 2001; Subashi, Moding et al. 2013). This allows for a relaxation of the requirement for high temporal resolution acquisitions (as needed for perfusion studies) and provides an opportunity for implementing

sampling techniques with wider coverage and increased spatial resolution. Figure 1 shows representative signal intensity curves in three regions of interest (ROI) in a sarcoma induced in the leg of a mouse. ROI-2 represents a fast enhancing region, while ROI-1 and ROI-3 represent slow enhancing regions with different amplitudes and areas under the curve. The temporal evolution of the concentration of the contrast agent is subsequently fitted with a pharmacokinetic model outputting a set of parameters related to physiologic processes.

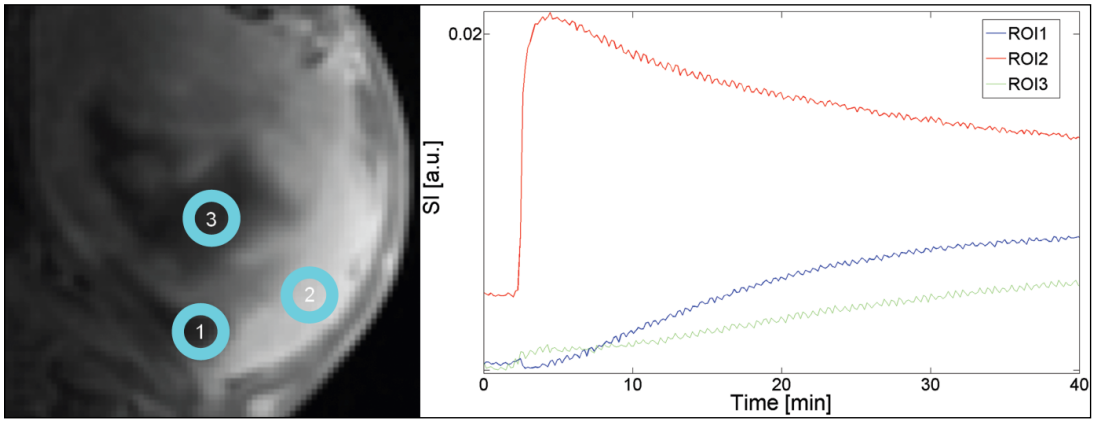

Figure 1: Representative signal intensity vs. time curves from a DCE-MRI study of a primary sarcoma.

Kermode and Tofts (Kermode, Tofts et al. 1988) published the first attempts at quantitative dynamic MRI more than twenty years ago. Since then, this imaging technique has found a wide range of applications in clinical and preclinical research, drug development, and clinical practice. In particular, the recognition that anti-angiogenic compounds may have crucial therapeutic implications in all solid neoplasms

(Folkman 1971) sparked the development of methods for measuring changes in neovascularization in vivo.

In the clinical domain, more than 100 phase I trials and investigator led studies of anti-angiogenic and vascular-disrupting therapeutic agents have incorporated the functional parameters from DCE-MRI as end-points in their protocols (O'Connor, Jackson et al. 2012). These functional parameters were applied to studies of cerebral (Zhu, Li et al. 2000), breast (Matsubayashi, Matsuo et al. 2000), cervical (Yamashita, Baba et al. 2000), prostate (Engelbrecht, Huisman et al. 2003), musculoskeletal (Geirnaerdt, Hogendoorn et al. 2000), and liver (Jayson, Zweit et al. 2002) tumors. The need for meaningful statistical comparisons across measurements from groups using different scanners and imaging protocols has led to the creation of the Quantitative Imaging Biomarker Alliance (QIBA) of the Radiological Society of North America (RSNA). QIBA combined the experience and expertise of clinical researchers, healthcare professionals, and industry representatives in the compilation of a set of guidelines for DCE-MRI acquisition parameters and data analysis (RSNA 2012). Table 1 summarizes the recommendations of this committee for clinical studies of novel therapeutic agents using the biomarkers from DCE-MRI to measure drug efficacy.

Table 1: Recommendations of the RSNA technical committee for DCE-MRI experiments in clinical studies

Pulse sequence	Spoiled Gradient-Recalled Echo (or equivalent)
Dimension	3D
Coils	Transmit: volume coil, Receive: volume/array coil
Resolution (in-plane)	1-2 mm
Slice thickness (mm)	< 5 (ideal), 5.1-6.0 (target), 6.1-8.0 (acceptable)
Number of slices	≥ 10
Temporal resolution	< 10 sec
TR (ms)	< 3 (ideal), 3-5 (target), 5-7 (acceptable)
TE (ms)	< 1.5 (ideal), 1.5-2.0 (target), 2.0-2.5 (acceptable)
FA (deg)	25-35 (to minimize saturation effects and SAR)
Bandwidth (kHz)	≥ 31.25 kHz (or ~250 Hz/pixel)

1.2.2 DCE-MRI in preclinical studies

The mouse is 3000 times smaller than the human, has a heart rate of approximately 6 times higher ($450 - 600$ bpm in mice vs. $80 - 100$ bmp in humans), and a total blood volume not more than approximately 2 ml. The simultaneous challenges of increasing the temporal and spatial resolution, in a setting where the signal from the much smaller voxel is weaker, have made the implementation of DCE-MRI exceedingly difficult in small animals. To date, no unified protocol exists for the execution of such an experiment in the preclinical domain. Table 2 lists the relevant imaging parameters from a survey of recent work employing DCE-MRI to measure the exchange properties of tumor vasculature. Despite the wide variability in acquisition techniques, it is remarkable that these studies have revealed a similar effect from anti-angiogenic and

vascular-disrupting agents on the kinetic parameters measured with dynamic contrast-enhanced MRI (Barnes, Whisenant et al. 2012).

Table 2: Dynamic contrast-enhanced MRI in preclinical studies from a survey of literature published in 2011. Notice the variability in field strength, dimensionality, voxel size, and temporal resolution.

Year	Ref.	Field (B_0)	2D/3D	Voxel Size [mm^3]	Volume [nL]	Temporal Resolution [sec]
2011	(Casneuf, Delrue et al. 2011)	1.5T	2D	5.0x0.5x0.5	1250	1.1
2011	(Loveless, Halliday et al. 2012)	7.0T	2D	2.0x0.39x0.39	304	1.5
2011	(Watson, Hu et al. 2011)	1.5T	2D	2.0x0.31x0.31	192	3.0
2011	(Farrar, Kamoun et al. 2011)	9.4T	2D	0.5x0.2x0.2	20	4.8
2011	(Braren, Altomonte et al. 2011)	1.5T	2D	2.0x0.8x0.8	1280	6.0
2011	(Egeland, Gaustad et al. 2011)	1.5T	2D	2.0x0.23x0.47	216	14.0
2011	(Gulliksrud, Øvrebø et al. 2011)	1.5T	2D	2.0x0.31x0.31	192	14.0
2011	(Farace, Merigo et al. 2011)	4.7T	3D	1.5x0.23x0.23	79	102.0
2011	(Plaks, Sapoznik et al. 2011)	4.7T	3D	0.68x0.39x0.39	103	163.0
2011	(Aychek, Vandoorne et al. 2011)	9.4T	3D	0.62x0.31x0.31	60	163.0

In preclinical studies, DCE-MRI has been used almost exclusively as a functional imaging tool for measuring therapeutic response in human tumor models. The study of the effect of neovascularization on neoplasm growth has led to a shift in the paradigm for cancer treatment (Weis and Cheresh 2011). The biomarkers from DCE-MRI have been applied in the evaluation of vascular-inhibiting drugs (Maxwell, Wilson et al. 2002), anti-angiogenic agents, and a combination of radiation and anti-angiogenic therapies (Chung, Jalali et al. 2013; Jalali, Chung et al. 2014). In rats, Maxwell et al. reported a three- and a five-fold decrease in mean permeability 6 hours after the administration of respectively 10 mg/kg and 100 mg/kg of a vascular-inhibiting agent. In mice, Checkley et al. found a dose-dependent decrease immediately after the administration of an angiogenesis inhibitor. Chung et al. observed a decrease of 26% in mean permeability with a combination of radiation and anti-angiogenic therapies. These findings are analogous to those in human studies where it is unequivocally known that permeability/perfusion decreases after therapy (O'Connor, Jackson et al. 2012).

1.2.3 Alternative techniques for tumor functional imaging

The growth of solid tumors beyond 1-2 mm^3 is always dependent on their ability to recruit new vasculature (Folkman 1971). In neoplasms of this volume, passive diffusion of oxygen and nutrients is not enough for further cell division. The phenomenon of neovascularization is known as angiogenesis. One of the earliest

identified biomolecules able to stimulate endothelial cell proliferation is the vascular endothelial growth factor (VEGF) (Ferrara and Henzel 1989). The discovery of this potent growth factor quickly led to the search for an antagonist agent able to block tumor-induced angiogenesis, hence limiting the amount of oxygen and nutrient supply. Shortly thereafter, the VEGF monoclonal antibody A4.6.1 was isolated in mice (Kim, Li et al. 1992) and its therapeutic potential shown in human cancer xenografts (Kim, Li et al. 1993). Early preclinical experiments on the use of A4.6.1 as a therapeutic agent focused on tumor size, weight, and vascular density as measured in histology slides (Gerber and Ferrara 2005). The humanized version of A4.6.1, known as bevacizumab (trade name Avastin, Genentech, San Francisco, CA), has been approved as a clinical therapeutic agent for several tumors.

The vast majority of studies of the pharmacological properties of anti-angiogenic and vascular-disrupting therapies have incorporated one or more biomarkers from immunohistochemical assays: cell density (Rubenstein, Kim et al. 2000), mitotic index in tumor and endothelial cells (Borgström, Hillan et al. 1996), apoptotic index in tumor and endothelial cells (Klement, Baruchel et al. 2000), Matrigel invasion assay (Sweeney, Miller et al. 2001), and microvessel density (Hotz, Hines et al. 2003). Surrogate biomarkers, such as ascites formation (Mesiano, Ferrara et al. 1998), metastatic potential (Melnyk, Zimmerman et al. 1999), interstitial fluid pressure (Boucher, Leunig et al. 1996),

and serum concentration of therapeutic agent (Mordenti, Thomsen et al. 1999) are commonly reported as well. In vivo measurements are acquired with: (a) optical imaging techniques in dorsal skinfold chamber implants and include vascular permeability and vessel diameter (Yuan, Chen et al. 1996), partial oxygen pressure (Lee, Heijn et al. 2000), and acidosis (Fukumura, Xu et al. 2001); (b) positron emission tomography (PET) for VEFG binding sites (Collingridge, Carroll et al. 2002) ; (c) single photon emission computed tomography (SPECT) for VEGF receptor sites (Backer, Levashova et al. 2007); (f) dynamic contrast-enhanced computed tomography (Stantz, Cao et al. 2011); (e) and ultrasonography (Korpanty, Carbon et al. 2007). Table A.1 provides a detailed review of tumor cell lines, site of implantation, therapeutic modality, endpoints, and noteworthy observations, for preclinical studies of the effect of anti-angiogenic agents.

1.3 Specific Aims

The goal of my dissertation research was to develop an accurate and efficient imaging method for functional imaging of tumor growth and therapeutic response in preclinical models of cancer. The driving premises of my work were the following:

- The complex heterogeneity in tumor tissue can only be probed with high spatial/temporal resolution imaging sequences; limited resolution and coverage in most small animal studies leads to incomplete and erroneous results.

- All functional parameters extracted from pharmacokinetic models are necessary and need to be analyzed in concert: no single parameter provides by itself a complete description of the tumor microenvironment.

My dissertation work was subdivided into four main stages:

Stage 1: Acquisition and Reconstruction. The main focus of my work was the development, implementation and optimization of a sampling and reconstruction technique for dynamic contrast-enhanced MRI. The requirement for high accuracy necessitates full coverage of the tissue of interest and high spatial/temporal resolution; we refer to such acquisitions as dynamic contrast-enhanced magnetic resonance microscopy (DCE-MRM). DCE-MRM was implemented as a 4D imaging sequence by exploiting the geometric properties of a 3D Archimedean spiral as a sampling strategy, combined with keyhole reconstruction for decreased acquisition times.

Stage 2: Validation. A volumetric dynamic imaging sequence with high spatiotemporal resolution raises three fundamental questions when keyhole techniques are used in reconstruction:

1) How does keyhole reconstruction affect spatial resolution?
2) What is the effect on temporal resolution?
3) What is the effect on image quality and biomarker estimation?

These questions were answered through a series of simulations, imaging studies in geometric and high resolution phantoms, and in vivo kinetic studies of tumors. Phantom experiments determined the effect on image quality and spatial resolution by measuring: **a)** changes in the signal-to-noise ratio (SNR), **b)** artifacts throughout the field of view (FOV), **c)** distortions in simple geometric shapes (circles, rectangles, and meshgrids), and **d)** spatial resolution as determined by the ability of the final reconstruction to resolve a meshgrid with spacing equal to the Nyquist distance. In vivo studies in different tumors with varying rates of contrast enhancement determined the effect of keyhole reconstruction on temporal resolution. Finally, the statistical variation of the pharmacokinetic parameters measured with DCE-MRM was determined through numerical simulations. The probability density function of these measures was estimated by analyzing the fundamental sources of error in the MR signal acquired with the spoiled gradient-echo (SPGR) pulse sequence.

Stage 3: DCE-MRM as a measure of blood-brain barrier permeability in a preclinical model of glioma. Pediatric high-grade gliomas (pHGGs) occur with strikingly different probabilities in infratentorial and supratentorial regions. Although histologically these malignancies appear similar, they represent distinct diseases. Recent genomic studies have identified histone K27M H3.3/H3.1 mutations in the majority of brainstem gliomas; these mutations are rarely encountered in cortical pHGGs. Clinical work suggests a

restricted permeability of the blood-brain-barrier (BBB) in brainstem gliomas. DCE-MRM was used to evaluate BBB permeability in a mouse model of pHGG as a function of location (cortex vs. brainstem) and histone mutation (mutant H3.3K27M vs. wild-type H3.3). The pHGG model was generated by expressing PDGF-B, Cre, and mutant H3.3K27M or wild-type H3.3 in the cortex/brainstem of nestin tv-a: $p53^{fl/fl}$ mice at post-natal day 3. T2-weighted MRI was used to determine tumor location/extent followed by DCE-MRM for estimating the rate constant for tracer exchange across the barrier.

Stage 4: DCE-MRM as a measure of therapeutic response in a preclinical model of adenocarcinoma. Tumor neovasculature, often identified by leakiness, heterogeneous blood flow, and abnormal vessel diameter, is structurally and functionally different from healthy vessels. DCE-MRI has been widely used to study transfer kinetics between the intra- and the extra-vascular space, providing a set of in vivo biomarkers useful in diagnosis and assessment of response to therapy. The majority of studies measuring the effect of an anti-angiogenic agent have compared the mean value of these biomarkers on manually selected ROIs or over the entire tumor volume. These measurements include regions in the tumor where the interpretation of the kinetic parameters is unclear (such as in necrotic areas) or where the magnitude of response to therapy may be heterogeneous. We hypothesized that the incorporation of semi-quantitative kinetic parameters in the analysis of DCE-MRM data may provide a way for identifying tumor

subpopulations responding differently to therapy. Two cohorts of mice were imaged at five time points over the course of four weeks. The treatment/control group received bevacizumab/saline at a dose of 5 mg/kg or 5 ml/kg twice weekly; DCE-MRM experiments were performed weekly. At completion of study, mice were perfusion-fixed for histology (CD31 and HE staining). The time-to-peak (TTP) was calculated on smoothed signal intensity vs. time curves. The histogram of TTP was used to identify two (fast- and slow-enhancing) regions based on a threshold of TTP=1000 sec. The regions were correlated to permeability maps, CD31 and HE slides, and the effect of therapy was locally examined.

2. DCE MR Microscopy: Acquisition and Reconstruction

The implementation of the acquisition methodology needed for volumetric DCE-MRM requires a study of the sampling strategy, the reconstruction algorithm, and the trade-offs between the relevant imaging parameters.

2.1 k-Space sampling

The most naturally abundant NMR-active nucleus in a living organism is the hydrogen nucleus contained in the water molecule. In the presence of magnetic field gradients, the acquired MR signal is equal to the Fourier transform of the effective spin density of the object:

$$s(t) = \int M(x,y,z) e^{-2i\pi \vec{\boldsymbol{K}}\cdot\vec{\boldsymbol{r}}}\, d\vec{\boldsymbol{r}} \qquad \textbf{Eqn. 1}$$

where $\vec{\boldsymbol{K}} = (k_x, k_y, k_z)$, $\vec{\boldsymbol{r}} = (x,y,z)$, and M = effective spin density (a product of system gain, magnetization, and relaxation terms). A direct comparison of Eqn. 1 with the definition of the Fourier transform reveals that the MR signal is sampled at the locations defined by $\vec{\boldsymbol{K}}$:

$$k_i = \frac{\gamma}{2\pi}\int_0^t G_i(\tau)d\tau, \quad i = x,y,z \qquad \textbf{Eqn. 2}$$

where γ = gyromagnetic ratio (42.58 MHz/T for hydrogen nuclei) and G = magnitude of spatially variant magnetic field. For this reason, we say that in MR imaging we sample the k-space (of the effective spin density) of the object. The injection of a contrast agent

leads to a decrease in the T1-relaxation time in proportion to the absolute concentration of the tracer.

Magnetic field gradients determine the location at which the MR signal is measured; the gradient waveforms and their relative timing determine the trajectory traversed in k-space. One of the main advantages of MR imaging lies in the simplicity with which many different k-space trajectories (also known as sampling strategies or sampling patterns) may be generated. Figure 2 shows the Cartesian trajectory, one of the most widely used strategies in MR imaging due to its sampling efficiency and reduced sensitivity to main magnetic field inhomogeneity and gradient nonlinearity.

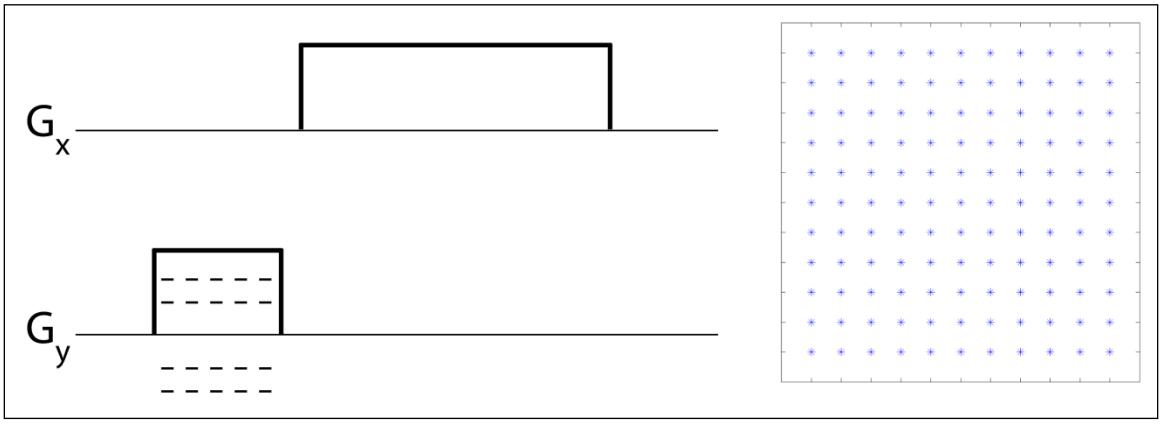

Figure 2: Cartesian k-space trajectory in 2-dimensions. The G_x and G_y gradient waveforms determine the rectilinear sample point locations.

Improvements in magnetic field uniformity and electronic components have allowed for the use of a large number of non-Cartesian sampling strategies each with their own advantages. Figure 3 shows the spiral trajectory, one of the early techniques

developed for fast MR imaging (Meyer, Hu et al. 1992). The need for advanced applications of MRI, such as imaging of different chemical species, or immunity to motion artifacts, led to the development of rosette (Noll 1997), PROPERELLER (Pipe 1999), circular (Zhou, Liang et al. 1998), and several other sampling methods.

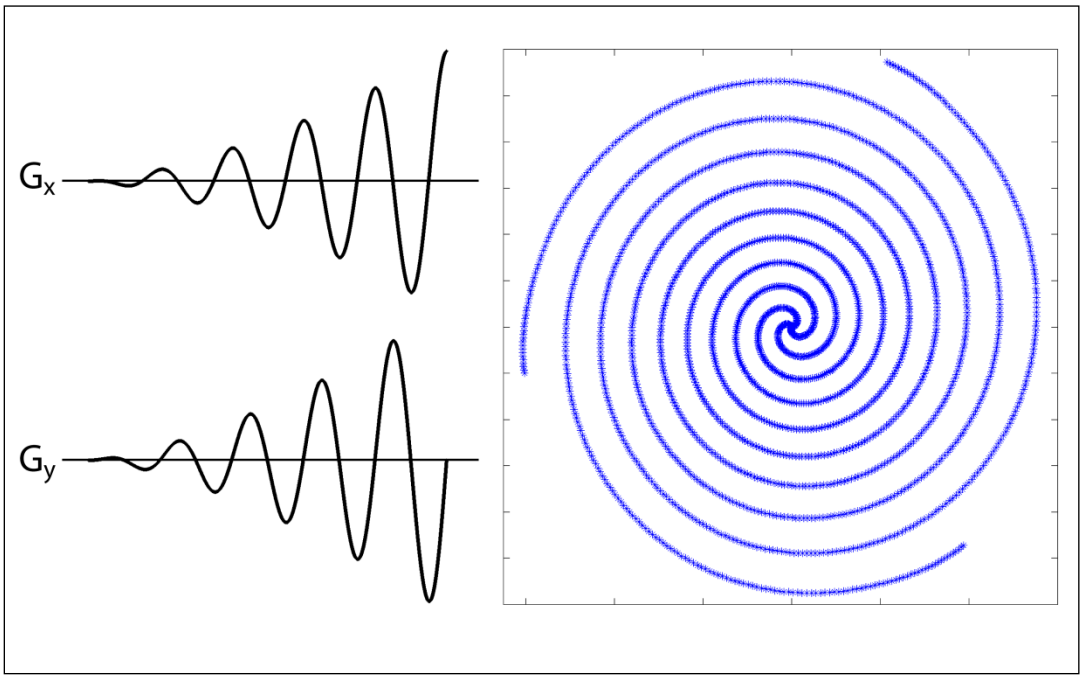

Figure 3: Spiral sampling function in 2-dimensions. This trajectory has higher data collection efficiency as compared to the Cartesian method.

2.1.1 Projection acquisition

Projection acquisition (projection/radial imaging) was the k-space trajctory used in the first publication demonstrating the ablity of the interation between a magnetized sample and applied magnetic fields to generate a tomographic image (Lauterbur 1973).

In radial imaging, the signal is acquired along spokes emanating or traversing the center of k-space as shown in Figure 4.

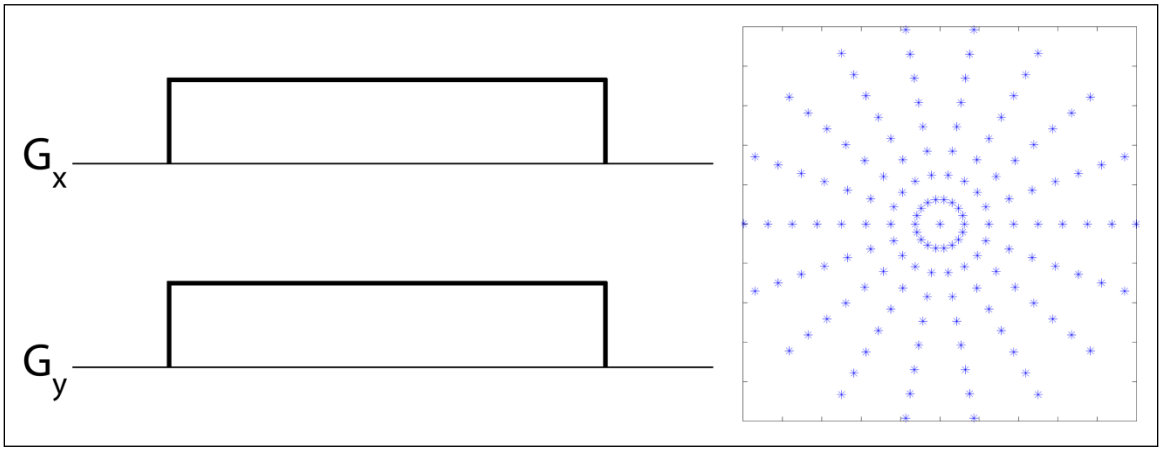

Figure 4: Projection imaging in 2-dimensions. The acquisition trajectory lies along spokes emanating from (or traversing) the center of k-space.

The main advantage of this technique, arising from the increased number of samples at the center of k-space where signal intensity is encoded, is its reduced sensitivity to motion and flow artifacts (Glover and Pauly 1992). With Cartesian sampling, periodic motion such as respiratory or cardiac motion, results in periodic intensity variations (ghosts); these artifacts appear throughout the field of view at a frequency dependent on the period of the motion and the time between the acquisition of two consequtive rectilinear lines. With radial imaging, motion artifacts appear as low intensity streaks close to the moving structure and increased intensity streaks at the perifery of the field of view. Figure 5 demonstrates these differences in a mouse abdominal scan. Motion reduction is of critical importance in diffusion-weighted imaging (Gmitro and

Alexander 1993), flow imaging (Nishimura, Jackson et al. 1991), and contrast-enhanced MRI.

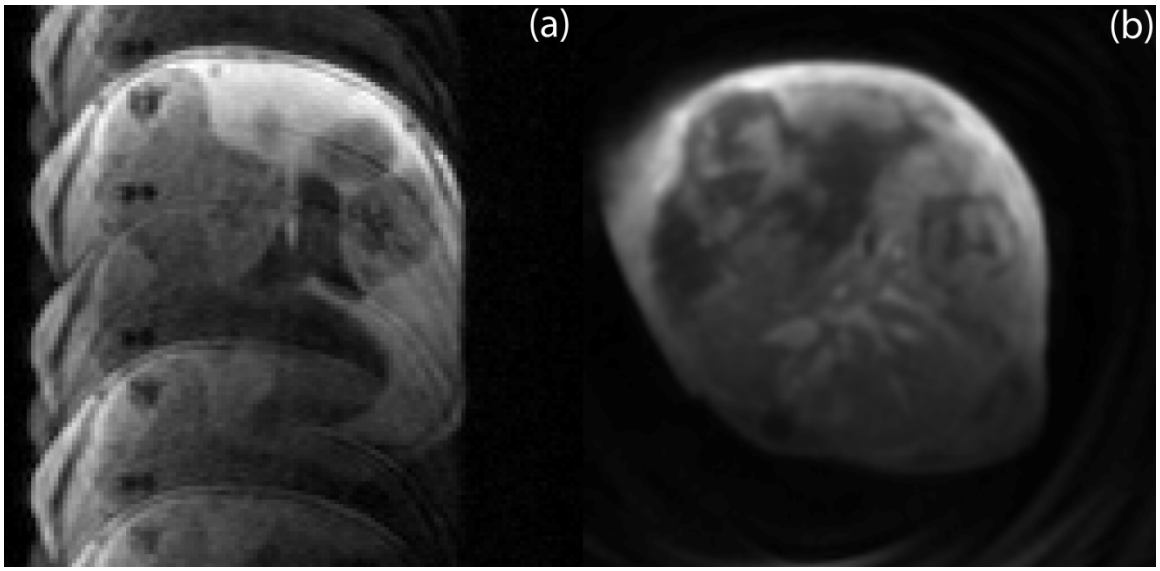

Figure 5: Comparison of motion artifact in mouse abdominal scan. (a) Reconstruction of GRE acquisition with Cartesian sampling. (b) Radial sampling of FID acquisition with similar imaging parameters. Motion causes ghosting in Cartesian sampling and blurring (notice edges) in radial sampling.

In 2D projection imaging, the number of spokes (views) needed to satisfy the Nyquist criterion at the periphery of k-space is given by Eqn. 3

$$N_{Nyquist} = \pi M \qquad \textbf{Eqn. 3}$$

where M = matrix size. In this case the views are acquired from the center of k-space to the periphery (as opposed to acquisitions from one end to another). This relationship can be derived by considering the distance between two points at the maximum k-space coordinate, which in turn is determined by the spatial resolution of the acquisition

(Bernstein, King et al. 2004). Nevertheless, the artifacts in images acquired with a smaller number of spokes consist of low intensity streaks at the periphery of the field of view (Scheffler and Hennig 1998). In two dimensions, the size of the artifact-free region at the center of the field of view depends on the total number of spokes as shown in Eqn. 4.

$$FOV_{eff} = FOV\left(\frac{2N_s}{\pi M}\right) \qquad \textbf{Eqn. 4}$$

where FOV_{eff} = artifact-free (effective) field of view, FOV = prescribed field of view, N_s = number of acquired spokes, M = matrix size. Undersamling artifacts in projection acquisition MRI are more tolerable than those in Cartesian imaging in which high intensity wraparound ghosts are overlayed on the field of view. Vastly undersampled radial imaging has found applications in contrast-enhanced MR angiography (Peters, Korosec et al. 2000), cardiac (Larson and Simonetti 2001), and interventional imaging (Peters, Lederman et al. 2003).

The main disadvantages of projection imaging are its increased scan time (when acquiring enough spokes to satisfy the Nyquist criterion at the periphery of k-space) and increased sensitivity to main magnetic field inhomogeneity and gradient nonlinearity. The latter of the two is of critical concern because, as discussed above, undersampling artifacts in radial imaging have minor effects on the final reconstruction. The analysis of the effect of field inhomogeneities and gradient nonlinearities on the point-spread function (PSF) of the radial sampling strategy has shown that the PSF is not only shifted

in location and reduced in amplitude, but it is also distorted (O'Donnell and Edelstein 1985). The location shift and amplitude decrease result in geometric distortion and SNR reduction respectively and can be easily restored for Cartesian sampling strategies, but not for radial MRI. The distortion in PSF leads to additional complex geometric distortions, blurring, and a decrease in spatial resolution. Figure 6 demonstrates these effects in a 3D radial acquisition of a 5 mM $CuSO_4$ phantom. Our studies have shown that the effect of gradient nonlinearities can be greatly reduced by measuring the k-space trajectory.

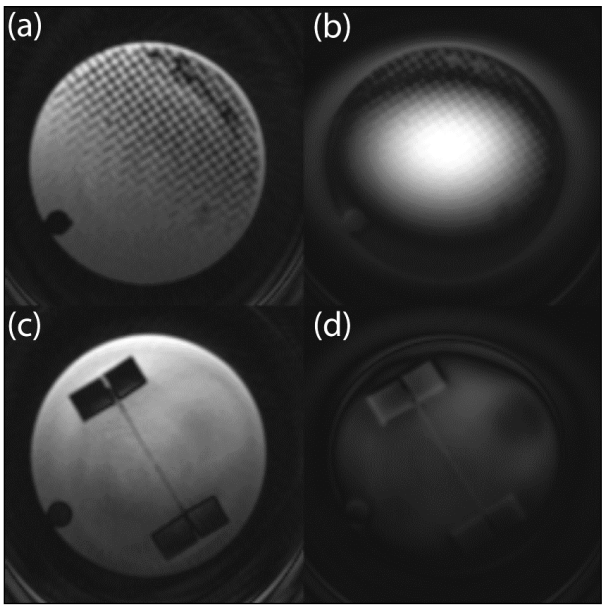

Figure 6: Comparison between images reconstructed with (a,c) measured and (b, d) assumed 3D radial trajectory. Panels (a) and (b) show complex geometric distortions and spatial resolution degradation. Panels (c) and (d) demonstrate the reduction in SNR.

2.2 Keyhole Imaging

Keyhole sampling, first introduced for Cartesian trajectories (Jones, Haraldseth et al. 1993; Van Vaals, Brummer et al. 1993), refers to a post-acquisition filtering technique in which the center of k-space is updated more frequently than the periphery with the purpose of increasing temporal resolution. This technique relies on the premise that image intensity is encoded at the center of k-space and high resolution features at the periphery. Figure 7 describes schematically the post-processing algorithm for rectilinear keyhole MRI. The main application for this method has been dynamic contrast-enhanced MRI, but interventional (Duerk, Lewin et al. 1996), cardiac (Suga, Matsuda et al. 1999) and fMRI (Xiong, Fox et al. 1999) imaging have also been explored.

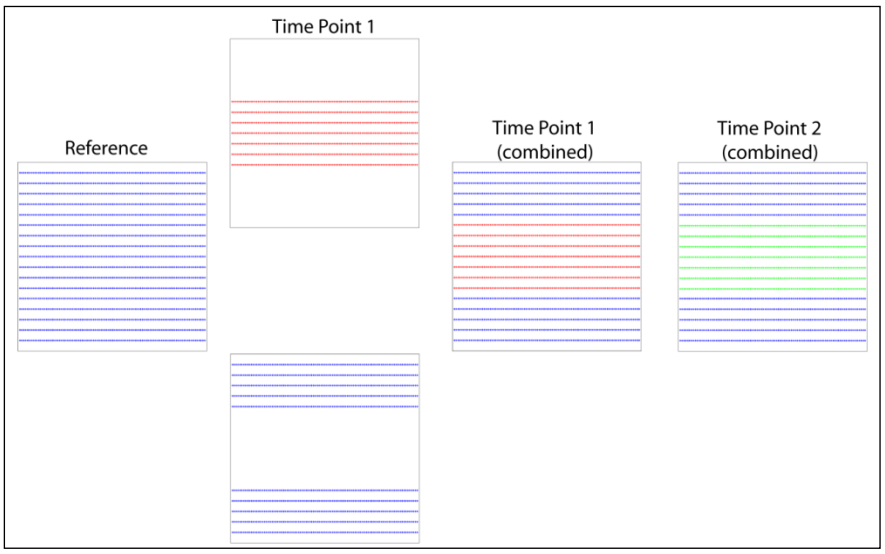

Figure 7: Cartesian keyhole imaging. Initially a reference image containing all the data in k-space is acquired. Subsequent time-points acquire a relatively small percentage of the lines at the center of k-space. The reconstruction of each time-point contains the periphery of k-space from the reference image and the center from the respective time-point.

The effects of 2D Cartesian keyhole imaging on spatial and temporal resolution have been studied by several groups (Hu 1994; Duerk, Lewin et al. 1996; Bishop, Santyr et al. 1997; Xiong, Fox et al. 1999). These studies have suggested that even though the Nyquist criterion is satisfied throughout k-space, keyhole MRI provides benefits in temporal resolution only for structures containing relatively low spatial frequencies. The temporal resolution for structures containing high spatial frequencies (for example, blood vessels) is not improved. Although reconstruction algorithms may improve the visual appearance of the images by reducing discontinuities between the reference and

low frequency acquisition (Zhi-Pei and Lauterbur 1994), the effect on quantitative MRI is not significant in high spatial frequency features (Bishop, Santyr et al. 1997).

Projection sampling lends itself naturally to keyhole MRI. The acquisition of radial trajectories leads to substantial oversampling at the center of k-space where pixel intensity is encoded. Figure 8 describes schematically the post-processing algorithm for radial keyhole imaging. The main advantage of this strategy, as compared to Cartesian keyhole, is that at every time point the periphery of k-space is also sampled. The views of the time point being reconstructed provide a temporally distinct measurement of some of the periphery of k-space enabling a constant update of the high frequency information. Radial keyhole imaging has been shown to provide increases in temporal resolution that allow for perfusion (Mistry, Pollaro et al. 2008) and dynamic contrast-enhanced MRI (Dougherty, Isaac et al. 2007).

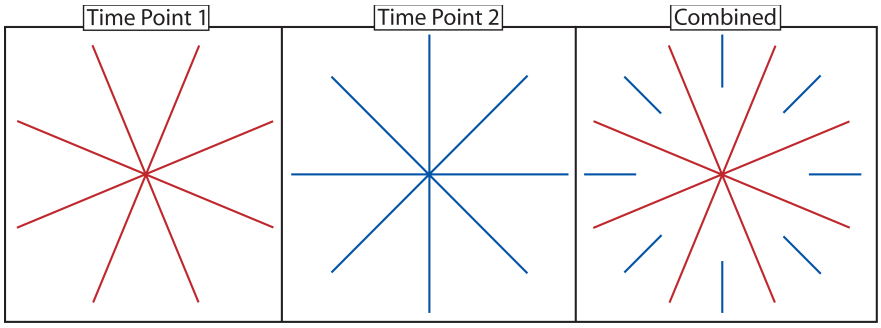

Figure 8: Radial keyhole imaging. A limited number of azimuthaly equidistant spokes is acquired at the first time point (TP1). The same number of spokes, rotated at an angle, is acquired at second time point (TP2). When reconstructing TP1, only the preiphery of the views from TP2 are added in k-space.

2.3 Reconstruction

Reconstruction is a mathematical operation by which the raw MR data acquired with a given pulse sequence and sampling method are transformed into the image of the object. Cartesian acquisitions measure the Fourier transform of the effective spin density in equidistant rectilinear points. The fast Fourier transform (FFT) (Cooley and Tukey 1965) is the optimal algorithm in this case. The FFT is undefined for applications where non-rectilinear sampling strategies are employed. The main reconstruction approach for non-Cartesian acquisitions has been to resample the data onto a rectilinear grid to enable the use of the FFT. Re-sampling can be implemented by interpolation or convolution. Convolution re-sampling is known as gridding (or re-gridding) and is the most widely adapted reconstruction technique for non-Cartesian MRI due to its simplicity and robustness (Jackson, Meyer et al. 1991). In the special case of projection imaging, which samples the Fourier transform of the object similarly to x-ray computed tomography, filtered back-projection may also be used. Recently, an algorithm for the calculation of the inverse Fourier transform directly from non-equidistant data points (Dutt and Rokhlin 1993) has been successfully applied to MRI (Jiayu, Yanhui et al. 2009).

The gridding operation is described by Eqn. 5:

$$m(\vec{r}) = \frac{IFFT\left(\left[\left(S(\vec{K}) * D(\vec{K}) * W(\vec{K})\right) \otimes C(\vec{K})\right] * \text{Ш}(\vec{K})\right)}{c(\vec{r})} \qquad \textbf{Eqn. 5}$$

where $\vec{\boldsymbol{K}} = (k_x, k_y, k_z)$, $\vec{\boldsymbol{r}} = (x, y, z)$, $m(\vec{\boldsymbol{r}})$ = reconstructed image, $S(\vec{\boldsymbol{K}})$ = sampling function, $D(\vec{\boldsymbol{K}})$ = MR data acquired at locations defined by $S(\vec{\boldsymbol{K}})$, $W(\vec{\boldsymbol{K}})$ = density compensation factors, $\otimes$ = convolution operator, $C(\vec{\boldsymbol{K}})$ = convolution function used for interpolation, $\text{Ш}(\vec{\boldsymbol{K}})$ = rect function, and $c(\vec{\boldsymbol{r}})$ = inverse Fourier transform of $C(\vec{\boldsymbol{K}})$. Jackson et al. have shown that the Kaiser-Bessel function is the optimal kernel $C(\vec{\boldsymbol{K}})$ for MR data reconstruction (Jackson, Meyer et al. 1991).

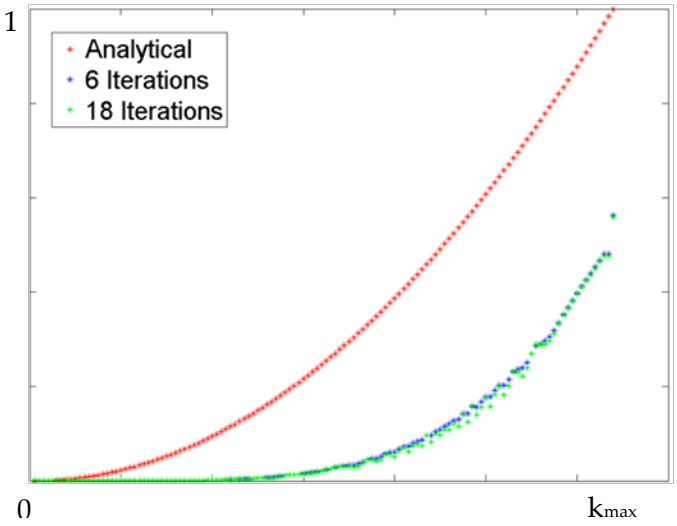

Figure 9: Comparison between analytic and iterative density compensation factors calculated with 6 and 18 iterations. The sampling function in this acquisition was a 3D radial keyhole trajectory. Analytic DCF over-emphasize the raw MR data at every location.

The calculation of the density compensation factors (DCF) in Eqn. 5 is trivial for sampling functions described by simple geometries, such as the radial or the spiral trajectories. It can be shown that the DCF for radial acquisitions is a factor arising from a change in coordinate systems. More generally, the determinant of the Jacobian of the

transformation matrix from an arbitrary coordinate system to a rectilinear one, can be used as the density compensation factor (Hoge, Kwan et al. 1997). In cases, when the transformation from the arbitrary coordinate system cannot be derived, such as in radial keyhole MRI, the calculation of DCF is nontrivial. Several methods have been described for this purpose (Pipe and Menon 1999; Rasche, Proksa et al. 1999; Mitsouras, Mulkern et al. 2007; Johnson and Pipe 2009). Rasche et al. proposed the use of the volume of the Voronoi cell around a given sampling point as the DCF for that point (Rasche, Proksa et al. 1999). Pipe et al. proposed an iterative technique which solves for density compensation factors that minimize the error from the gridding operations in k-space (Pipe and Menon 1999). Johnson et al. used Pipe's iterative algorithm with a novel gridding kernel and found that this method reconstructs images with the smallest root-mean-square error (Johnson and Pipe 2009). Johnson's method is easy to implement and does not make any assumptions about the k-space sampling strategy; the only inputs are the k-space coordinates at which the MR signal is acquired. Using this approach, analytic and iterative DCF are compared in Figure 9 and the effect on reconstruction is shown in Figure 10.

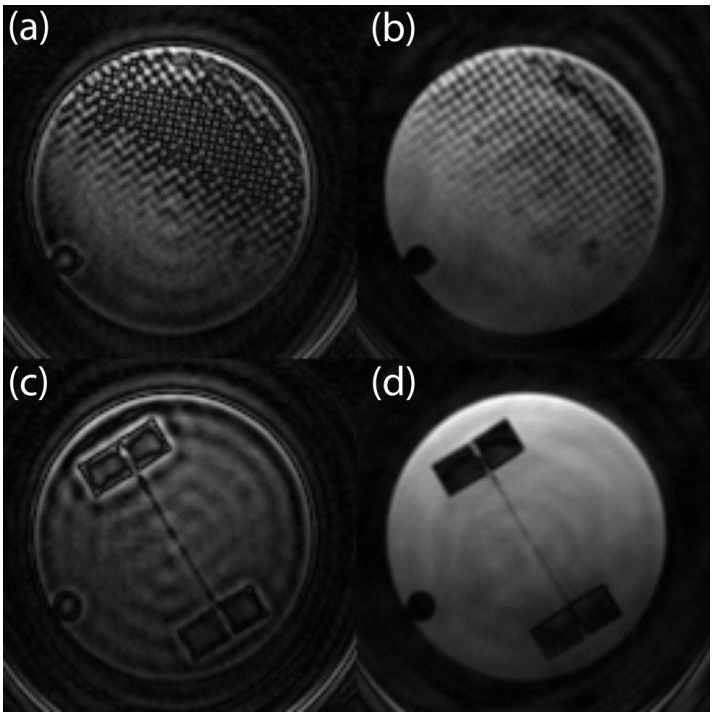

Figure 10: Comparison between reconstructions with analytic (a, c) and iterative (b, d) density compensation factors. The sampling function in this acquisition was a 3D radial keyhole trajectory.

3. DCE MR Microscopy: Pharmacokinetic Modeling

The analysis of the kinetic curves measured with DCE-MRI has traditionally been part of one of three frameworks: qualitative, semi-quantitative, and quantitative. These methods offer imaging biomarkers each with their advantages and disadvantages.

3.1 Qualitative biomarkers

Qualitative methods are based on the analysis of the shape of the signal intensity kinetic curve. In the absence of any pharmacokinetic modeling, several research groups have hypothesized that the temporal evolution of the signal intensity is indicative of underlying tumor viability (Buadu, Murakami et al. 1996). The descriptive parameters used for discriminating these different cases are summarized in Table 3 (Buadu, Murakami et al. 1996; Kuhl, Mielcareck et al. 1999; Chen, Shih et al. 2002). Representative curves from each category are shown in Figure 11. The main advantage of the qualitative analysis of DCE-MRI data is that it is simple: no curve-fitting or quantitative modeling is needed. Additionally, the acquisition of a pre-injection T1 map or the identification of an arterial input function is not required. The shape of the curve has been shown to correlate well with microvessel density measured in histology slides (Buadu, Murakami et al. 1996) and to discriminate between benign and malignant breast tumors (Kuhl, Mielcareck et al. 1999).

Table 3: Descriptive parameters used in the qualitative analysis of DCE-MRI signal intensity curves

Type 1 curve	Early enhancement, rapid washout
Type 2 curve	Early enhancement, plateau
Type 3 curve	Late enhancement, no washout
Type 4 curve	No (insignificant) enhancement

The main disadvantage of the qualitative analysis of DCE-MRI data is that it is based solely on signal intensity curves. Given that this signal is not linearly proportional to the concentration of the injected contrast agent, a comparison of types of curves from different scanners is virtually impossible. Pixel intensity is a quantity without physical units and its value may be strongly affected by the gain of the electronic components of the magnet and the image acquisition parameters.

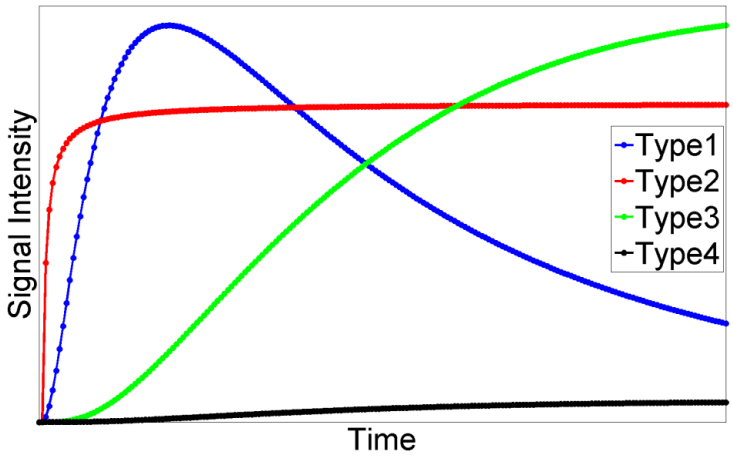

Figure 11: Representative kinetic curves from each descriptive category used in the qualitative analysis of DCE-MRI data.

3.2 Semi-quantitative biomarkers

Semi-quantitative methods are based on the mathematical analysis and the extraction of quantitative parameters from signal intensity curves. Figure 12 depicts the semi-quantitative biomarkers typically obtained during this analysis. The peak parameter (PEAK) is defined as the maximum value of the signal intensity curve; the time-to-peak (TTP) parameter is defined as the time it takes the signal intensity to reach the maximum value. The wash-in slope (WIS) is defined as the slope of the line from the signal intensity at the point of contrast agent injection to the peak enhancement; the wash-out slope (WOS) is defined as the slope of the line from peak enhancement to intensity value at end of scan. The area under the curve (AUC) is often encountered in semi-quantitative analyses, but should not be confused with the AUC from quantitative analyses. The former use the signal intensity curve; the latter use the curve of the contrast agent concentration. The biomarkers from the semi-quantitative analysis of DCE-MRI data have been applied in the clinical (Medved, Karczmar et al. 2004) and preclinical (Hillman, Singh-Gupta et al. 2009) domain for measuring tumor response to therapy. Because these methods base their analysis on signal intensity curves, they have the same advantages and disadvantages as qualitative methods.

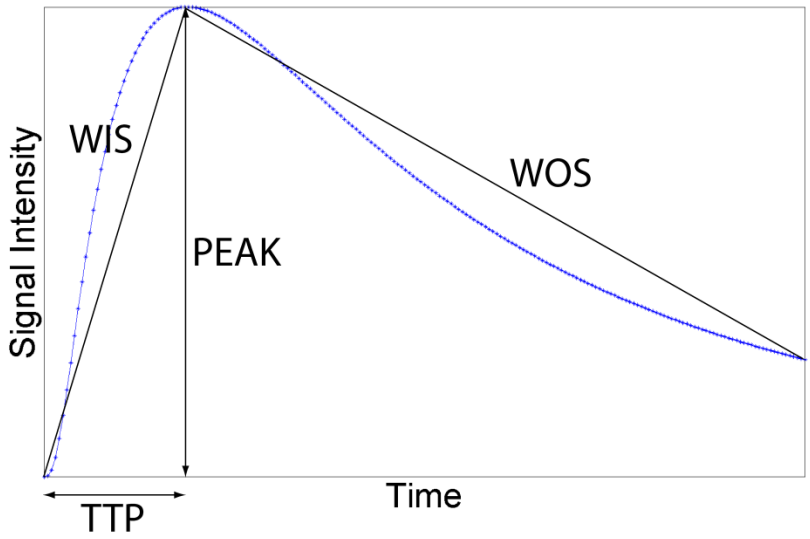

Figure 12: Semi-quantitative biomarkers. PEAK=peak enhancement, TTP=time to peak enhancement, WIS=wash-in slope, WOS=wash-out slope.

3.3 Quantitative biomarkers

Quantitative methods are based on the mathematical analysis and the extraction of kinetic parameters from the contrast agent concentration curve. The biomarkers calculated from fitting a pharmacokinetic model to the concentration curve are believed to be directly related to the underlying physiologic characteristics of the tissue being investigated (Barnes, Whisenant et al. 2012).

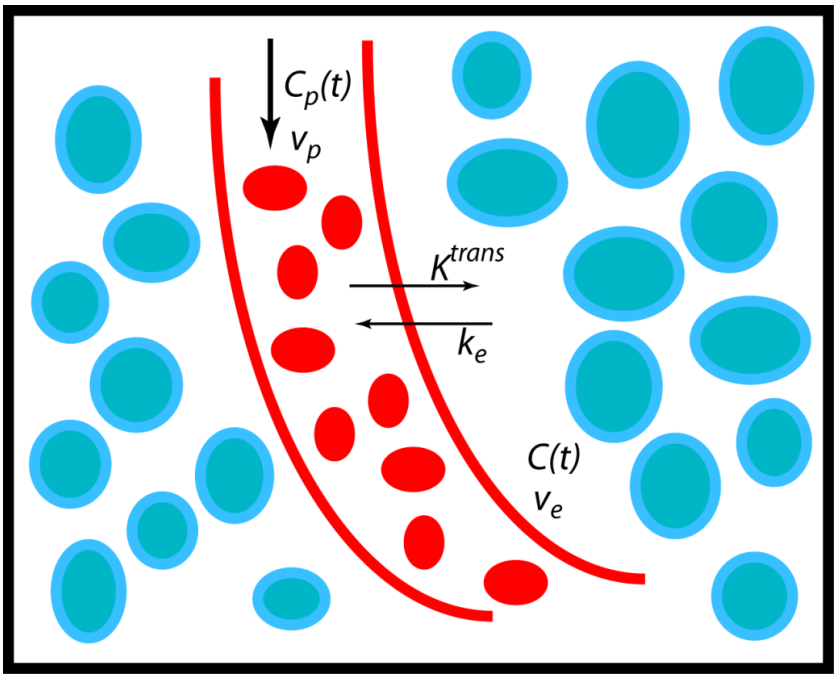

Figure 13: In the quantitative analysis of DCE-MRI data, the region of interest is described by a two-compartment model: the plasma space (*p*) with volume v_p and the extravascular-extracellular space (*EES*, or *e*) with volume v_e. The transfer constants, K^{trans} and k_e, are related to the rate of transport of the contrast agent across the endothelium barrier.

Assume the tissue of interest is composed of two compartments separated by a permeable membrane: the plasma space (*p*) with volume v_p and the extravascular-extracellular space (*EES* or *e*) with volume v_e, as shown in Figure 13. If the time-dependent concentration of the contrast agent in the plasma and extravascular-extracellular space is measured to be $C_p(t)$ and $C(t)$ respectively, then one of the most widely used kinetic models describing the exchange rates between these two compartments is given by (Tofts 1997):

$$C(t) = v_p \cdot C_p(t) + K^{trans} \int_0^t C_p(u) \cdot e^{-(k_e)\cdot(t-u)} du \qquad \textbf{Eqn. 6}$$

where K^{trans} is defined as the rate constant for the transfer of the agent from plasma to EES and is measured in ml/s of contrast agent per ml of tissue; k_e is the rate constant for the transfer of the agent in the inverse direction measured in same units as K^{trans}; v_e and v_p are also normalized with respect to the volume of the tissue of interest and as such do not have physical units. Eqn. 6 is referred to as the extended Tofts model (ETM); the standard Tofts model assumes $v_p = 0$. The area under the contrast agent concentration curve (AUC) is another parameter of interest in the quantitative analysis of DCE-MRI data. Typically, the concentration curve is integrated only for the first 1-5 minutes post-injection.

The biomarkers from quantitative DCE-MRI have been applied extensively in monitoring therapeutic response in solid tumors in the preclinical (Barnes, Whisenant et al. 2012) and clinical domain (O'Connor, Jackson et al. 2012). This technique allows for meaningful statistical comparisons across measurements from groups using different scanners and imaging protocols because it is based on the absolute concentration of the contrast agent.

3.3.1 Challenges in quantitative DCE-MRI

The challenges in quantitative DCE-MRI may be divided in two main categories: acquisition-related and analysis-related. The former are mainly associated with the

acquisition of the native *T1* map, the concentration of the tracer in the plasma space $C_p(t)$, spatiotemporal resolution, and coverage. The analysis-related challenges arise mainly during the calculation and the interpretation of the kinetic parameters in Eqn. 6.

3.3.1.1 Acquisition-related challenges

The standard method for an accurate estimation of *T1* over a region of interest is the inversion-recovery spin-echo technique (Bernstein, King et al. 2004). For volumetric sampling, the acquisition time with this approach is prohibitively long. Deoni et al. compared several fast *T1*-maping methods and suggested that the acquisition with a variable flip angle (VFA), spoiled, gradient recalled (SPGR), pulse sequence is the most effective and leads to an error of approximately 7% over a range of *T1* between 300 and 2000 ms (Deoni, Rutt et al. 2003). Schabel et al. analyzed the uncertainty in *T1* arising from limited SNR and field uniformity and suggested an optimal range of flip angles for the SPGR technique (Schabel and Parker 2008).

The measurement of the concentration of the tracer in the plasma space $C_p(t)$, also referred to as the arterial input function (AIF), is particularly challenging in small animals. A vessel feeding the tissue of interest is usually difficult to indentify. When present in the field of view, these vessels are so small that partial volume effects inevitably bias the detected signal intensity. Furthermore, the temporal resolution for sufficient sampling of the AIF needs to be <2 seconds, limiting the spatial resolution and

the coverage of the acquisition. Several investigators, in the preclinical and clinical domain, have suggested the use of a population averaged AIF and have examined the effect on the calculation of the kinetic parameters (Parker, Roberts et al. 2006; Loveless, Halliday et al. 2012). Loveless et al. found that in mice the quantitative parameters estimated using a population derived arterial input function were highly correlated to those calculated from an individual AIF (Loveless, Halliday et al. 2012).

The issue of temporal length (total acquisition time) of a DCE-MRI study is more complicated. Simulation studies have shown that the precision of the quantitative parameters decreases with total acquisition time (Larsson, Kleppestø et al. 2012). Figure 14 shows the effect of decreasing the temporal length of the acquisition on K^{trans} calculation. The simulation was done by using the first 50% or 75% of the data from a study of a colorectal tumor implanted in the mammary fat pad of a mouse. The decision for total acquisition time would have to strike the balance between number of experiments/day and tolerated precision, keeping in mind that the shorter the scan the less precise the estimation of the quantitative parameters.

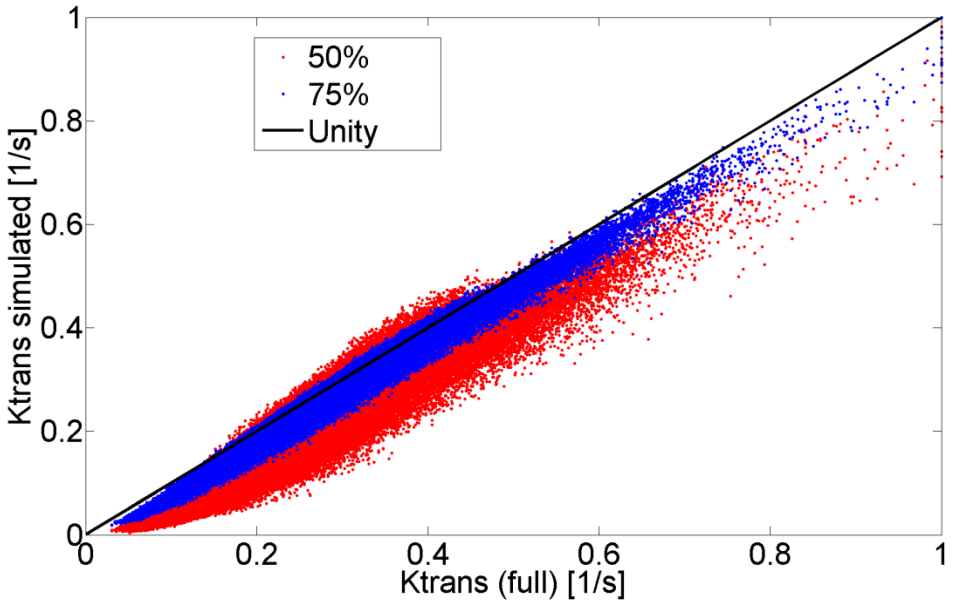

Figure 14: Effect of total acquisition time on precision of K^{trans}. The red data were calculated by cropping the total acqusition time by 50%. The calculation of the blue data was done using 75% of the length of the acquisition. Total acquisition time was ~ 40 mins.

3.3.1.2 Analysis-related challenges

The extended Tofts model provides an estimation of three unique kinetic parameters (K^{trans}, v_e, v_p) and one derived parameter ($k_e=K^{trans}/v_e$). The interpretation of the volumes (v_e, v_p) of the two compartments is unambiguous; the interpretation of the rate constant K^{trans} is not trivial. Three distinctions are made with respect to the physiologic parameters of the tissue under study: flow-limited case, permeability-limited case, and mixed case. In the flow-limited case, the assumption is that the permeability of the endothelial barrier is much higher than the flow rate (perfusion) to the region of interest. Under these conditions K^{trans} is directly proportional to flow rate (perfusion). In the

permeability-limited case, the flow is considered to be so high that it is not altered by the exchange between the two compartments. In this case, K^{trans} measures the product of the permeability and the surface area of the endothelium. As expected, in the mixed case K^{trans} is an intermediate measure of the above two quantities. These definitions are summarized in Table 4. Sourbron and Buckley recently published a rigorous study on the interpretation of the kinetic parameters derived from the Tofts models (Sourbron and Buckley 2011). They determined that the extended Tofts model accurately fits the DCE-MRI data only in weakly vascularized ($v_p \approx 0$) and/or high perfused (high flow) regions. In all other cases, the fit to the dynamic data is not accurate or the interpretation of K^{trans} is unclear.

Table 4: Interpretation of K^{trans}. Under the flow-limited model, K^{trans} is equal to the product of flow F [ml/g/min], density of tissue ϱ [g/ml], and (1-Hct) where Hct=hematocrit. Under the permability-limited model, K^{trans} is equal to the product of density, permeability of capilary wall P [cm/min], and surface are of capilary wall per unit mass of tissue S [cm²/g]. In the mixed case, K^{trans} falls between the two quantities defined for the above two models (E=initial extraction ratio).

Flow-limited	$K^{trans} = \rho F(1 - Hct)$
Permeability-limited	$K^{trans} = \rho PS$
Mixed	$K^{trans} = \rho EF(1 - Hct)$

The extended Tofts model (Eqn. 6) is an integral equation that does not have an analytic solution. The solution can be found using any of the fitting techniques from

numerical analysis (usually the Levenberg-Marquardt algorithm) (Ahearn, Staff et al. 2005) or a matrix inversion method (Murase 2004). Because the Levenberg-Marquardt fitting routine requires an initial guess, the solution to Eqn. 6 may be different based on different initial conditions. To avoid estimation errors, the consensus is that the analysis of DCE-MRI data should always be performed with the same numerical method and initial conditions (Barnes, Whisenant et al. 2012).

4. A Comparison of Keyhole Strategies for DCE-MRM

4.1 Outline

Dynamic contrast-enhanced (DCE) MRI has been widely used as a quantitative imaging method for monitoring tumor response to therapy. The simultaneous challenges of increasing temporal and spatial resolution, in a setting where the signal from the much smaller voxel is weaker, have made this MR technique difficult to implement in small-animal imaging. Existing protocols employed in preclinical DCE-MRI acquire a limited number of slices resulting in potentially lost information in the third dimension. This study describes and compares a family of four-dimensional (3D spatial + time), projection acquisition, keyhole-sampling strategies that support high spatial and temporal resolution.

The 4D method is based on an RF-spoiled, steady-state, gradient-recalled sequence with minimal echo time. An interleaved 3D radial trajectory with a quasi-uniform distribution of points in k-space was used for sampling temporally resolved datasets. These volumes were reconstructed with three different k-space filters encompassing a range of possible keyhole strategies. The effect of k-space filtering on spatial and temporal resolution was studied in a 5 mM $CuSO_4$ phantom consisting of a meshgrid with 350-μm spacing and in 12 tumor cell lines (HT-29, LoVo, MX-1, sarcoma, three tumors/group). The time-to-peak signal intensity was used to assess the effect of

the reconstruction filters on temporal resolution. As a measure of heterogeneity in the third dimension, we analyzed the spatial distribution of the rate of transport (K^{trans}) of the contrast agent across the endothelium barrier for several different types of tumors.

4D radial keyhole imaging does not degrade the system spatial resolution. Phantom studies indicate there is a maximum 40% decrease in SNR as compared to a fully sampled dataset. T1 measurements obtained with the interleaved radial technique do not differ significantly from those made with a conventional Cartesian spin-echo sequence. A bin-by-bin comparison of the distribution of the time-to-peak parameter shows that 4D keyhole reconstruction does not cause significant temporal blurring when a temporal resolution of 9.9 seconds is used for the subsamples of the keyhole data. In-vivo studies reveal substantial tumor heterogeneity in the third spatial dimension that may be missed with lower resolution imaging protocols.

Volumetric keyhole imaging with projection acquisition provides a means to increase spatial and temporal resolution and coverage over that provided by existing 2D Cartesian protocols. Furthermore, there is no difference in temporal resolution between the higher spatial resolution keyhole reconstruction and the undersampled projection data. The technique allows one to measure complex heterogeneity of kinetic parameters with isotropic, microscopic spatial resolution.

4.2 Introduction

Dynamic contrast-enhanced (DCE) MRI has become an important imaging tool in the study of several diseases. This technique has been particularly useful in oncology for monitoring therapeutic response in solid tumors (Padhani and Miles 2010; O'Connor, Jackson et al. 2012). A typical DCE-MRI protocol consists of the following steps: 1) acquisition of pre-injection images for calculating the native *T1* and the equilibrium longitudinal magnetization (M_0) maps; 2) acquisition of post-injection images for determining the time-dependent tracer concentration; and 3) analysis of tracer dynamics to extract physiological characteristics of the tumor under study. Numerous methods exist for the implementation of each of the above steps: *T1* and M_0 maps can be acquired with several techniques (Li, Zhu et al. 2000; Deoni, Rutt et al. 2003; Cheng 2007; Treier, Steingoetter et al. 2007); different mathematical models can be used to analyze the dynamic data (Johnson and Wilson 1966; Patlak, Blasberg et al. 1983; Tofts and Kermode 1991; Østergaard, Weisskoff et al. 1996; St. Lawrence and Lee 1998; Tofts, Brix et al. 1999; Brix, Kiessling et al. 2004; Yankeelov, Luci et al. 2005); and finally, various pulse sequences differing in sampling strategies and acquisition parameters have been developed to sample the signal in k-space (Daniel, Yen et al. 1998; Yen, Han et al. 2000; Dougherty, Isaac et al. 2007; Han, Daniel et al. 2008).

The vast majority of preclinical sampling strategies used for DCE-MRI acquire a limited number of relatively thick slices. Volume averaging and limited coverage make it difficult to characterize the heterogeneity in the tumor microenvironment. The limitations are: 1) the location of the imaging slice is arbitrary (*which slice should be imaged?*); 2) longitudinal imaging is unreliable due to irreproducible slice selection (*how do we pinpoint the location of the same slice in the tumor after a few weeks?*); and 3) even if the first two limitations are avoided, there is no guarantee that the functional parameters measured in a few slices are representative of the entire tumor (*what is the variation in the third spatial dimension?*)

The goal of this work is to develop a 4D imaging method for preclinical studies in which temporal and spatial resolution are increased to allow measures of tumor heterogeneity. The work is an extension of previous (clinical) efforts employing projection imaging with keyhole sampling (Song and Dougherty 2000; Song and Dougherty 2004; Dougherty, Isaac et al. 2007). Projection imaging, when implemented as a 3D sequence, provides inherently volumetric measurements, has reduced sensitivity to motion and flow artifacts, and allows for shorter echo times as compared to traditional Cartesian methods (Glover and Pauly 1992). The acquisition of radial trajectories leads to substantial oversampling at the center of k-space where most of the information related to pixel intensity is encoded. Hence, radial sampling lends itself naturally to

keyhole imaging as shown by others for 2D sequences (Song and Dougherty 2004; Mistry, Pollaro et al. 2008). Based on these advantages, several post-acquisition methods can be developed to further improve temporal resolution, while minimizing sampling artifacts.

4.3 Materials and Methods

4.3.1 Radial keyhole acquisition

The radial acquisition sequence was implemented on the ParaVision 5.1 software platform (Bruker BioSpin MRI GmbH). The pulse sequence consists of an excitation hard pulse followed with the encoding gradients in three directions as shown in Figure 15. The sampling trajectory was adapted from Wong et al. (Wong and Roos 1994). This technique defines the location of the endpoints of the individual radial spokes (views) using a continuous spiral path on the surface of the unit sphere, resulting in a nearly uniform distribution of samples in k-space.

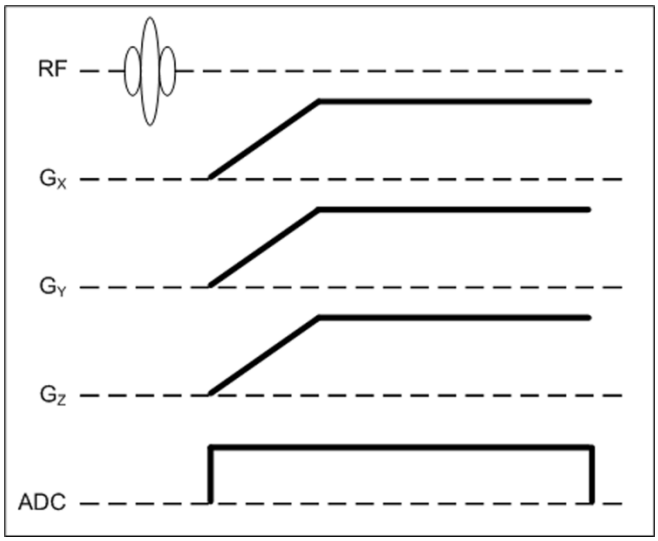

Figure 15: Pulse sequence diagram for 3D radial encoding. During the ramp portion of the gradients, the sampling distance in the radial direction is not uniform. Typically, 1/3 of the ADC time is spent on the ramp portion. Ideally, the k-space locations can be calculated from the area under the gradient curves. However, in the presence of system nonlinearities (gradient amplifiers, eddy currents) coordinates in k-space may deviate significantly from the theoretical projections. Therefore, the trajectory was measured at the beginning of each study.

The fully-sampled k-space volume was divided into V_t interleaved acquisitions, where V_{t-1} is the rotated version of V_t as illustrated in Figure 16. If N is the total number of acquired spokes, then the k_x,k_y,k_z-coordinates of the endpoints of each spoke in our interleaved trajectory are given by:

$$\alpha(i,j) = \frac{c\pi}{2}[j + (i-1)V_t]$$

$$k_z(i,j) = 1 - \frac{2[j + (i-1)V_t]}{N} \qquad \textbf{Eqn. 7}$$

$$k_x(i,j) = \cos(\alpha)\sqrt{1 - k_z^2(i,j)}$$

$$k_y(i,j) = \sin(\alpha)\sqrt{1 - k_z^2(i,j)}$$

where the index $j=1,2,\ldots,V_t$ references interleaves and $i=1,2,\ldots,N/V_t$ references the spokes of a specific interleaf. Hence $k_z(i,j)$ is to be interpreted as the k_z-coordinate of the endpoint of the i-th view in the j-th interleaf and similarly for $k_x(i,j)$ and $k_y(i,j)$. The constant c in the expression for the angle α effectively randomizes the order in which views are acquired in the k_x-k_y direction, thus minimizing artifacts arising from incoherent signal build-up. In our sequence we used $c=203$. Fast imaging sequences impose high demands on the scanner hardware leading to k-space trajectories that may deviate significantly from the theoretical projections. The effect on image quality is shown in Figure 6. Therefore, the k-space trajectory was measured at the beginning of each scan with the method described by Zhang et al. (Zhang, Hetherington et al. 1998).

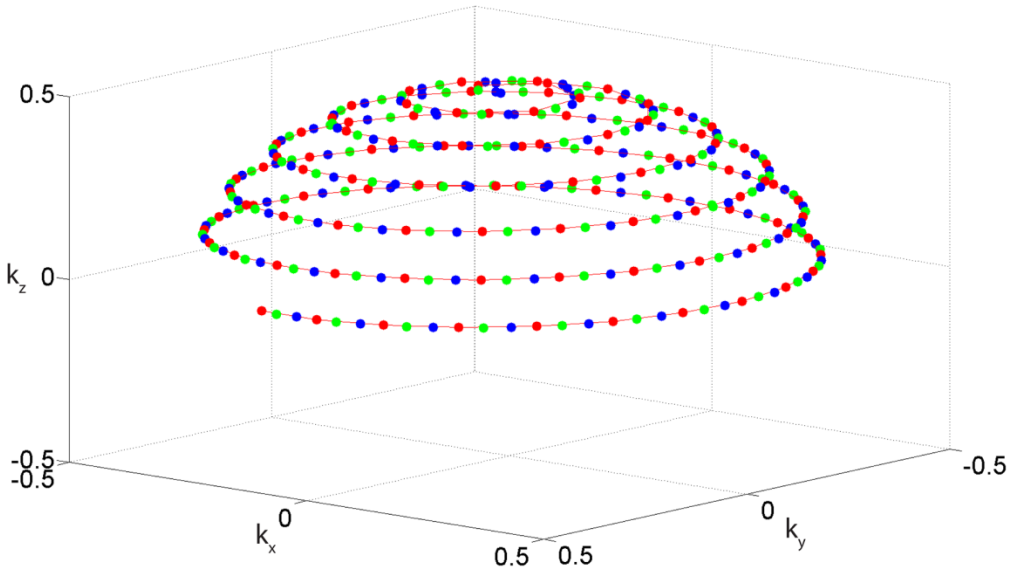

Figure 16: k-Space sampling strategy demonstrating the interleaved radial acquisition. Only the endpoint of each view (spoke) is shown here. Undersampling is implemented by dividing the fully sampled k-space volume into V_t interleaved acquisitions, where V_{t-2} (blue) is the rotated version of V_{t-1} (green), which in turn is the rotated version of V_t (red). Each interleave provides a quasi-uniform sampling of the surface of the sphere.

Typical acquisition parameters are as follows: FOV = 20 mm^3, reconstruction matrix size = 128^3, TR/TE = 5/0.02 ms, NEX = 1, flip angle = 10°, digitizer bandwidth = 100 kHz, 1024 dummy views, 1980 views per interleaf, total number of interleaves = 13, and 64 readout points along each projection. In this case, the total acquisition time per interleaf is 9.9 seconds.

4.3.2 Radial keyhole reconstruction

Projection acquisition lends itself naturally to keyhole imaging because of the high oversampling rate at the center of k-space. Assume four interleaves were acquired

in the order *A, B, C, D*. To assess the effect of radial keyhole reconstruction on effective temporal resolution, the following filtering methods were tested on the same raw datasets:

1. Uniform frequency-cutoff (UFC): To reconstruct a given time point of the DCE study, e.g. time-point 1 (interleaf A), the views from the remaining time-points (interleaves B, C, and D) were filtered such that only the data in the outer shell of inner radius f_N were used. The views from interleaf A were left intact. The sampling function for this case is shown schematically in Figure 17(a).
2. Variable frequency-cutoff (VFC): In this case, to reconstruct the first time point, the views from interleaf *B* were filtered such that only the data in the outer shell of inner radius f_N were used, the views from interleaf *C* were filtered such that only the data in the outer shell of inner radius f_1 were used, and similarly for the following interleaves. Again, as shown in Figure 17(b), the views from interleaf A were not filtered.
3. Undersampled (UND): The data from a single interleaf (e.g. A) were used to reconstruct the respective time point (e.g. time point 1) without the addition of data from the remaining interleaves B, C, or D. The sampling function for this method is shown in Figure 17(c).

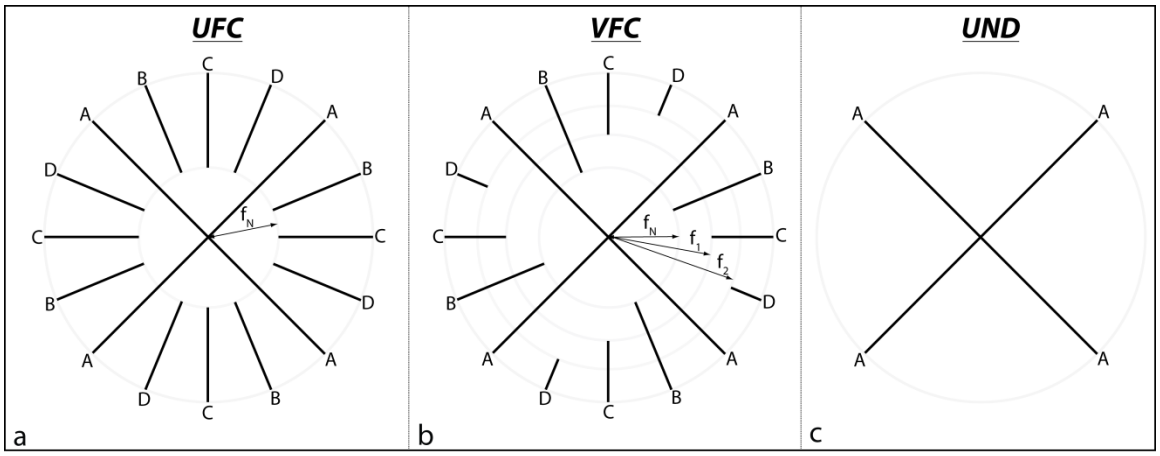

Figure 17: Radial keyhole reconstruction strategies (2D shown for clarity). In this example, interleaves are acquired in the order A, B, C, D and amount to time points 1, 2, 3, 4 in the DCE study. (a) Uniform frequency cutoff (UFC) filtering, (b) Variable frequency cutoff (VFC) filtering, and (c) Undersampled (UND) filtering. In UFC filtering, all interleaves contribute equally to the reconstruction of the high spatial-frequency features in image space; VFC filtering is an intermediate strategy in which the contribution to high spatial-frequencies from consecutive time points is slowly, in this case linearly, reduced; in UND filtering the absence of keyhole combination does not cause temporal blurring.

The cutoff frequency can be described by:

$$f_i = f_N + i\delta_i f_N \qquad \textbf{Eqn. 8}$$

where $i=1,2,\ldots,V_t$ and the parameter δ_i is:

$$\begin{aligned} UFC: &\quad \delta_i = 0, \forall i \\ VFC: &\quad \delta_i = \frac{k_{max} - f_N}{V_t f_N}, \forall i \\ UND: &\quad f_N = k_{max} \end{aligned} \qquad \textbf{Eqn. 9}$$

with k_{max} representing the maximum k-space coordinate that defines the particular spatial resolution being reconstructed and f_N defining the region of a single interleaf beyond which the Nyquist criterion is not satisfied. Eqn. 8 can be used to generate a family of filters by defining different parameters δ_i which may depend on the variable i.

To calculate the cutoff frequency f_N, we start by looking at the number of views for full sampling with the 3D radial trajectory (Bernstein, King et al. 2004):

$$N = \pi N_p^2 \qquad \textbf{Eqn. 10}$$

where N = total number of spokes (acquired from the center to the periphery of k-space) and N_p = the number of samples in the radial direction. For a total of V_t interleaves, the solid angle associated with each view in a single interleaved acquisition increases by a factor of V_t. Therefore, the Nyquist criterion is satisfied only in an inner sphere of radius:

$$f_N = \frac{k_{max}}{\sqrt{V_t}} \qquad \textbf{Eqn. 11}$$

where f_N is the k-space cutoff frequency shown in Figure 17. Since in the proposed sequence spatial encoding happens also during the ramp portion of the gradients, the number of samples in the radial direction that determines f_N is not found by $N_p/\sqrt{V_t}$ but by looking at the k-space radial sampling rate, Δk_r. Ideally, when using rectangular gradients, Δk_r is constant, but with trapezoidal gradients Δk_r will increase linearly in the ramp portion.

The standard re-gridding algorithm was used in the reconstruction of our radial keyhole data. A modified Kaiser-Bessel kernel (Beatty, Nishimura et al. 2005) allowing for a faster reconstruction, was employed in the gridding step. The kernel parameters were: window size = 3 pixels, oversampling ratio = 3. Analytical density compensation factors for the k-space sampling functions used in this work cannot be found in the published literature. We calculated these factors using the iterative algorithm described by Zwart (Zwart, Johnson et al. 2011) and the gridding kernel from Johnson (Johnson and Pipe 2009). Prior to gridding, the projections from different interleaves were selected using the sliding window method (Riederer, Tasciyan et al. 1988) providing a continuously updated outer shell in k-space. The raw data from each channel in the four-element array coil were reconstructed separately and combined with the Sum-of-Squares technique (Roemer, Edelstein et al. 1990). Finally, the reconstructed images were filtered with a 3D Hamming (Lowe and Sorenson 1997) window to reduce spatial domain ringing arising by the finite extent of the acquired MR data.

4.3.3 Calculation of fractional volume and permeability parameters

The signal value for our pulse sequence at steady state is given by (Callaghan 1991):

$$S(\alpha, TR, TE) = S_0 \frac{\sin(\alpha)\left(1 - e^{-TR/T1}\right)}{1 - cos(\alpha)e^{-TR/T1}} e^{-TE/T2^*} \qquad \textbf{Eqn. 12}$$

where S_0 is a constant proportional to the equilibrium longitudinal magnetization and to the spatially dependent system gain function. The $T2^*$ term can be reduced to unity since TE=0.02 ms≈0 ms. Eqn. 12 can then be linearized as:

$$\frac{S(\alpha, TR)}{\sin(\alpha)} = E1\frac{S(\alpha, TR)}{\tan(\alpha)} + S_0(1 - E1) \qquad \textbf{Eqn. 13}$$

where $E1=exp(-TR/T1)$. A varying flip-angle acquisition (Li, Zhu et al. 2000; Deoni, Rutt et al. 2003) with α=2°, 4°, 6°, 8°, 10°, 12°, 14°, 16° and TR=5 ms was used to measure $S(\alpha)$. The $T1$, and S_0 maps were obtained (by linear regression) from the slope and interception of Eqn. 13. To minimize sampling artifacts, keyhole filtering was not applied to the radial sequence during the varying flip-angle acquisition.

In the fast exchange limit the relaxation rate, $R1=1/T1$, is given by (Landis, Li et al. 2000):

$$R1(t) = R1_0 + r_1 C(t) \qquad \textbf{Eqn. 14}$$

where $R1_0$ is the native relaxation rate, $C(t)$ is the time dependent contrast concentration, and r_1 is the longitudinal relaxivity of Gd-DTPA (Magnevist, Schering AG, Berlin, Germany) which at 7 T was found to be r_1=3.275 $mM^{-1}s^{-1}$ (Noebauer-Huhmann, Szomolanyi et al. 2010). It has been shown (Heilmann, Kiessling et al. 2006; Schabel and Parker 2008) that for high accuracy, a non-linear relation between signal intensity and concentration needs to be assumed. The non-linear time dependent relaxation rate (Li, Zhu et al. 2000; Heilmann, Kiessling et al. 2006) is given by:

$$R1(t) = -\frac{1}{TR}\ln\left(\frac{1-(A+B)}{1-\cos(\alpha)\,(A+B)}\right)$$

Eqn. 15

$$A = \frac{S(t)-S(0)}{S_0 \sin(\alpha)}, \qquad B = \frac{1-E1_0}{1-\cos(\alpha)E1_0}$$

where $E1_0 = exp(-TR*R1_0)$, $S(0)$=signal intensity before contrast injection, and $S(t)$=time-dependent signal intensity. The concentration of the contrast agent is then calculated by rearranging Eqn. 14.

The rate constant K^{trans} was calculated as described in chapter 3.

4.4 Sequence validation

The effect of k-space filtering on spatial and temporal resolution was studied in a 5 mM $CuSO_4$ phantom consisting of a meshgrid with 350-μm spacing and in 12 tumors from three cell lines (HT-29, LoVo, MX-1) and a primary mouse sarcoma model (three tumors/group). The time-to-peak signal intensity was used to assess the effect of the reconstruction filters on temporal resolution. As a measure of heterogeneity in the third dimension, we analyzed the spatial distribution of the rate of transport (K^{trans}) of the contrast agent across the endothelium barrier.

4.4.1 Animal and phantom experiments

Female *nu/nu* mice with the following tumor cell lines, implanted in the mammary fat pad, were imaged: HT-29, LoVo, and MX-1 (three tumors/group, Charles

River Laboratories Wilmington, MA). A genetically engineered mouse model of soft tissue sarcoma (Kirsch, Dinulescu et al. 2007) induced in the right hind leg was also imaged (three tumors) with the same protocol. Tumors ranged in volume from 118 mm^3 to 1318 mm^3. During the MR experiment, a custom-made animal positioning system was used to maintain the mouse under anesthesia by isoflurane delivery via a nose cone. Body temperature was controlled between 36 °C and 37 °C by circulating warm water in the animal cradle. The animals were free-breathing and no respiratory gating was employed. The contrast agent was injected after the acquisition of 15 interleaves (i.e. time points) and dynamic imaging lasted for approximately 40 min (245 time points) post-injection. An automatic syringe pump (KD Scientific Inc., Holliston, MA) provided a consistent contrast injection. Gd-DTPA was administered as a bolus via a 27-gauge tail vein catheter at a dose of 0.5 mmol/kg and flow rate of 2.4 mL/min as described by Loveless et al (Loveless, Halliday et al. 2012).

The effect of the 4D-keyhole sampling technique on spatial resolution and artifacts was validated in a 5 mM $CuSO_4$ phantom consisting of a nylon mesh with 350-μm spacing. The scanning parameters were identical to those used for the in vivo studies. The 3D-radial varying-flip angle technique was verified against a Cartesian varying-TR spin echo acquisition with the following parameters: *TR*=12.5, 25, 50, 100,

200, 400, 800, 1600 ms, matrix size = 128x128 and 1-mm slice at isocenter. The estimated *T1* values were compared using a two-tailed t-test.

4.4.2 Validation of acquisition and reconstruction

Keyhole imaging is based on the premise that image intensity is encoded at the center of k-space. To test the validity of this assumption in 3D and particularly the effect on spatial resolution, the same raw data acquired on the nylon mesh phantom were reconstructed with the filters presented in Eqn. 9. These images are compared in Figure 18. Figure 18(a) shows an image of the phantom reconstructed using the views acquired in all interleaves. This image represents the ground truth with respect to spatial resolution. Figure 18(d) demonstrates the loss of high-frequency information when the UND filter is applied to the raw data. After the data in the periphery of k-space are added in the reconstruction of the images using the UFC or VFC filter, it is clear from Figure 18(b, c) that the spatial resolution is recovered. A decrease of approximately 40% in the signal-to-noise ratio (SNR) is seen when comparing the fully sampled image in Figure 18(a) with the radial keyhole images reconstructed with the VFC and UND filters and a decrease of 20% when comparing with the UFC reconstructed image. No significant SNR difference was observed between the images reconstructed with the VFC and UND filters.

The second row in Figure 18 presents the absolute difference between the fully sampled and the respective radial keyhole image shown in the first row. In the difference images of Figure 18(e, f), background noise levels are equal to or higher than signal values indicating that indeed the majority of image intensity lies at the inner sphere of radius f_N in k-space. This result was also verified in vivo.

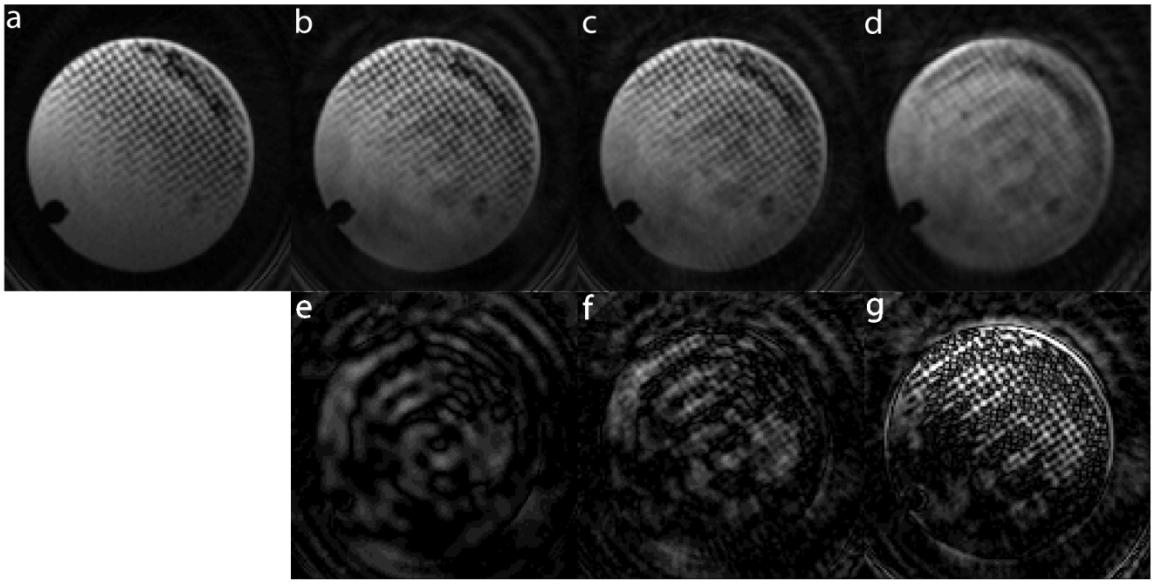

Figure 18: Effect of radial keyhole reconstruction on spatial resolution. (a) Fully sampled, (b) UFC filtered, (c) VFC filtered, and (d) UND filtered reconstructions. The second row (e-g) shows the absolute difference between the fully sampled and the respective radial keyhole image shown in the first row. The spacing in the nylon mesh and pixel size is 350 μm and 160 μm, respectively. Keyhole reconstruction with projection acquisition is a feasible technique for imaging at the theoretical Nyquist spatial resolution (~2.3 * pixel size). A maximum SNR decrease of 40% is seen when comparing the fully sampled image with the radial keyhole images.

The *T1* values of the copper sulfate solution estimated with the Cartesian spin-echo sequence and with the variable flip-angle acquisition using the 3D-radial sampling

method were found to be respectively 161±53 ms and 152±12 ms. At the 5% significance level, these values are not significantly different. Vautier et al. have found similar results (Vautier, Heilmann et al. 2010).

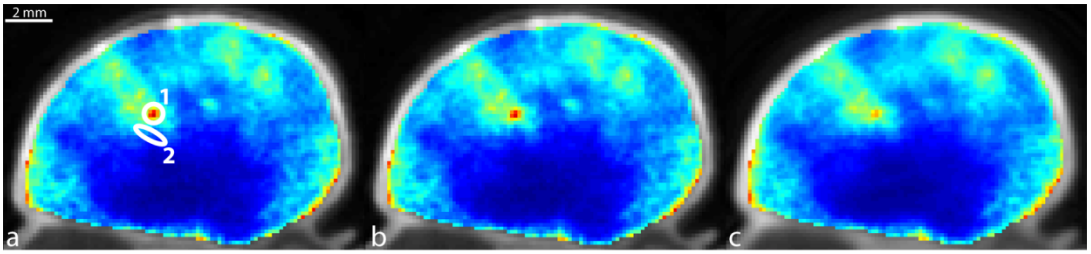

Figure 19: K^{trans} map overlayed on the grayscale image reconstructed with (a) UFC, (b) VFC, and (c) UND filtering. Regions 1 and 2, where the time-intensity curves of Figure 20 were measured, were selected in a fast-enhancing and a slow-enhancing location respectively. K^{trans} values calculated from the 4D images reconstructed with each of the radial keyhole filters were not significantly different from each other in these locations (Table 5).

The in vivo native *T1* values obtained in this study were consistent with the published literature (Yankeelov, Luci et al. 2005; Loveless, Halliday et al. 2012). In the quadriceps femoris muscle group, *T1* was in the range (μ±2σ) 1.43 sec to 2.10 sec, while tumor *T1* was between 2.76 sec and 4.93 sec. Figure 19 presents the K^{trans} map from a central slice in one of the HT-29 tumors overlaid on the grayscale image reconstructed with each of the radial keyhole filters. A region of interest (ROI) of 24 pixels was selected in a fast-enhancing (ROI-1) and a slow-enhancing (ROI-2) region in the tumor. The K^{trans} values calculated from the dynamic volumes reconstructed with the UFC, VFC, and UND filters are listed in Table 5 for comparison. There is no significant difference at the

5% significance level between these values. The normalized time-dependent signal in ROI-1, ROI-2, and a single pixel inside the fast-enhancing region, is plotted in Figure 20 illustrating the time evolution of signal intensity as a function of the k-space filter used for reconstruction.

Table 5: K^{trans} at ROI-1 and ROI-2 (Figure 19) calculated from the 4D volumes reconstructed with the UFC, VFC, and UND filters. At the 5% significance level, there is no significant difference between these values.

	UFC	*VFC*	*UND*
ROI-1	0.045±0.011 min^{-1}	0.045±0.011 min^{-1}	0.043±0.011 min^{-1}
ROI-2	0.027±0.010 min^{-1}	0.027±0.010 min^{-1}	0.029±0.012 min^{-1}

The time-to-peak (TTP) parameter is found as the time in seconds it takes the signal intensity to reach its maximum value. TTP was used a measure of temporal blurring. To assess whether the use of the reconstruction filters resulted in curves with significantly different time-to-peak values, 3D maps of the TTP parameter were generated and compared. The tumor volume was manually segmented and the mask was used to compare the pixels only in the tumor region. As shown previously (Song and Dougherty 2004), reconstructing with the UND filter does not cause temporal blurring: the undersampled 4D dataset represents the ground truth with respect to temporal resolution. The histogram of TTP from a representative animal is shown in Figure 21. A bin-by-bin comparison of the distribution of TTP revealed that the UFC and VFC filters did not lead to significantly different values (Wilcoxon Sign-Rank test at the

5% significance level) as compared to the TTP calculated when UND was used. This finding was confirmed in all tumors studied in this work.

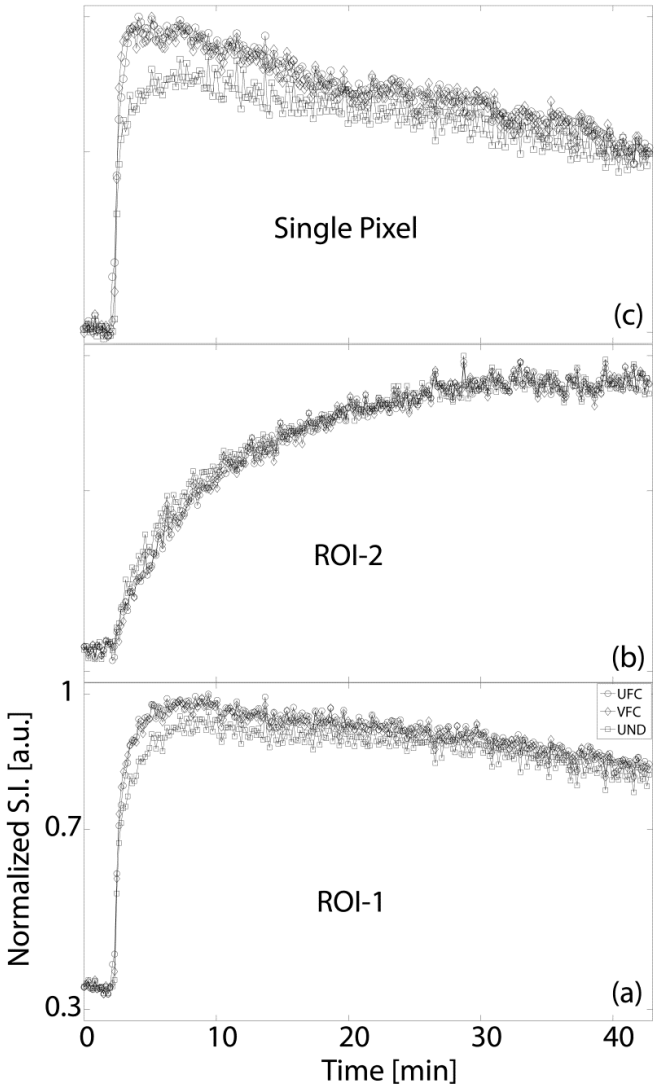

Figure 20: Signal intensity vs. time curves from (a) ROI-1, (b) ROI-2, and (c) a single pixel inside ROI-1 (ROIs shown in Figure 19). The time-to-peak (TTP) signal intensity was used in this study as a measure of temporal blurring. Notice that even though the peak signal value is not necessarily the same between the three filters, TTP does not differ significantly. All plots have the same x- and y-axis range as that shown in panel (a).

A montage of six consecutive slices is shown in Figure 22. Two identical ROIs with an area of 32 pixels were defined at the same location in slice 91 (arrow in Figure 22a) and slice 94 (arrow in Figure 22d). K^{trans} in these regions was 0.013±0.001 min^{-1} and 0.092±0.011 min^{-1} respectively; these values are significantly different from each other (at the 5% significance level). A montage of the histogram of K^{trans} for each respective slice is shown in Figure 23. Care was taken to exclude the fatty tissue surrounding the tumor.

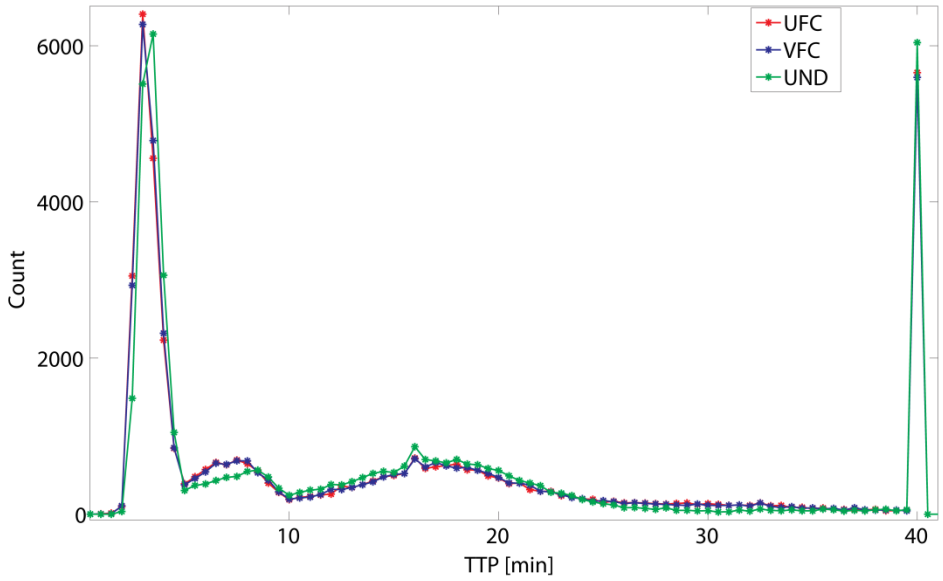

Figure 21: Comparison of TTP histograms when the UFC, VFC, and UND filters were used in reconstruction. TTP calculated with the UND filter was used as the ground truth. In all studied tumors, no significant difference was found between the histograms calculated with either UFC or VFC filtering.

4.5 Discussion

Keyhole imaging can be implemented through several filtering strategies (Song and Dougherty 2004; Altbach, Bilgin et al. 2005) for which the main tradeoff is between

temporal resolution, spatial resolution and sampling artifacts. In general, reduced filtering leads to a decreased level of artifacts, which in turn may introduce temporal blurring. The filtering methods chosen in this study are meant to encompass a wide range of radial keyhole strategies combining the data in the periphery of k-space: in UFC filtering, all interleaves contribute equally to the reconstruction of the high spatial-frequency features in image space and potentially lead to temporal blurring in these regions; VFC filtering is an intermediate strategy in which the contribution to high spatial-frequencies from consecutive time points is slowly, in our case linearly, reduced (for VFC, δ_i in Eqn. 9 assures there is no contribution from the farthest temporal interleaf); as was shown by Song (Song and Dougherty 2004), in UND filtering the absence of keyhole combination does not cause temporal blurring. A comparison of Figure 18(a, b, c, d) reveals that spatial resolution is preserved for UFC filtering and only partially degraded when VFC filtering is employed. The effect of VFC filtering on spatial resolution arises from the fact that in regions of k-space that satisfy $f_N < k_r < f_V$ (V=total number of interleaves) the Nyquist criterion is generally not satisfied. Partial blurring of some of the highest frequency features in image space is demonstrated in the difference image of Figure 18(f).

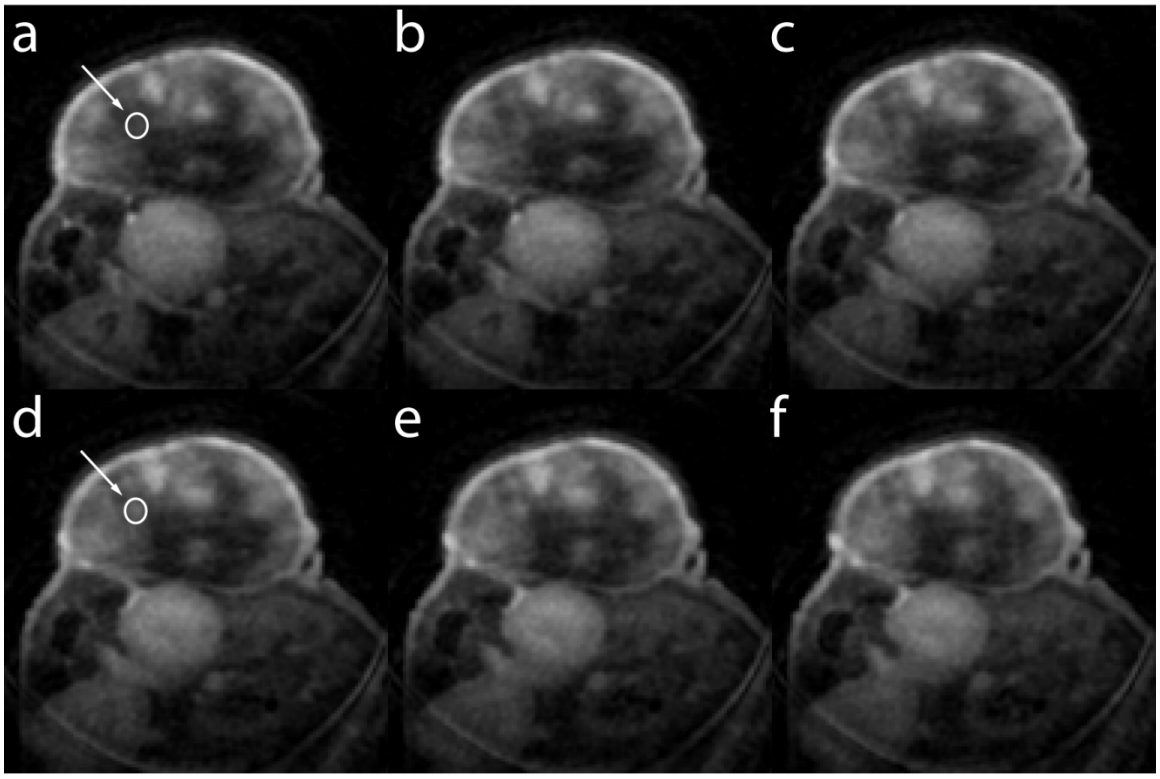

Figure 22: Montage of six consecutive slices (slice 91-96 corresponding to panels a-f). The arrows point to the circular ROIs, selected in slice 91 and 94, where the K^{trans} values were compared. In this case, tumor heterogeneity in the z-direction is being investigated. K^{trans} in these two locations was significantly different. The distance between slices is 160 μm.

The spacing in the nylon meshgrid (350 μm) was chosen because it is approximately equal to the theoretical achievable resolution of the system which is ~2.3 * pixel size due to the effect of the density compensation factors and the Hamming filter (Haacke, Brown et al. 1999). Therefore both radial keyhole filters retain the system resolution at the cost of reduced SNR. As expected, we observe a decrease in SNR since

the amount of raw MR data at the center of k-space, which encodes signal intensity, is reduced by a factor of V_t.

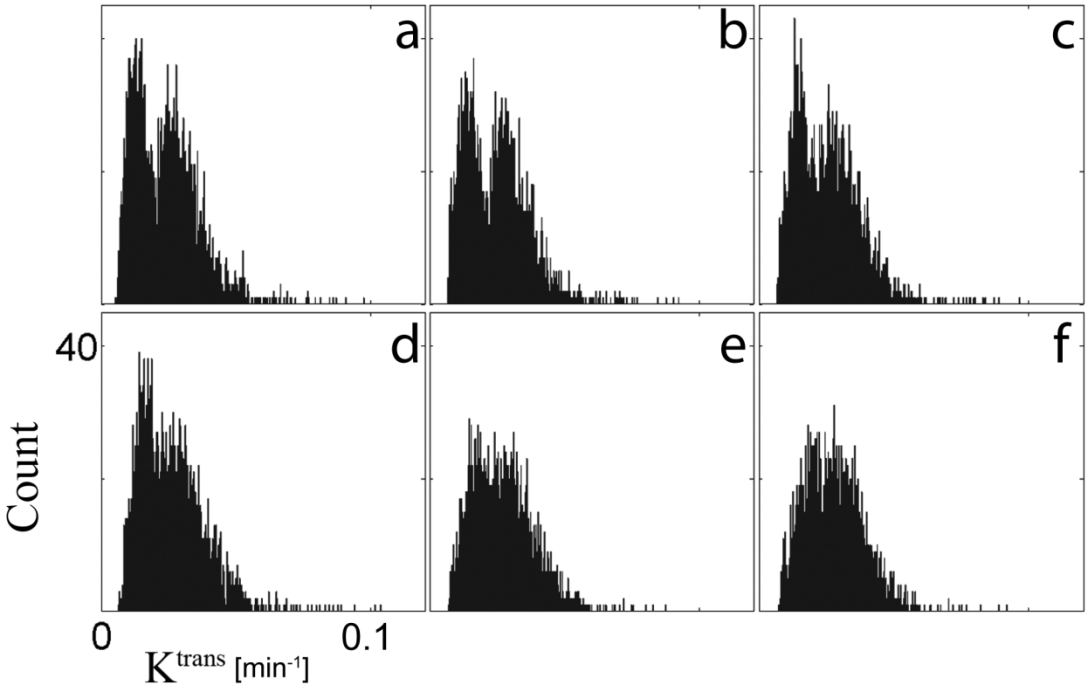

Figure 23: Montage of the histogram of K^{trans} in the tumor region for the respective slices shown in Figure 22. The tumor was manually segmented at each slice. Notice the different distributions in slices 91-93 (a-c) and 94-96 (d-f). All histograms have the same x- and y-axis range as that shown in panel (d).

Methods for sufficient sampling of k-space with non-Cartesian sequences, such as the bit-reversed (BR) or golden-angle (GA) scheme, have been recently compared in the literature (Chan, Ramsay et al. 2012). While it is true that these sampling strategies can provide evenly spaced projections in k-space, they have certain limitations. Both the BR and GA technique are defined for sampling k-space in two dimensions and the extension to 3D is non-trivial. Most importantly, the Archimedean spiral trajectory

described in Eqn. 7 is well suited for 4D contrast-enhanced MRI for these two reasons: first, each interleaf provides a quasi-uniform sampling of the 3D k-space, and second, all combined interleaves provide a quasi-uniform sampling of the 3D k-space. Such distribution of spokes in k-space minimizes the sampling artifacts for each temporally resolved interleaf.

It is well known that perfusion curves can be modeled by a lognormal distribution having a global maximum early in the enhancement stage (Strouthos, Lampaskis et al. 2010). Therefore, a method that causes temporal blurring would result in temporal curves with shifted time-to-peak signal intensities. While the TTP parameter is used extensively in perfusion imaging, in this study it was used as a measure of effective temporal resolution. When compared to the ground truth with respect to temporal resolution, no significant difference was found between the distributions of TTP calculated when either UFC or VFC filtering was used in the reconstruction of the temporally resolved volumes. Hence, these two filters retain the temporal resolution of 9.9 sec achieved with the UND filter. Of critical importance is the finding by Loveless et al. (Loveless, Halliday et al. 2012), which has shown that a population arterial input function can be used when calculating the kinetic parameters of the extended Tofts model. This allows a relaxation of the requirement of very high temporal resolution (usually 1-2 sec) needed for the sampling of the AIF and provides an opportunity for

implementing these 3D keyhole-sampling techniques with a sufficiently high temporal resolution.

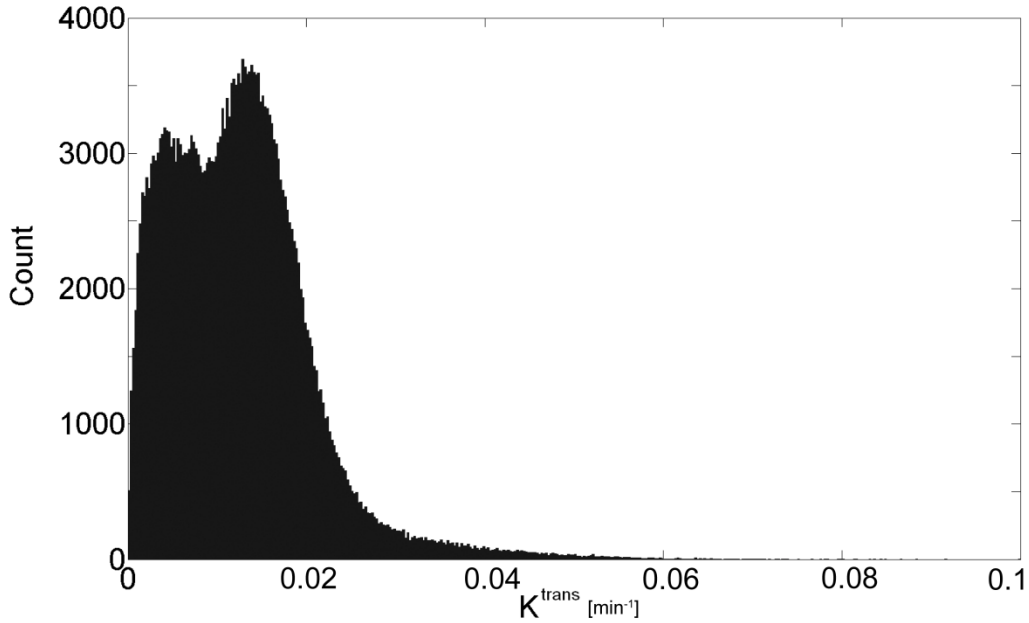

Figure 24: Histogram of K^{trans} over the entire tumor volume. The volume was manually segmented. Care was taken not to include in the segmentation the capsule of fatty tissue surrounding the tumor. The distribution of K^{trans} over this volume is bimodal and skewed to the right. Compare with the distribution of K^{trans} in slices 94-96 (Figure 23d-f)

Given that the voxel size in this study is 160 μm, it is remarkable that K^{trans} is significantly different at the two ROIs shown in Figure 22. More importantly, note that in Figure 23 the histogram of K^{trans} at these regions is drastically different. A bimodal distribution at slice 91 is changed into a skewed Gaussian distribution at slice 94. The results above demonstrate that the heterogeneity in the third dimension (z-direction in this case) is significant and should not be ignored. Bigger voxels may lead to an

incomplete survey of the tumor microenvironment. This finding is further supported in Figure 24. It is clear that the distribution of K^{trans} over the entire tumor volume is bimodal and skewed to the right. If for example, a 2D sampling protocol was employed in the study of the tumor heterogeneity and slice 94 was imaged, the results would not be representative of the true distribution of the kinetic parameters found in the tumor.

Table 6: Minimum value of TTP in tumor volume when UND was used as a reconstruction filter. The temporal sampling interval was 9.9 sec. In all but one of the tumors studied, there are at least seven sample points in the rising portion of the dynamic curve.

Tumor	TTP_{min} [sec]
HT29	237.6
HT29	168.0
Sarcoma	158.4
MX1	148.5
MX1	148.5
MX1	148.5
LoVo	138.6
LoVo	138.6
HT29	79.2
Sarcoma	79.2
Sarcoma	69.3
LoVo	39.6

In vivo experiments of four different tumor types (n=3/type) were undertaken to address the issue of what temporal resolution would be required considering the tradeoffs between temporal and spatial resolution. Our concern was whether the sampling interval (9.9 sec) was sufficiently short to appropriately measure the signal

intensity changes related to contrast exchange kinetics. The 4D volume of each dynamic study was examined on a pixel-by-pixel basis to determine the shortest time to peak in the tumor. The results are shown in Table 6. For all but the last case, there were at least seven samples before reaching the time to peak. We believe the last point was an outlier arising from a motion artifact. For the majority of the tumors there were at least 7 points in the rising portion of the curve - *for the shortest TTP in the entire volume*. Thus, we believe the temporal sampling interval we have used should be sufficient to adequately sample the initial rapidly changing signal in these tumors.

4.6 Conclusions

The study of the heterogeneous microenvironment in tumors necessitates the use of high spatial and temporal resolution DCE-MRI. Radial sampling is less sensitive to motion and flow artifacts. More importantly, this sampling technique lends itself naturally to keyhole reconstruction because of the high oversampling rate at the center of k-space where most of the image intensity is encoded. We have shown here that 4D-radial keyhole imaging is a feasible technique for high resolution DCE-MRI. This technique retains the spatial resolution as compared to a fully sampled dataset and the temporal resolution achieved with an undersampled dataset. An in vivo study reveals tumor regions less than 500 μm apart in the z-direction with significantly different contrast kinetics. The biomarker used in this project was K^{trans}, but the method is also

suitable for the study of other pharmacokinetic parameters. Indeed, it has been suggested that the complexity of the tumor microenvironment needs to be analyzed with biomarkers that are not only sensitive to kinetic parameters, but also to their spatial distribution (Rose, Mills et al. 2009).

Kermode and Tofts (Kermode, Tofts et al. 1988) presented some of the first attempts at quantitative dynamic MRI more than twenty years ago. Since that time, DCE-MRI has found a wide range of applications in the clinical and preclinical arena. Advances in acquisition methods, reconstruction, and hardware have lead to great improvements in spatial and temporal resolution. Kim et al. (Kim, Folks et al. 2011) have reported a protocol with a voxel size of 0.23x0.23x1 mm^3 and temporal resolution of 58.9 sec while Loveless et al. (Loveless, Halliday et al. 2012) achieved a temporal resolution of 1.5 sec with a voxel of 0.39x0.39x2 mm^3. If the product of voxel size and temporal resolution is used as the figure of merit, the work here presents an improvement by more than an order of magnitude over that previously reported. Currently, no unified protocol exists for the implementation of a DCE-MRI experiment in the preclinical domain. We believe the proposed technique satisfies some of the spatial/temporal resolution requirements for preclinical DCE-MRI and may serve as a reference for future efforts in standardization.

5. An Analysis of the Uncertainty and Bias in DCE-MRM Measurements

5.1 Outline

The pharmacokinetic parameters derived from dynamic contrast-enhanced (DCE) MRI have been used in more than 100 phase I trials and investigator led studies. A comparison of the absolute values of these quantities requires an estimation of their respective probability distribution function (PDF). The statistical variation of the DCE-MRI measurement is analyzed by considering the fundamental sources of error in the MR signal intensity acquired with the spoiled gradient-echo (SPGR) pulse sequence.

The variance in the SPGR signal intensity arises from quadrature detection and excitation flip angle inconsistency. The noise power was measured in eleven phantoms of contrast agent (CA) concentration in the range $[0\text{-}1]$ mM (in steps of 0.1 mM) and in one in vivo acquisition of a tumor-bearing mouse. The distribution of the flip angle was determined in a uniform 10 mM $CuSO_4$ phantom using the spin echo double angle method. The PDF of a wide range of $T1$ values measured with the varying flip angle (VFA) technique was estimated through numerical simulations of the SPGR equation. The resultant uncertainty in contrast agent concentration was incorporated in the most common model of tracer exchange kinetics and the PDF of the derived pharmacokinetic parameters was studied numerically.

The VFA method is an unbiased technique for measuring $T1$ only in the absence of bias in excitation flip angle. The time-dependent concentration of the contrast agent measured in vivo is within the theoretically predicted uncertainty. The uncertainty in measuring the DCE-MRI parameters with SPGR pulse sequences is of the same order, but always higher than, the uncertainty in measuring the pre-injection longitudinal relaxation time ($T1_0$). The fractional volume parameters derived from the extended Tofts model were found to be more sensitive than K^{trans} to the variance in signal intensity. The SNR of the pre-injection $T1$ map indicates the limiting precision with which the DCE-MRI parameters can be estimated.

Current small-animal imaging systems and pulse sequences robust to motion artifacts have the capacity for reproducible quantitative acquisitions with DCE-MRI. In these circumstances, it is feasible to achieve a level of precision limited only by physiologic variability.

5.2 Introduction

Dynamic contrast-enhanced (DCE) MRI provides a noninvasive measurement of the time-dependent concentration of an injected contrast agent (CA). The kinetic curves observed in the tissue of interest are subsequently incorporated into a pharmacologic model describing the underlying physiologic process. This method is used extensively in the measurement of hemodynamic parameters. The most widely reported measures are

the rate of transport of the CA across the endothelium barrier (K^{trans}, k_e), the fractional volume of the extravascular-extracellular space (v_e), the fractional volume of the plasma space (v_p), and the initial area under the contrast concentration curve (AUC). In tumor studies, the pharmacokinetic models, their respective measures, and the conditions under which the outputs may be correctly interpreted, have been recently reviewed in detail (Sourbron and Buckley 2011).

In the clinical domain, more than 100 phase I trials and investigator led studies of anti-angiogenic and vascular-disrupting therapeutic agents have incorporated as end-points the functional parameters from DCE-MRI (O'Connor, Jackson et al. 2012). The reported therapeutic effects are in the range of $5\% - 97\%$ decrease in K^{trans}, $27\% - 50\%$ decrease in v_p, and $36\% - 50\%$ decrease in AUC (O'Connor, Jackson et al. 2012).
A comparison of the absolute values of these quantities requires an estimation of their respective probability distribution functions (PDF). Such knowledge is critical in selecting the appropriate statistical test for determining significance and confidence intervals. The estimation of the PDF from a region of interest (ROI) in the image may be incorrect given that tumors exhibit a highly heterogeneous spatial distribution of the DCE-MRI parameters (Subashi, Moding et al. 2013).

The aim of this work is to determine the statistical variation of the pharmacokinetic parameters measured with DCE-MRI. The probability density function

of these measures is estimated by analyzing the fundamental sources of error in the MR signal acquired with the spoiled gradient-echo (SPGR) pulse sequence. These results extend and complement previous research studying the uncertainty in measuring the contrast agent concentration (Schabel and Parker 2008) and the functional DCE-MRI parameters (Kershaw and Buckley 2006; Barnes, Whisenant et al. 2013).

5.3 Materials and Methods

5.3.1 Theory

The magnitude of the SPGR signal at pixel $\vec{\boldsymbol{r}} = (x, y, z)$ is given by

$$S(\vec{\boldsymbol{r}}, \alpha, TR, TE) = S_0(\vec{\boldsymbol{r}}) \frac{\sin\left(\alpha(\vec{\boldsymbol{r}})\right)\left(1 - e^{-TR/T1(\vec{\boldsymbol{r}})}\right)}{1 - cos(\alpha(\vec{\boldsymbol{r}}))e^{-TR/T1(\vec{\boldsymbol{r}})}} e^{-TE/T2^*(\vec{\boldsymbol{r}})} \qquad \textbf{Eqn. 16}$$

where $S_0(\vec{\boldsymbol{r}})$ is proportional to the equilibrium longitudinal magnetization and the system gain function. The $T2^*$ term is assumed to equal unity. In this study, TE=0.02 ms; for the typical values of $T2^*$ found in tumors (Vautier, Heilmann et al. 2010), the error arising from the above assumption is <0.1%. Eqn. 16 can then be linearized voxel-wise as

$$\frac{S(\alpha, TR)}{\sin(\alpha)} = E1\frac{S(\alpha, TR)}{\tan(\alpha)} + S_0(1 - E1)$$
$$E1 = \exp\left(-TR/T1\right) \qquad \textbf{Eqn. 17}$$

A varying flip-angle acquisition (VFA) with $\alpha = \{\alpha_1, \ldots, \alpha_N\}$ and fixed TR is used to measure $S(\alpha_i)$. The $T1$ and S_0 maps are obtained by solving

$$\vec{\boldsymbol{y}} = m \cdot \vec{\boldsymbol{x}} + b$$

$$y_i = \frac{S_i}{sin(\alpha_i)}, \qquad x_i = \frac{S_i}{tan(\alpha_i)}, \qquad i = 1, \dots, N \qquad \textbf{Eqn. 18}$$

$$m = E1, \qquad b = S_0(1 - E1)$$

The magnitude of $S(\vec{\boldsymbol{r}}, \alpha, TR, TE)$ follows a Rician distribution. If $SNR > 5$,

$$S(\vec{\boldsymbol{r}}, \alpha, TR, TE) \sim N\left(\sqrt{\hat{S}^2 + \sigma^2}, \sigma\sqrt{\frac{2}{4-\pi}}\right) \qquad \textbf{Eqn. 19}$$

where $N(\cdots)$ denotes the normal distribution, $\hat{S}$ is the true pixel intensity determined from Eqn. 16, and σ^2 is the noise power of the real and imaginary acquisition channels (Gudbjartsson and Patz 1995; Macovski 1996). The noise power can be measured independently in an artifact-free image with no NMR signal (Gudbjartsson and Patz 1995). In the absence of flow and susceptibility artifacts, Eqn. 19 characterizes the noise properties of the MR signal to an accuracy of better than 2% (Henkelman 1985).

The mean value of the magnitude of the SPGR signal is dependent on three system variables: $S_0(\vec{\boldsymbol{r}})$, TR, and α. We assume the gain function contained in $S_0(\vec{\boldsymbol{r}})$ is uniform and the timing parameters TR/TE are known with absolute certainty. The spatial distribution of the excitation flip angle (α) is determined by the amplitude and shape of the $\overrightarrow{\boldsymbol{B1}}$ field. In turn, the distribution of the $\overrightarrow{\boldsymbol{B1}}$ field is a function of the shape of the object being scanned, its electromagnetic properties, the resonance frequency (main magnetic field), and the polarization of the radiofrequency coil (Glover, Hayes et al.

1985). For a given object, $\overrightarrow{\boldsymbol{B1}}(\vec{\boldsymbol{r}})$, and hence $\alpha(\vec{\boldsymbol{r}})$, can be measured with a spin-echo pulse sequence using the double angle method (DAM) (Stollberger and Wach 1996). This technique has the advantage of being independent of the coil sensitivity; its main disadvantage is the impractically long scan time.

Given a fixed set of imaging parameters, after the injection of a contrast agent, the signal intensity from the SPGR sequence is only a function of the time-varying $T1$. Using the formalism of Schabel et al., the relative signal enhancement is given by (Schabel and Parker 2008)

$$\Xi = \frac{\mathrm{S(T1)} - \mathrm{S(T1_0)}}{\mathrm{S(T1_0)}} = \frac{(\mathrm{E1} - \mathrm{E1_0})(\cos(\alpha) - 1)}{(\mathrm{E1_0} - 1)(\mathrm{E1}\cos(\alpha) - 1)} \qquad \textbf{Eqn. 20}$$

with the subscript denoting the native (pre-injection) quantities. Eqn. 20 may be readily solved for the relaxation rate $R1 = 1/T1$

$$\mathrm{R1} = -\frac{1}{\mathrm{TR}}\log\left[\frac{\Xi(\mathrm{E1_0} - 1) + \mathrm{E1_0}(1 - \cos(\alpha))}{1 + \cos(\alpha)(\Xi(\mathrm{E1_0} - 1) - 1)}\right] \qquad \textbf{Eqn. 21}$$

In the fast exchange limit, the functional dependence of the CA concentration on the longitudinal relaxation rate is (Landis, Li et al. 2000)

$$\mathrm{C} = \frac{1}{\mathrm{r_1}}(\mathrm{R1} - \mathrm{R1_0}) \qquad \textbf{Eqn. 22}$$

where $\mathrm{r_1}$ is the longitudinal relaxivity of the injected contrast agent.

The temporal evolution of the concentration of the contrast agent is widely believed to arise from a two compartment exchange system described by the extended Tofts model (Tofts 1997)

$$C(t) = v_p \cdot C_p(t) + K^{trans} \int_0^t C_p(u) \cdot e^{-(K^{trans}/v_e)\cdot(t-u)} du \qquad \textbf{Eqn. 23}$$

where $C_p(t)$ is the arterial input function (AIF), v_p is the fractional volume of the plasma compartment, v_e is the fractional volume of the extravascular-extracellular space (EES), and K^{trans} is the rate constant for the transfer of the contrast agent from plasma to EES measured in ml/s of contrast agent per ml of tissue. Equation (8) can be written in matrix form (Murase 2004)

$$\vec{\boldsymbol{B}} = \vec{\boldsymbol{A}}^{-1} \cdot \vec{\boldsymbol{C}}$$

$$\vec{\boldsymbol{A}} = \begin{pmatrix} \int_0^{t_1} C_p(u)du & -\int_0^{t_1} C(u)du & C_p(t_1) \\ \int_0^{t_2} C_p(u)du & -\int_0^{t_2} C(u)du & C_p(t_2) \\ \vdots & \vdots & \vdots \\ \int_0^{t_n} C_p(u)du & -\int_0^{t_n} C(u)du & C_p(t_n) \end{pmatrix} \qquad \textbf{Eqn. 24}$$

$$\vec{\boldsymbol{B}} = \begin{pmatrix} K^{trans} + \left(K^{trans}/v_e\right) \cdot v_p \\ K^{trans}/v_e \\ v_p \end{pmatrix}, \qquad \vec{\boldsymbol{C}} = \begin{pmatrix} C(t_1) \\ C(t_2) \\ \vdots \\ C(t_n) \end{pmatrix}$$

where n is the total number of time points.

5.3.2 Simulations

In DCE-MRI, the concentration of the contrast agent is only a function of the change in the longitudinal relaxation time. Thus, the accuracy and precision of the pharmacokinetic parameters derived from this technique depend on the accuracy and precision with which $T1$ can be measured. Based on Eqn. 22, two separate terms need to be considered: the statistical variation in the measurement of $T1_0$ and the statistical variation in the measurement of the change in $T1$.

The VFA method is able to provide accurate and precise measurements of $T1_0$ using two pre-determined nutation angles (Deoni, Rutt et al. 2003). The pair of flip angles is chosen such that the variance of a single $T1_0$ is minimized. A variable degree of precision would be achieved in-vivo given that a range of relaxation times are measured. Consider a single pixel at position $\vec{\boldsymbol{r}} = (x, y, z)$ with a true longitudinal relaxation $\hat{T}1_0$ and equilibrium magnetization $\hat{S}_0$. Assume that at this location α arises from a distribution D_α. Given the prescribed flip angle $\hat{\alpha}$, we represent

$$\alpha_{SNR} = \frac{\mu_{D_\alpha}}{\sigma_{D_\alpha}}$$

$$\delta\alpha = \frac{\mu_{D_\alpha} - \hat{\alpha}}{\hat{\alpha}} \qquad \textbf{Eqn. 25}$$

where μ_{D_α} and σ_{D_α} equal the mean and the standard deviation of D_α. In this context, the quantity α_{SNR} describes the precision of attaining $\hat{\alpha}$, while $\delta\alpha$ is a measure of the accuracy (bias). Under these conditions, we are interested in determining the probability

distribution function of $\hat{T}1_0$. An analytic expression for error propagation when inverting a matrix (Eqn. 18) with elements of unequal variance in not known. Hence, the PDF of $\hat{T}1_0$ in the range $[100 - 4000]$ ms (in steps of 50 ms) was estimated through numerical simulations of Eqn. 18 with $\alpha = \{2^o, 10^o\}$. The distribution of the signal intensity at position $\vec{\boldsymbol{r}}$ was calculated using Eqn. 16 and Eqn. 19, with the flip angle distribution described by Eqn. 25. The simulation was repeated 10^6 times.

The degree of uncertainty and bias in concentration measurements using the SPGR pulse sequence has been previously studied in detail (Schabel and Parker 2008). The variance of the concentration (σ_C^2) is calculated by

$$\sigma_C^2 = \frac{1}{N_B}\frac{(E1\cos(\alpha)-1)^4}{(SNR\cdot\beta)^2}\left(\left(\frac{E1-1}{E1\cos(\alpha)-1}\right)^2+\left(\frac{E1_0-1}{E1_0\cos(\alpha)-1}\right)^2\right) \qquad \textbf{Eqn. 26}$$

$$\beta = r_1\, TR\, E1\,(\cos(\alpha)-1)$$

where N_B is the number of baseline scans (number of pre-injection scans) and SNR is the signal-to-noise ratio of the imaging sequence. Note that Eqn. 26 assumes the contrast agent does not change $T2^*$. A bias in the native longitudinal relaxation ($\delta T1_0$) or in the excitation flip angle ($\delta\alpha$) would lead to a bias in the calculation of the concentration:

$$\delta C_{T10} = \delta T1_0\frac{\partial C}{\partial T1_0}, \qquad \delta C_\alpha = \delta\alpha\frac{\partial C}{\partial \alpha} \qquad \textbf{Eqn. 27}$$

The partial derivatives are obtained by implicit differentiation of Eqn. 20.

Finally, assume that at the pixel in position $\vec{\boldsymbol{r}}$, the pharmacokinetic parameters are given by the triplet $\left(\hat{K}^{trans}, \hat{v}_e, \hat{v}_p\right)$. Using the population AIF reported by Loveless *et.*

al,. (Loveless, Halliday et al. 2012) the true time-varying concentration $\hat{C}(t)$ was calculated using Eqn. 23. The measured concentration was then assumed to arise from

$$C(t_i) \sim N\left(\left(\hat{C}(t_i) + \delta\hat{C}(t_i)_{T10} + \delta\hat{C}(t_i)_{\alpha}\right), \sigma_{\hat{C}(t_i)}\right)$$
$$Cp(t_i) \sim N\left(\left(\widehat{Cp}(t_i) + \delta\widehat{Cp}(t_i)_{T10} + \delta\widehat{Cp}(t_i)_{\alpha}\right), \sigma_{\widehat{Cp}(t_i)}\right) \quad \textbf{Eqn. 28}$$

Eqn. 28 was used to generate 10^4 different $C(t)$ and $C_p(t)$ curves. The imaging parameters were: $TR/TE = 5/0.02$ ms, $NEX = 1$, $\alpha = 10^o$, $N_B = 12$, and 10 sec temporal resolution. The probability distribution function of the triplets was determined by solving Eqn. 24.

5.3.3 Measurements

Experiments were performed on a $7T$ small-animal, MRI scanner (Bruker BioSpin MRI GmbH, Ettlingen, Germany) equipped with self-shielded gradient coils having a maximum gradient strength of 450 mT/m and rise time of 110 μs. An actively detuned volume excite RF-coil was used in conjunction with a four-element array coil for surface receive.

The pulse sequence and the k-space sampling strategy used in this study have been described elsewhere (Subashi, Moding et al. 2013). The acquisition parameters were: FOV = 20 mm^3, $matrix = 128^3$, $TR/TE = 5/0.02$ ms, $NEX = 1$, $\alpha = 10^o$, and 10 sec temporal resolution. A rect pulse with a length of 20 μs was used for excitation. The raw data from each channel in the four-element array coil were separately

reconstructed using the re-gridding method and combined with the Sum-of-Squares technique (Roemer, Edelstein et al. 1990). The pre-injection longitudinal relaxation time was measured with the variable flip-angle acquisition using the same acquisition parameters and $\alpha = \{2^o, 10^o\}$. The noise power of the sequence with the above parameters was measured in eleven phantoms of CA concentration in the range $[0 - 1]$ mM (in steps of 0.1 mM) and in one in-vivo acquisition of a tumor-bearing mouse. The range of phantom concentrations was chosen to be representative of the range encountered in a typical small animal DCE-MRI study (Subashi, Moding et al. 2013).

The distribution of the flip angle was measured in a uniform 10 mM $CuSO_4$ phantom using the spin echo double angle method (DAM) with the following parameters: FOV = 20 mm^3, $matrix = 128\ x\ 128\ x\ 100$, $TR/TE = 4000/25$ ms, $NEX = 20$, $\alpha = \{40^o, 80^o\}$. A rect pulse with a length of 20 μs was used for excitation and refocusing. The DAM acquisition was repeated with $\alpha = \{30^o, 60^o\}$ for comparison with the $\alpha = \{40^o, 80^o\}$ results.

All animal studies were approved by the Duke University Institutional Animal Care and Use Committee. A DCE-MRI dataset was acquired in a tumor-bearing (tumor volume ≈ 470 μL) *nu/nu* mouse with the LS174t cell line implanted in the mammary fat pad (Charles River Laboratories Wilmington, MA). A custom-made animal positioning system was used to maintain the mouse under anesthesia by isoflurane delivery via a

nose cone. Body temperature was controlled between 36 °C and 37 °C by circulating warm water. The contrast agent was injected after the acquisition of twelve baseline scans ($N_B = 12$); dynamic imaging lasted for approximately 20 min post-injection. An automatic syringe pump (KD Scientific Inc., Holliston, MA) provided a consistent contrast injection. Gd-DTPA (Magnevist, Schering AG, Berlin, Germany) was administered as a bolus via a 27-gauge tail vein catheter at a dose of 0.5 mmol/kg and flow rate of 2.4 mL/min as described by Loveless et al. (Loveless, Halliday et al. 2012). At 7 T, the longitudinal relaxivity of Magnevist in blood plasma is r_1=3.275 $mM^{-1}s^{-1}$ (Noebauer-Huhmann, Szomolanyi et al. 2010).

5.4 Results

5.4.1 Uncertainty and bias in *T1* measurements

The mean value of the SPGR signal is dependent on three system variables: $S_0(\vec{r})$, TR, and α. The distribution of the signal is dependent on the noise power and the distribution of the flip angle. Figure 25(a) shows a representative histogram of the signal intensity in an artifact-free background region, while Figure 25(b) plots the flip angle distribution measured with the spin echo DAM. In phantoms with varying Magnevist concentration, the standard deviation of the noise was found to be $\sigma = (0.057 \pm 0.002)\%$ of the mean of S_0. The distribution of the flip angle measured in the $CuSO_4$ phantom is described by

$$\alpha_{SNR} \approx 30, \qquad \overline{\delta\alpha} \approx +10\% \qquad \textbf{Eqn. 29}$$

Figure 25(c) displays the estimated PDF of $T1_0$ in a single pixel with $\hat{T}1_0 = 2000$ ms for two cases: no bias in flip angle ($\alpha_{SNR} \approx 30,\ \delta\alpha = 0$) and distribution described by Eqn. 29. Notice that a flip angle bias would not only bias the mean of $T1_0$, but it would also decrease the precision with which it can be measured.

The estimated probability distribution function of $T1_0$ was characterized by two main parameters

$$T1_{SNR} = \frac{\mu_{D_{T1}}}{\sigma_{D_{T1}}}$$
$$\delta T1 = \frac{\mu_{D_{T1}} - \hat{T}1_0}{\hat{T}1_0} \qquad \textbf{Eqn. 30}$$

where D_{T1} represents the PDF of $T1_0$, $\mu_{D_{T1}}$ is the mean, $\sigma_{D_{T1}}$ is the standard deviation, and $\hat{T}1_0$ is the true longitudinal relaxation rate. The quantity $T1_{SNR}$ is an indicator of the precision of the $\hat{T}1_0$ measurement technique, while $\delta T1$ describes its accuracy (bias). The asymmetry of the PDF was studied through an analysis of the skewness of D_{T1}.

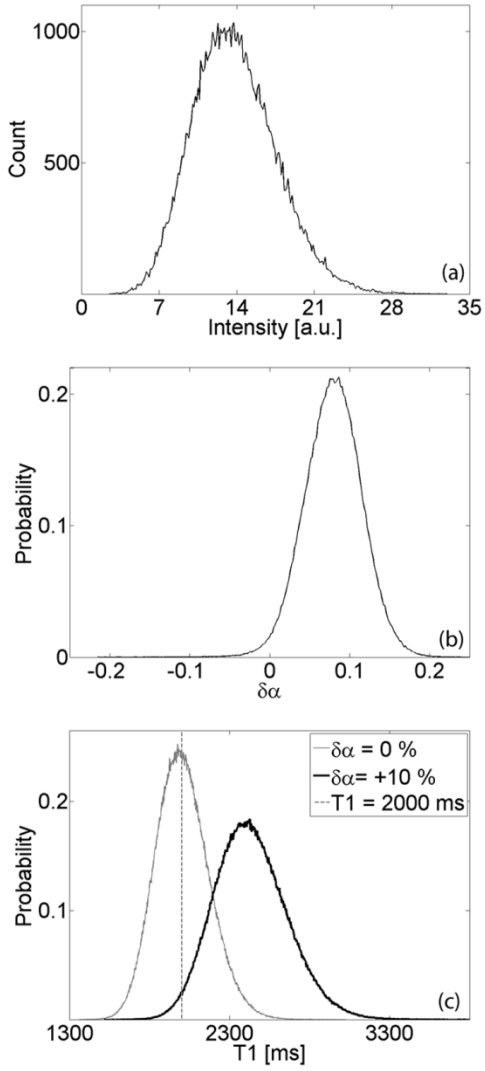

Figure 25: (a) Representative histogram of signal intensity in artifact-free background ROI (region with no NMR signal). The noise power equals the variance of the measured distribution. (b) Distribution of excitation flip angle (referenced with respect to prescribed flip angle) measured in uniform $CuSO_4$ phantom. (c) Estimated PDF of $T1_0$ in a single pixel with $\widehat{T1}_0$=2000 ms for two cases: no bias in flip angle (α_{SNR}≈30, $\delta\alpha$=0) and distribution given in panel (b).

The variance of the $T1_0$ distribution estimated numerically was compared with the variance of the distribution measured in 11 uniform phantoms of increasing longitudinal relaxation rate. Figure 26(a) depicts the measured histogram of $T1_0$ in an

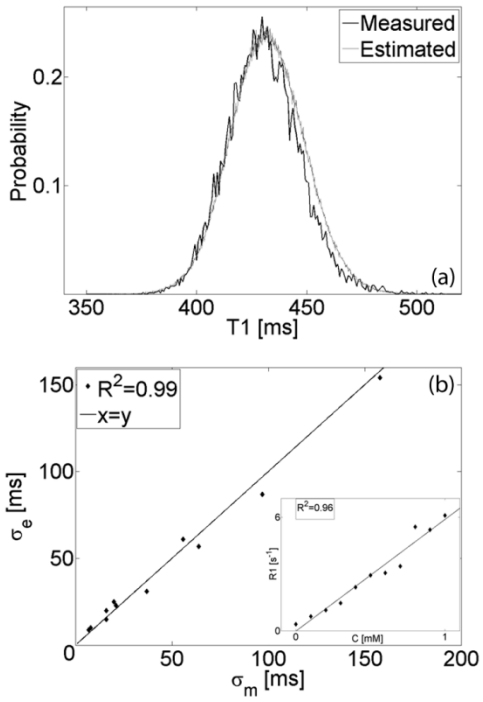

Figure 26: (a) Comparison of $T1_0$ distribution estimated numerically with distribution measured in an ROI of ≈10^4 pixels in uniform phantom. (b) Estimated (σ_e) vs. measured (σ_m) $T1_0$ standard deviation in phantoms with increasing CA concentration (inset shows relation between the concentration C [mM] and measured relaxation rate R1 [s^{-1}]).

ROI of $\approx 10^4$ pixels and the estimated PDF of a single pixel with the same mean $T1_0$. The estimated standard deviation (σ_e) is plotted in Figure 26(b) as a function of the standard deviation measured (σ_m) in phantoms with increasing CA concentration (inset shows relation between the concentration C $[mM]$ and measured relaxation rate R1 [s^{-1}]).

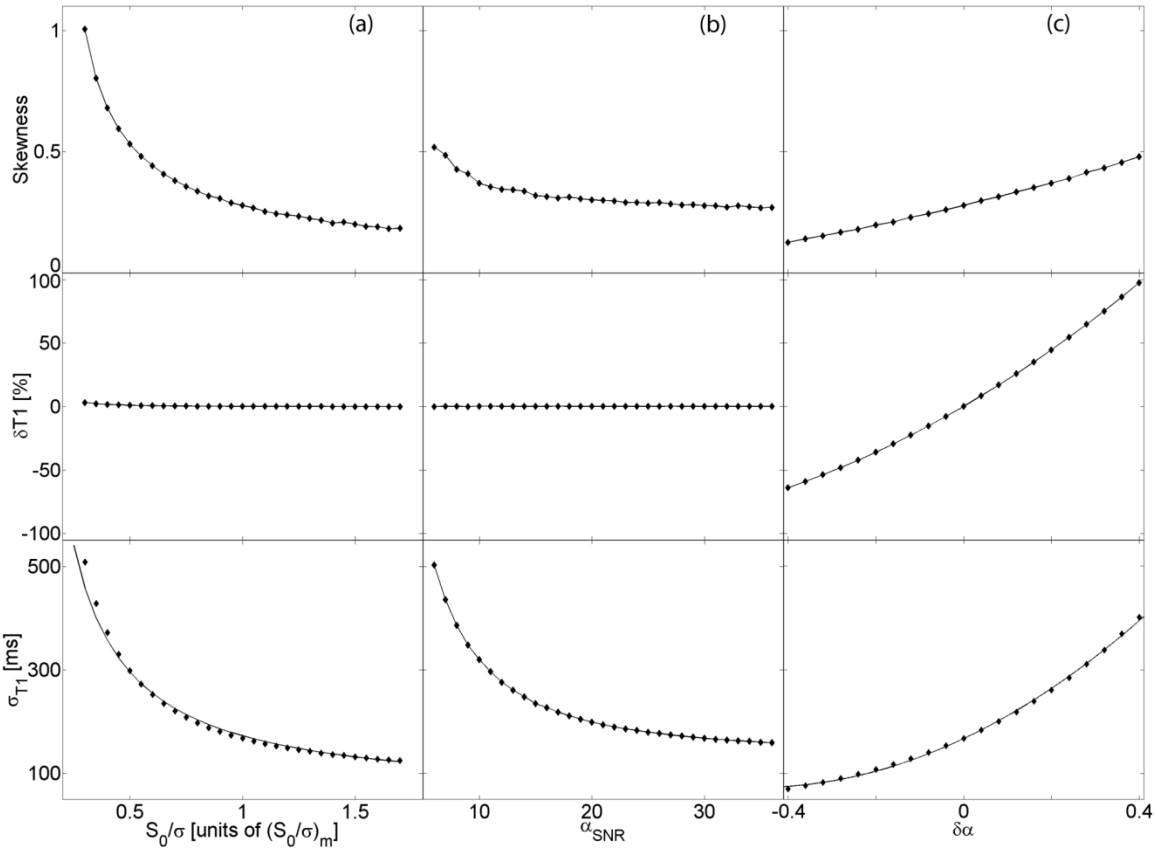

Figure 27: (a) Uncertainty and bias in $T1_0$ measurements as a function of (a) intrinsic SNR, (b) flip angle uncertainty, and (c) flip angle bias. Graphs in each column have the same x-axis as the respective lower graph; graphs in each row have the same y-axis as the respective leftmost graph.

The uncertainty and bias in the measurement of the spin-lattice relaxation time arises from the distribution of the SPGR signal intensity. This dependence was studied by numerical simulations of Eqn. 18 and the results are described in Figure 27 and Figure 28. In the context of DCE-MRI, since the contrast agent does not have an effect on the equilibrium magnetization, we define the measured ratio

$$\left(\frac{\sigma}{S_0}\right)_m \approx 0.057\ \% \qquad \textbf{Eqn. 31}$$

as the intrinsic SNR of the pulse sequence (with the specific image acquisition parameters listed above). Figure 27 examines the standard deviation, percent deviation, and the skewness of the PDF of $\hat{T}1_0 = 2000$ ms in the presence of varying intrinsic SNR, α_{SNR}, and flip angle bias. Figure 27(a) shows the effect of the intrinsic SNR assuming the flip angle is known with absolute certainty. The flip angle uncertainty is subsequently added to the simulation revealing the dependence in Figure 27(b). Lastly, we incorporate a flip angle bias and demonstrate the effect on $T1_0$ measurements in Figure 27(c). This analysis is extended to longitudinal relaxation times in the range $\hat{T}1_0 = [100 - 4000]$ ms as shown in Figure 28.

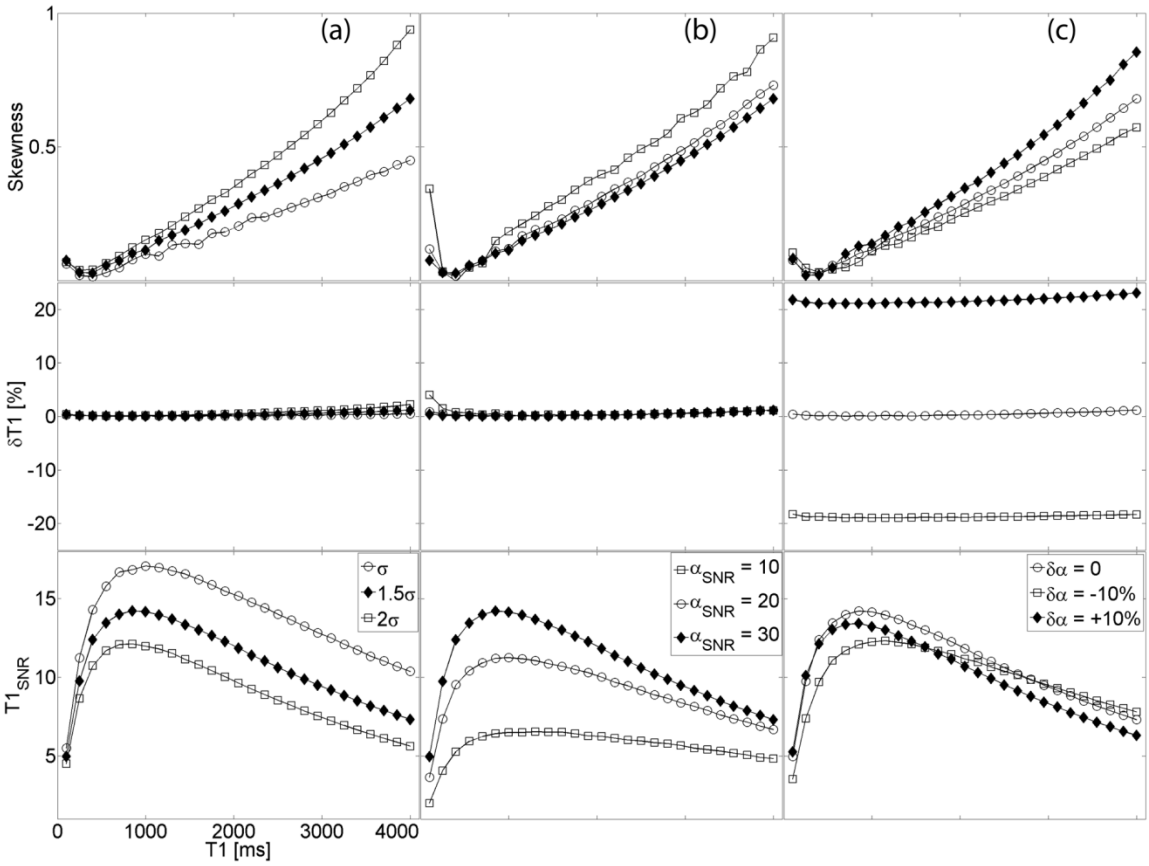

Figure 28: (a) Uncertainty and bias in $T1$ measurements as a function of longitudinal relaxation time in the presence of varying (a) noise power, (b) flip angle uncertainty, and (c) flip angle bias. All graphs have the same x-axis; the legends in the bottom row are column-specific.

5.4.2 Uncertainty and bias in DCE-MRI parameters

The noise power in the in-vivo acquisition was in the range of the noise measured in the phantoms with varying contrast agent concentration. The intrinsic SNR was found to be $(\sigma/S_0)_m \approx 0.056$ %. The pre-injection longitudinal relaxation time in the tumor volume (manually segmented to exclude fatty tissue in the encapsulating epithelial sack) was in the range $(\mu \pm 2\sigma)$ $1.58 - 2.88$ sec. Figure 29(a) presents an

overlay of the K^{trans} map on a contrast-enhanced $T1$-weighted image from a central slice in the tumor. The time dependence of the CA concentration in a single pixel (arrow) is plotted in Figure 29(b). The predicted curve obtained by solving Eqn. 23 and the uncertainty estimated by Eqn. 26 are superimposed on the measured concentration curve. Note that the graphs depicting the uncertainty ($\pm 2\sigma$) were calculated using the concentration curve found by solving the pharmacokinetic model in Eqn. 23.

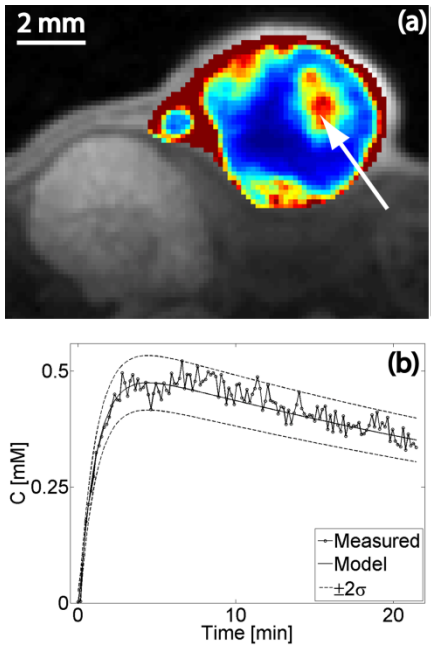

Figure 29: (a) Overlay of K^{trans} map on a contrast-enhanced T1-weighted image from a central slice in the tumor. (b) Time-varying contrast agent concentration in a single pixel (arrow in panel (a)). The predicted curve obtained by solving Eqn. 23 and the uncertainty estimated by Eqn. 26 are superimposed on the measured concentration curve.

The probability distribution function of the CA concentration curve was used to estimate the uncertainty of the pharmacokinetic parameters measured with DCE-MRI.

Figure 30(a) demonstrates the effect of flip angle bias (and consequently $T1$ bias) on a single pixel with $K^{trans} = 0.2\ \text{min}^{-1}$ while Figure 30(b) compares the coefficient of variation of the DCE-MRI parameters to the coefficient of variation of $\hat{T}1_0$.

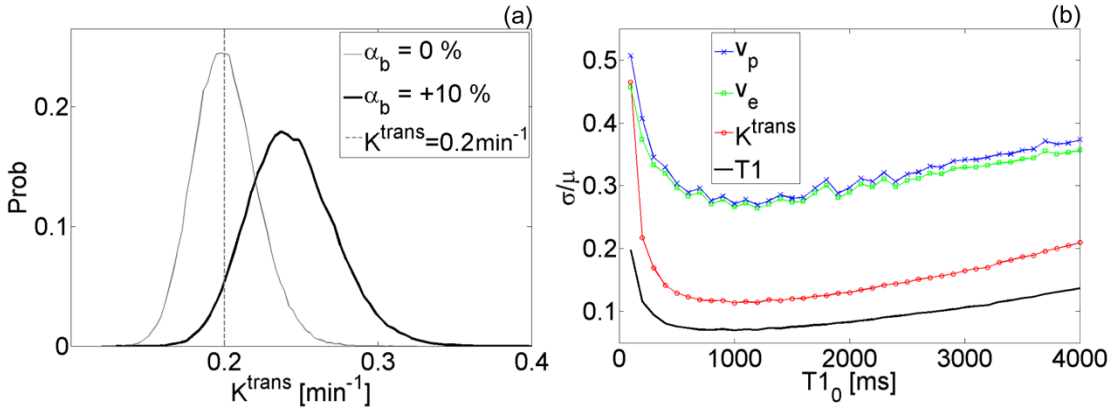

Figure 30: (a) Representative distributions demonstrating the effect of flip angle bias (and consequently T1 bias) on a single pixel with K^{trans} = 0.2 min^{-1}. (b) Coefficient of variation of $T1_0$ and DCE-MRI parameters for the range of $T1_0$ studied in this work.

5.5 Discussion

In quadrature detection, the signal intensity in an artifact-free image with no NMR signal is Rayleigh distributed (Gudbjartsson and Patz 1995). For acquisitions with an n-element array coil and Sum-of-Squares reconstruction the noise power is unchanged while the SNR scales approximately as $\sqrt{n}$. Notice in Figure 25(a) the effect of this reconstruction on the shape of the distribution.

The distribution of the excitation flip angle is a function of the shape of the object being scanned, its electromagnetic properties, the main magnetic field, the RF-pulse

design (hard vs. slice selective or adiabatic), and the polarization of the radiofrequency coil. In a uniform $CuSO_4$ phantom we found that the distribution of the flip angle from a rect pulse resembles a Gaussian distribution with the parameters given in Eqn. 29.

Under these conditions, the variance of the pre-injection longitudinal relaxation time measured with the VFA technique can be predicted for a wide range of $T1_0$ values, as shown in Figure 26. For $\hat{T}1_0 = 2000$ ms, the uncertainty (standard deviation) of the measurement is inversely proportional to the intrinsic SNR of the pulse sequence (Figure 27(a)). While the bias is negligible, at low intrinsic SNR the distribution tends farther from a Gaussian and has a positive skewness. Figure 27(b) demonstrates the effect of flip angle uncertainty on the measurement of $T1_0$. Again, the standard deviation is inversely proportional to α_{SNR} and the bias insignificant. Although the skewness is low, our simulations reveal that even at relatively high α_{SNR} the $T1_0$ distribution is asymmetric. Finally, we find that the bias in $T1_0$ measurements is mainly caused by the bias in the excitation flip angle (Figure 27(c)). The uncertainty depends approximately on the square of the flip angle bias. Surprisingly, a negative bias decreases the standard deviation of the $T1_0$ distribution leading to a more precise measurement of an underestimated relaxation time.

The findings for $\hat{T}1_0 = 2000$ ms apply reasonably well to $T1_0$ values in the range $[100 - 4000]$ ms. Figure 28 uncovers the dependence of the precision and the accuracy

of the VFA measurement technique on the pre-injection relaxation time. Unavoidably, the choice of two flip angles, in our case $\alpha = \{2^o, 10^o\}$, leads to a narrow domain of $T1_0$ values where the uncertainty is minimized.

An understanding of the sources of error in determining the longitudinal relaxation time allows for the prediction of the uncertainty in the estimation of the concentration of the injected contrast agent. The assumption inherent in the fast-exchange limit (Eqn. 22) seems to be satisfied in the range of concentrations encountered in a typical in-vivo study (inset in Figure 26(b)). The temporal evolution of the CA concentration from a single pixel in a highly permeable region is shown in Figure 29(b). The estimated uncertainty superimposed on the solution to Eqn. 23 reveals that Eqn. 28 provides a reasonably accurate prediction for concentration variance. Given the location of the tumor (notice kidney in Figure 29(a)), it is remarkable that signal changes caused by motion artifacts are still within the uncertainty estimated in Eqn. 28: this equation assumes no motion artifacts. Consequently, we can confidently estimate the uncertainty in the pharmacokinetic parameters derived from DCE-MRI measurements using the SPGR pulse sequence. In Figure 30(b) we find that the coefficient of variation of these parameters follows closely that of the pre-injection $T1$; the uncertainty is of the order of, but always higher than, the uncertainty of $T1_0$. This suggests a simple rule of thumb: the SNR of the pre-injection $T1$ map indicates the limiting precision with which the DCE-

MRI parameters can be calculated. Note that the results presented in Figure 30 describe the probability distribution function in a single pixel. In a uniform ROI containing N pixels, the variance will be reduced by a factor of approximately N.

The analysis presented here assumes the statistical variability in signal intensity arises primarily during quadrature detection (i.e. instrumental noise). This approach has the advantage of allowing for the evaluation of the uncertainty and bias of the DCE-MRI parameters as a function of the noise power. The dependence of the noise power on the pulse sequence and hardware platform has been described in detail elsewhere (Macovski 1996).

The term "physiologic variability" is used to describe the error introduced in the modeling phase; uncertainties arising due to discrepancies between the assumptions in the pharmacokinetic model and the underlying physiologic process. We appreciate the critical importance of a patient-specific arterial input function and recognize the additional error introduced when assuming a population-derived AIF. This issue has been previously studied in the preclinical (Loveless, Halliday et al. 2012) and clinical domain (Parker, Roberts et al. 2006). The effect of transmembrane water diffusion has also been examined at length (Landis, Li et al. 2000; Yankeelov, Luci et al. 2008). The accuracy and precision of the DCE-MRI parameters is further affected by the temporal resolution and total scan time (Henderson, Rutt et al. 1998; Hugo, Jaspers et al. 2011).

The results of this work apply to a wide range of pre-injection T1 values, noise power, and flip angle uncertainty. As the inversion problem posed by Eqn. 23 does not have an analytic solution, we believe our findings can be justified by the following heuristic: the calculation of K^{trans} depends on the calculation of the contrast agent concentration, which in turn depends on the longitudinal relaxation time. Hence, the uncertainty of the pre-injection T1 must limit the uncertainty of the contrast agent concentration, which in turn limits the uncertainty of K^{trans}.

5.6 Conclusions

We demonstrate that the limit on the uncertainty of the DCE-MRI parameters is the uncertainty in the measurement of the pre-injection $T1$ map. Current small-animal imaging systems and pulse sequences robust to motion artifacts have the capacity for reproducible quantitative acquisitions with DCE-MRI. The uncertainty in the pharmacokinetic parameters derived from these studies can be readily minimized by decreasing the uncertainty in $T1_0$ measurements. In these circumstances, it is feasible to achieve a level of precision limited only by physiologic variability and to exploit the heterogeneity of tumor K^{trans} as a more sensitive biomarker for therapeutic response.

6. DCE-MRM as a Measure of Blood-Brain Barrier Permeability in a Preclinical Model of Glioma

6.1 Outline

Pediatric high-grade gliomas (pHGGs) occur with strikingly different probabilities in infratentorial and supratentorial regions. Although histologically these malignancies appear similar, they represent distinct diseases. Recent genomic studies have identified histone K27M H3.3/H3.1 mutations in the majority of brainstem gliomas; these mutations are rarely encountered in cortical pHGGs. Clinical work suggests a restricted permeability of the blood-brain-barrier (BBB) in brainstem gliomas. Dynamic contrast-enhanced (DCE) MRM was used to evaluate BBB permeability in a mouse model of pHGG as a function of location (cortex vs. brainstem, $n = 6$ mice/group) and histone mutation (mutant H3.3K27M vs. wild-type H3.3, $n = 6$ mice/group). The pHGG model was generated by expressing PDGF-B, Cre, and mutant H3.3K27M or wild-type H3.3 in the cortex/brainstem of nestin tv-a: $p53^{fl/fl}$ mice at post-natal day 3. *T2*-weighted MRI was used to determine tumor location/extent followed by 4D DCE-MRI for estimating the rate constant (K^{trans}) for tracer exchange across the barrier. BBB permeability was significantly higher in cortical pHGGs; in both brain locations, the permeability was higher in gliomas with wild-type H3.3. Though mice became symptomatic at approximately the same time, the volume of cortical tumors was significantly higher than the volume of brainstem tumors. The difference between the

volumes of gliomas with wild-type and mutant H3.3 was insignificant. Mean K^{trans} was significantly correlated to glioma volume. These results present a possible explanation for the poor response of brainstem pHGGs to therapy. Our findings further illustrate the role played by the microenvironment and epigenetic drivers in shaping tumor growth and BBB permeability.

6.2 Introduction

Pediatric central nervous system (CNS) tumors account for approximately 7% of all primary CNS malignancies diagnosed in the United States (Ostrom, Gittleman et al. 2013). High-grade gliomas (HGGs) represent the most aggressive sub-group with a prevalence rate of 8-12% and a 5-year survival rate of 15-35% (Fangusaro 2012). Children with brainstem HGGs, the majority of which arise in the pons and are referred to as diffuse intrinsic pontine gliomas (DIPG), have a bleaker prognosis with median survival of less than one year from diagnosis (Cohen, Heideman et al. 2011). These tumors are inaccessible to surgical resection and show limited or no response to chemotherapy (Warren 2012); the standard of care is focal radiation, providing only temporary relief. In the past thirty years, clinical trials have failed to identify a single drug that can significantly prolong survival. The location of these tumors poses a particularly difficult challenge for histopathologic examinations and the scarcity of biopsy samples has historically restricted the number of conclusive research findings.

Recent evidence suggests that the mechanism of high-grade gliomagenesis in children is region-specific (Sturm, Witt et al. 2012). Brainstem and midline pHGGs have a high occurrence of specific and mutually exclusive K27M mutations in the histone H3 family (H3F3A and HIST1H3B) and less frequently in genes involved in chromatin remodeling (ATRX-DAXX). In contrast, cortical HGGs rarely harbor K27M histone mutations and instead can harbor G34R/V mutations in H3F3A which frequently co-occur with mutations in ATRX-DAXX (Schwartzentruber, Korshunov et al. 2012; Wu 2012). Pediatric cortical and brainstem HGGs also harbor distinct differences in the DNA copy-number, DNA methylation, and gene-expression profiles when compared to the adult analogues (Schiffman, Hodgson et al. 2010; Paugh, Broniscer et al. 2011; Puget, Philippe et al. 2012; Sturm, Witt et al. 2012).

Although the role of the newly discovered histone mutations in gliomagenesis is still under intense investigation, recent studies suggest that H3F3A K27M mutations are associated with worse prognosis and decreased survival (Khuong-Quang, Buczkowicz et al. 2012). These histone mutants have been shown to globally decrease trimethylation of Lys27 on all H3, working as an inhibitor of EZH2, leading to global epigenetic and transcriptomal changes (Schwartzentruber, Korshunov et al. 2012; Lewis, Müller et al. 2013).

Pediatric brainstem HGGs are diagnosed based on MRI findings and a combination of neurological symptoms (Epstein and Farmer 1993). Given the critical importance of in vivo imaging in the diagnosis of HGGs, several research groups have investigated the feasibility of using different MR pulse sequences as a potential prognostic marker for disease progression (Sugahara, Korogi et al. 1998; Law, Yang et al. 2003; Warren 2004; Hipp, Steffen-Smith et al. 2011). As pediatric brainstem HGGs show limited enhancement in contrast-enhanced *T1*-weighted MRI, and due to the high-frequency of H3.3K27M mutations in this disease group, we hypothesized that both tumor location and H3.3K27M status may influence BBB permeability. In this study we used dynamic contrast-enhanced (DCE) MRI to evaluate the permeability of the blood-brain barrier of a genetically engineered mouse model of pHGG as a function of location (supratentorial vs. brainstem) and H3.3K27M mutation status (mutant vs. wild-type).

6.3 Materials and Methods

6.3.1 RCAS/TVA model of pediatric high-grade glioma

All animal studies were approved by the Duke University Institutional Animal Care and Use Committee. The RCAS/TVA system was used to generate a pHGG mouse model expressing either the mutated (H3.3K27M) or wild-type (H3.3WT) histone H3.3 (Becher, Hambardzumyan et al. 2010). Post-embryonic day 3 neonates were injected

with 1 μL ($1x10^5$ cells/μL) of virus expressing DF1 cells divided equally into thirds in the following combinations:

1) RCAS-PDGF-B + RCAS-Cre + RCAS-H3.3WT (wild-type histone)

2) RCAS-PDGF-B + RCAS-Cre + RCAS-H3.3K27M (mutant histone).

Neonates were anesthetized on ice and cells were injected in the cortex ($n = 12$) or brainstem ($n = 12$) as described in Barton et al (Barton, Misuraca et al. 2013). Each group was further subdivided in wild-type ($n = 6$) or mutant ($n = 6$) histone sub-groups amounting to four final distinct phenotypes. Mice were monitored closely for signs of tumor development (lethargy, head tilt, increased head size). On the appearance of glioma symptoms, mice underwent *T2*-weighted and DCE-MRI. Following the MR study, the animals were euthanized by isoflurane overdose, brains were excised, formalin fixed for 24 hrs, and embedded in paraffin for histological analysis.

6.3.2 T2-weighted and dynamic contrast-enhanced MRI

MRI experiments were performed on a $7T$ small-animal, MRI scanner (Bruker BioSpin MRI GmbH, Ettlingen, Germany). An actively detuned volume excite RF-coil was used in conjunction with a four-element array coil for surface receive.

The location and extent of the tumor were determined in a *T2*-weighted image acquired with a spin-echo 3D-RARE pulse sequence. The imaging parameters were:

$TR/TE_{eff} = 6300/40$ ms, RARE factor = 8, $BW = 50$ kHz, 150 μm isotropic voxels, total acquisition time ≈ 28 mins.

The DCE-MRI study protocol has been described in detail elsewhere (Subashi, Moding et al. 2013). Briefly, an interleaved 3D-UTE radial sampling pulse sequence was reconstructed using a sliding-window keyhole approach allowing for the acquisition of 4D datasets. The imaging parameters were: FOV=20x20x20 mm^3, $matrix = 128x128x128$, TR/TE=5/0.02 ms, $NEX = 1$, BW=100 kHz, $\alpha = 10^o$, and 10 sec temporal resolution. The pre-injection longitudinal relaxation time was measured with the variable flip-angle acquisition (Fram, Herfkens et al. 1987) using the same radial sampling strategy and identical imaging parameters except $\alpha = \{2^o, 10^o\}$.
Animals were maintained under anesthesia by isoflurane delivery via a nose cone in a custom-made animal positioning system. Body temperature was controlled between 36 °C and 37 °C by circulating warm water. Dynamic imaging was initiated two minutes prior to contrast agent injection and lasted for approximately 20 min post-injection. An automatic syringe pump (KD Scientific Inc., Holliston, MA) was used to administer Gd-DTPA (Magnevist, Schering AG, Berlin, Germany) as a bolus via a 27-gauge tail vein catheter at a dose of 0.5 mmol/kg and flow rate of 2.4 mL/min as described by Loveless *et. al* (Loveless, Halliday et al. 2012).

6.3.3 Image analysis

The time-dependent contrast agent concentration $C(t)$ was calculated using:

$$C(t) = \frac{1}{r_1}(R1 - R1_0) \qquad \textbf{Eqn. 32}$$

where $R1_0$ is the native relaxation rate and r_1 is the longitudinal relaxivity of Gd-DTPA. The post-injection relaxation rate is found by (Li, Zhu et al. 2000; Heilmann, Kiessling et al. 2006):

$$R1(t) = -\frac{1}{TR}\ln\left(\frac{1-(A+B)}{1-\cos(\alpha)\,(A+B)}\right) \qquad \textbf{Eqn. 33}$$

$$A = \frac{S(t) - S(0)}{S_0 \sin(\alpha)}, \qquad B = \frac{1 - E1_0}{1 - \cos(\alpha) E1_0}$$

where $E1_0 = exp(-TR*R1_0)$, $S(0)$=signal intensity before contrast injection, and $S(t)$=time-dependent signal intensity.

In the framework of the extended Tofts model (Tofts 1997), the time-dependent contrast agent concentration in the tissue compartment is described by:

$$C(t) = v_p \cdot C_p(t) + K^{trans} \int_0^t C_p(u) \cdot e^{-(K^{trans}/v_e)\cdot(t-u)} du \qquad \textbf{Eqn. 34}$$

where $C_p(t)$ is the arterial input function (AIF), v_p is the fractional volume of the plasma compartment, v_e is the fractional volume of the extravascular-extracellular space (EES), and K^{trans} (permeability parameter) is the rate constant for the transfer of the contrast agent from plasma to EES measured in ml/s of contrast agent per ml of tissue. This

equation can be represented in matrix form and solved on a pixel-by-pixels basis using the linear least-squares method (Murase 2004). In the analysis of our dynamic data, the population AIF reported by Loveless et al. (Loveless, Halliday et al. 2012) was used when solving Eqn. 34.

The tumor volume was manually segmented in the *T2*-weighted image and the mask was imported into the functional parameter maps obtained from DCE-MRI. The K^{trans} values from each animal were pooled into the respective phenotype group and the pixel-wise distributions were compared using the Kruskal-Wallis test. K^{trans} values outside the range [0 1] min^{-1} were omitted from the analysis. The statistical test was repeated using ANOVA after the distributions were transformed using the square-root operator.

6.4 Results

All tumors included in this work were histologically confirmed to be high-grade gliomas defined by the presence of microvascular proliferation and/or necrosis. Pseudopalisading necrosis and vascular proliferation can be seen in a representative H&E section in Figure 31. The MR image features of the murine tumors reflect the clinical analogues observed in children (Warren 2012): gliomas appear hyperintense on *T2*-weighted images and hypo/iso-intense on *T1*-weighted images as shown in Figure

32. The pre-injection *T1* values in the tumor volume typically were (μ±σ) 1.54±0.21 sec. Figure 32(b) depicts the functional K^{trans} map at the same axial location as the slice in

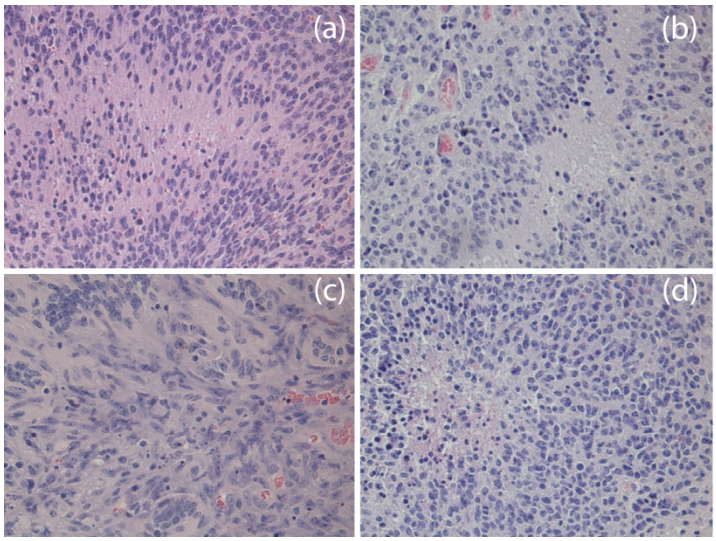

Figure 31: High-grade brainstem and cortex glioma induced with identical genetic drivers: (a) cortical HGG with H3.3WT, (b) cortical HGG with H3.3K27M, (c) brainstem HGG with H3.3WT, and (d) brainstem HGG with H3.3K27M. Tumors appear histologically similar in H&E.

Figure 32(a). Graphs of the temporal evolution of the concentration of the contrast agent at two pixels (arrowheads in Figure 32(b)) with distinct permeability parameters are given in Figure 32(d). Figure 33 demonstrates the heterogeneity of BBB permeability in a typical cortical glioma.

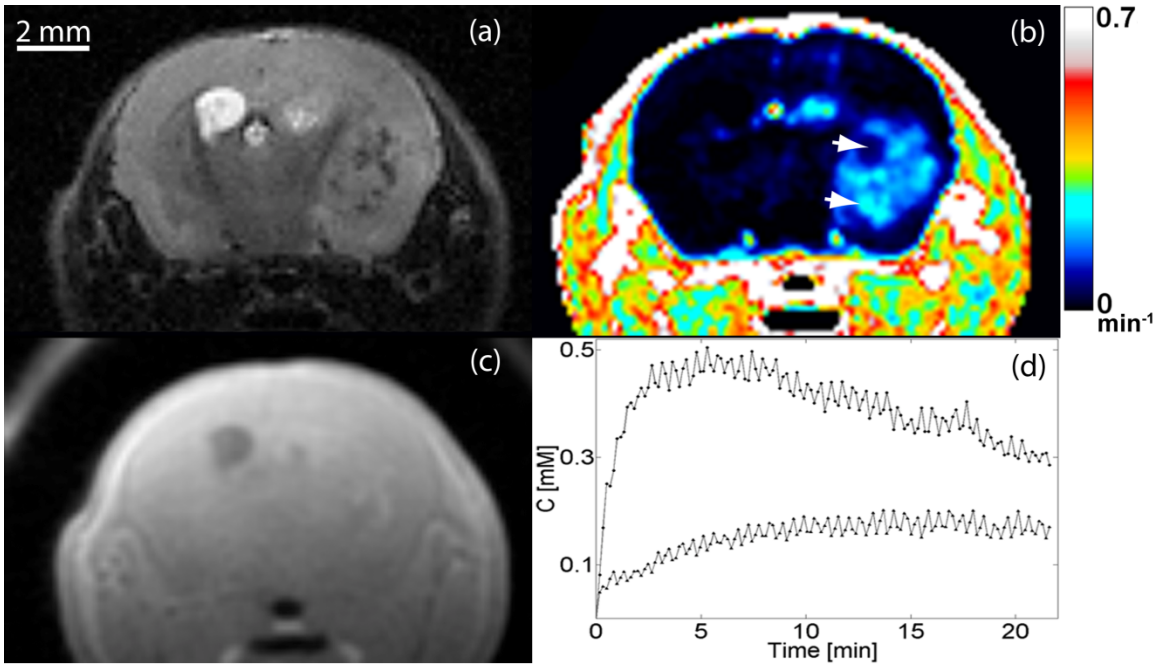

Figure 32: Representative MR images of cortical glioma. Tumors appear hyperintense on (a) *T2*-weighted and (c) hypo/iso-intense on *T1*-weighted MRI. (b) K^{trans} map at same axial location. (d) Concentration of the contrast agent as a function of time at two pixels (arrowheads in panel (b)) with distinct permeability parameters.

The K^{trans} maps from a representative animal in each phenotype group are compared in Figure 34. The outline of the tumor volume determined from the corresponding *T2*-weighted image is overlaid for reference. Figure 34(a, b) shows a high-grade glioma with the H3.3WT or H3.3K27M histone mutation originating in the cortex; Figure 34(c, d) presents the respective brainstem glioma. Notice the inhomogeneous spatial distribution and distinctly higher K^{trans} values in the cortical tumors. This heterogeneity is characterized in Figure 34(e, f) depicting the permeability parameter

histogram of the separate phenotypes. The distributions are computed by pooling the K^{trans} histograms from all animals in each specific group.

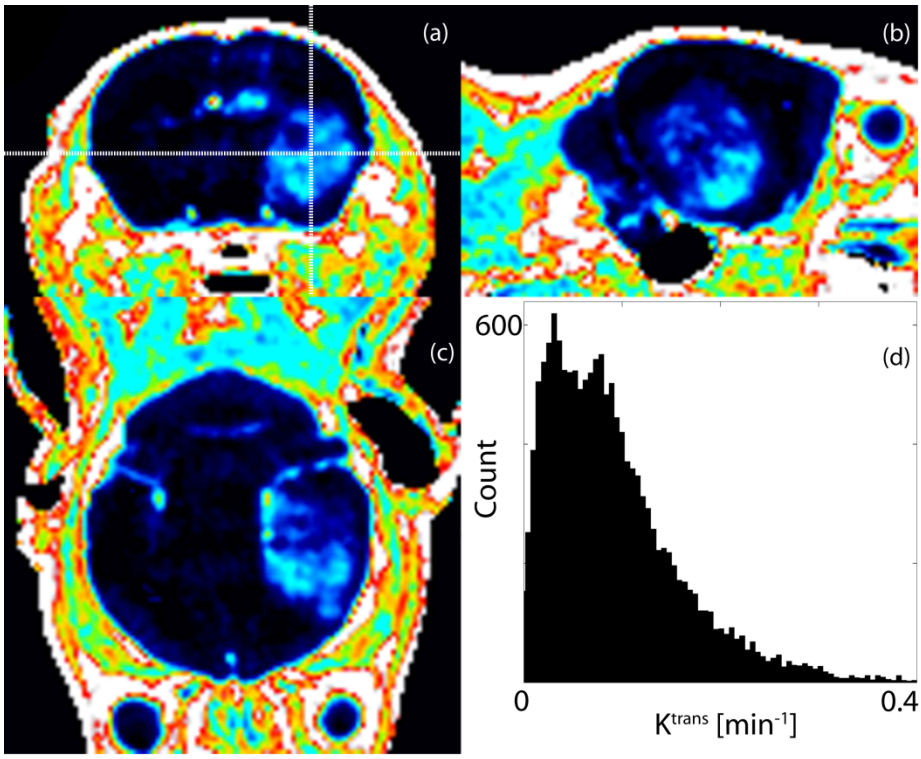

Figure 33: Orthogonal views of K^{trans} map demonstrate an inhomogeneous spatial distribution of the permeability parameter in (a) axial, (b) sagittal, and (c) coronal planes. (d) K^{trans} histogram over tumor volume.

In cortical HGGs the mean BBB permeability was significantly higher than in brainstem HGGs ($p<0.01$); for both locations, the mean BBB permeability was significantly higher in gliomas with the wild-type H3.3 histone ($p<0.01$). The analysis of variance on the square-root transformed distributions confirmed these findings. The difference in mean

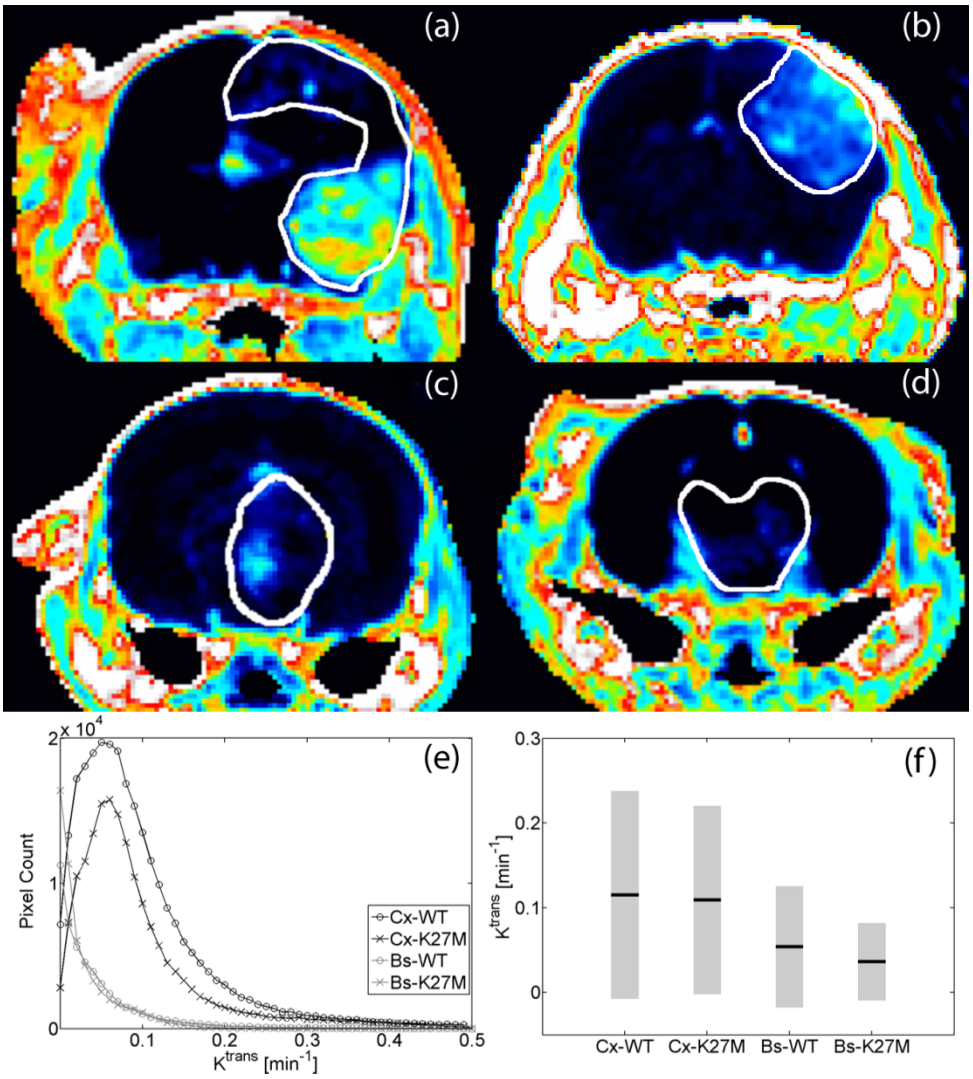

Figure 34: Representative K^{trans} maps from each phenotype group: (a) cortical HGG with H3.3WT, (b) cortical HGG with H3.3K27M, (c) brainstem HGG with H3.3WT, and (d) brainstem HGG with H3.3K27M. Notice the inhomogeneous spatial distribution and distinctly higher K^{trans} values in cortical tumors. (e) Histogram of K^{trans} computed by pooling the parameters from animals in each phenotypical group. (f) In cortical (Cx) HGGs the mean BBB permeability was significantly higher than in brainstem (Bs) HGGs ($p<0.01$); for both locations, the mean BBB permeability was significantly higher ($p<0.01$) in gliomas with wild-type H3.3 histone.

permeability was higher (an average of 150% higher) when comparing brain location than when considering H3.3K27M mutation status (an average of 16% higher). Figure 35(a) plots the time in days since DF1-virus injection until the appearance of glioma symptoms (lethargy, head tilt, increased head size); the number of days for mice to become symptomatic was not significantly different between the four groups (ANOVA, $p \approx 0.82$). Although on average it took the same number of days for mice to become symptomatic, the volume of the cortical tumors was significantly higher (ANOVA, $p < 0.01$) than the volume of the brainstem tumors. In each location (cortex or brainstem) the difference between the volumes of the gliomas with wild-type or mutated H3.3 histone was not statistically significant (ANOVA, $p \approx 0.51$). The observations summarized in Figure 35(b) imply that the growth rate for tumors in the cortex is significantly higher than for those developing in the brainstem, regardless of H3.3K27M mutation status. Interestingly, we find a weak, but significant correlation ($p < 0.05$, $\varrho = 0.43$) between HGG volume and mean of K^{trans} as shown in Figure 35(c). This finding is suggestive of an invasion mechanism associated with tumor perfusion/permeability.

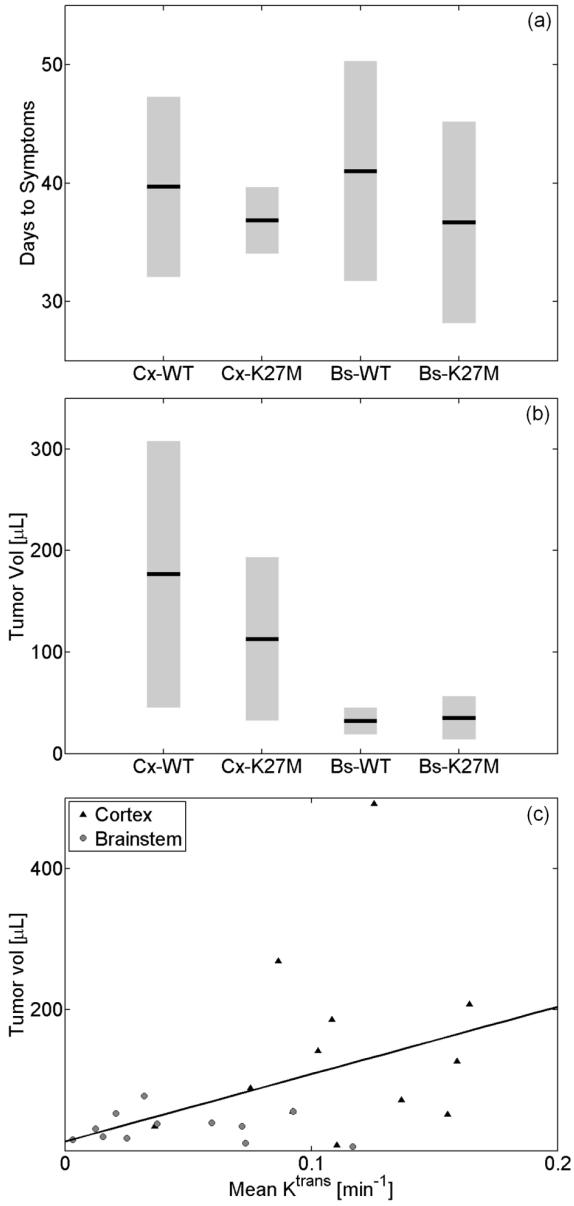

Figure 35: (a) Time in days (μ±σ) since DF1-virus injection until appearance of glioma symptoms. (b) The volume of the cortical (Cx) tumors was significantly higher ($p<0.01$). In each location the difference between the volumes of the gliomas with wild-type (WT) or mutated (K27M) H3.3 histone was not significant. (c) Tumor volume as a function of the mean of the permeability parameter. Mean K^{trans} was significantly correlated ($p<0.05$, $\varrho=0.43$) to glioma volume.

6.5 Discussion

Preclinical models are essential in the study of carcinogenesis in a biologically relevant microenvironment (Becher and Holland 2006). The advent of genetically engineered mouse models of high-grade gliomas (Becher, Hambardzumyan et al. 2010) has provided a unique opportunity for understanding the driving oncogenic events. The aim of this work was to determine in vivo the permeability of the blood-brain barrier in four distinct subgroups of pediatric high-grade gliomas: HGGs with wild-type vs. mutant histone H3.3 (H3.3K27M) developing in the brainstem vs. the cortex. K27M mutations are highly prevalent in pediatric HGG leading to inhibition of the PRC2 complex and a decrease in global H3 trimethylation (Lewis, Müller et al. 2013). Although these histone mutations occur more commonly in midline tumors they have also been identified in the cortex (Zhang, Wu et al. 2013). Presence of H3K27M has been linked to poor prognosis, and interestingly in this study, showed significant decrease in BBB permeability. These findings show DCE-MRI may be a useful tool in distinguishing the clinical characteristics of mutation status in vivo. Our study also provides further insight into K27M tumor biology, although further work is needed to understand the mechanism by which H3.3K27M leads to a decreased BBB permeability.

It is the current standard of care to diagnose and monitor tumor progression in pediatric patients with HGG using conventional anatomic MR imaging. Using the

clinically available MR sequences to date, the parameters of tumor size and invasiveness, metastatic lesions, necrosis, hydrocephalus, or edema have not been able to accurately predict overall survival in these patients (Hargrave, Chuang et al. 2008). However, the addition of spectroscopy, perfusion, and diffusion MRI has recently been used to identify prognostically distinct subgroups (Lober, Cho et al. 2014) and to correlate to survival time (McConville, Hambardzumyan et al. 2007; Hipp, Steffen-Smith et al. 2011).

SPECT imaging with Tc-99m Sestamibi was performed in half of the murine gliomas listed above. In this pilot study, a commercially available scanner fitted with a 0.35mm multi-pinhole collimator was used to compare the permeability parameters measured with DCE-MRI and SPECT. The field of view covered the entire brain and was reconstructed at 125μm isotropic voxels using the pixel-based ordered-subsets expectation-maximization algorithm (Woutjan, Brendan et al. 2010). Tc-99m Sestamibi was injected as a bolus via a tail-vein catheter at doses varying from 2 to 20 mCi and images were acquired for 60 minutes. As shown in Figure 36, this pilot study found an insignificant enhancement in SPECT acquisitions. This suggests that the mechanism by which Tc-99m Sestamibi binds to tumor cells is absent in the mouse model of HGGs studied in this project.

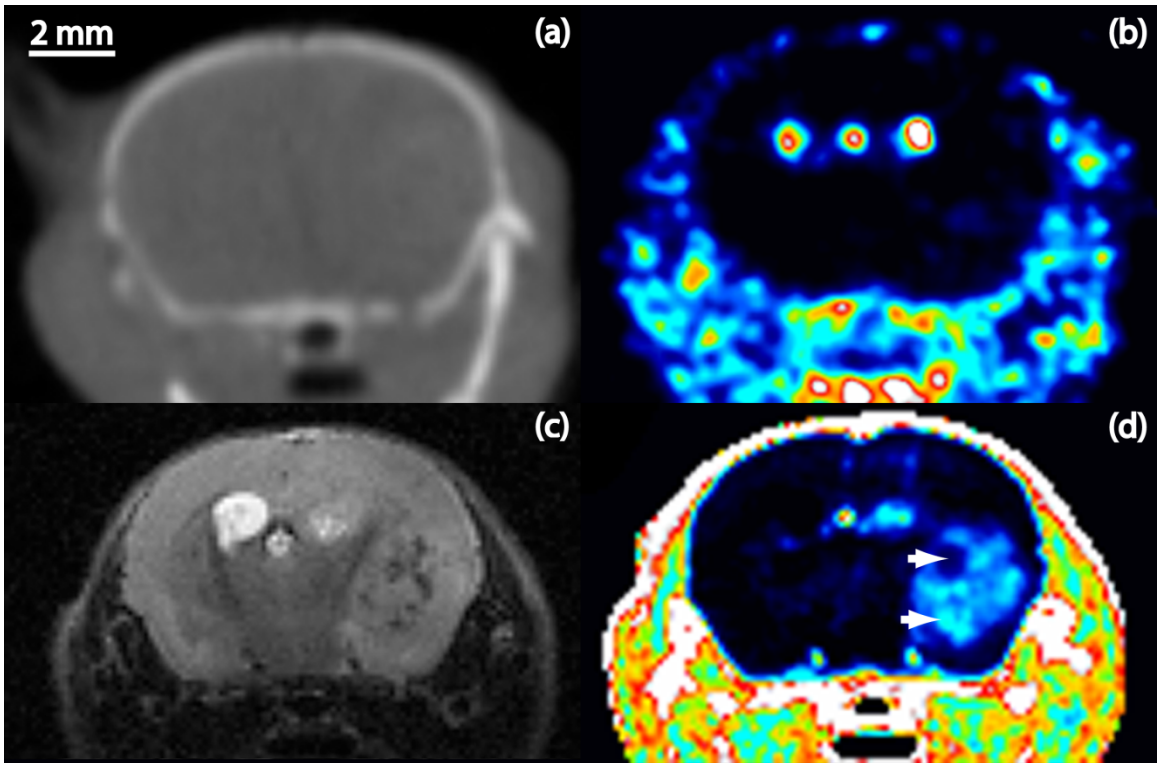

Figure 36: Representative acquisition comparing (a) CT, (b) SPECT, (c) T2-weighted MRI, (d) K^{trans} images of murine model of cortical glioma. This pilot study found an insignificant enhancement in SPECT acquisitions of gliomas imaged with Tc-99m Sestamibi.

In this work we observe that the permeability of the blood-brain barrier, measured with high resolution DCE-MRI, is dependent on the location of the tumor and its genotype. Our study demonstrates that cortical HGG blood vessels have a significantly higher permeability (~ 150% higher) than those developing in the brainstem. In both brain locations (cortex vs. brainstem) there is a small, but significantly higher (~16% higher) permeability in gliomas with histone H3.3WT than in those with H3.3K27M. Interestingly, tumor location appears to play a role in tumor growth rate as

cortical HGGs had a significantly larger volume than the brainstem HGGs, but symptoms for both conditions appeared at approximately the same time. H3.3K27M mutation status did not lead to a significantly different tumor volume in both brain regions. Mean K^{trans} was a significant predictor for the volume of gliomas studied in this work.

These results suggest that a reduction in the alteration of the BBB in brainstem HGGs compared to cortical HGGs is a possible explanation for the lack of response of brainstem HGGs to drug therapy. Given that our experiments controlled for variability in epigenetic drivers, our findings further illustrate the important role played by the glioma microenvironment in influencing tumor growth and BBB permeability. In summary, DCE-MRI imaging of a genetically engineered mouse model of pediatric HGGs demonstrates that both tumor location and an epigenetic driver (H3.3K27M) determine BBB permeability. Future studies will address whether the extent of the permeability of the BBB influences response to treatment, particularly to therapies (such as bevacizumab) that impact BBB directly.

6.6 Conclusions

In this work we demonstrate a differential opening of the blood-brain barrier dependent on HGG location and a newly described epigenetic driver (H3.3K27M). Although the genetic drivers in our tumor model are identical, the response of the microenvironment

to cell proliferation is not the same. Therefore, the local microenvironment in which the tumor cells interact with normal brain may have implications in regards to degree of invasion and ultimately, patient survival. DCE-MRM can measure these effects in vivo, non-destructively and without the use of ionizing radiation, allowing for repeated measurements.

7. DCE-MRM Identifies Regions of Therapeutic Response in a Preclinical Model of Colorectal Adenocarcinoma

7.1 Outline

Dynamic contrast-enhanced (DCE) MRI studies, when measuring the effect of an anti-angiogenic treatment, often compare the derived biomarkers on manually selected tumor regions or over the entire volume. These measurements include domains where the interpretation of the biomarkers may be unclear (such as in necrotic areas). The incorporation of semi-quantitative kinetic parameters to analyze DCE-MRI data, combined with a volumetric high spatiotemporal resolution acquisition, may provide insights into the response of the tumor microenvironment to therapy.

Two cohorts (n=8/group) of *nu/nu* mice with LS-174T implanted in the mammary fat pad were imaged at five time points over the course of four weeks. The treatment/control group received bevacizumab/saline at a dose of 5 mg/kg or 5 ml/kg twice weekly; imaging experiments were performed weekly. MRI images, covering the entire tumor volume, were acquired at an isotropic resolution of 156x156x156 μm^3 and with a temporal sampling rate of 9.9 sec. At completion of study, mice were perfusion-fixed for histology (CD31 and HE staining). The time-to-peak (TTP) was calculated on smoothed signal intensity vs. time curves. The histogram of TTP was used to identify two (fast- and slow-enhancing) regions based on a threshold of TTP=1000 sec. The

regions were correlated to K^{trans} maps, CD31 and HE slides, and the effect of therapy was locally examined.

Bevacizumab has a significant effect on tumor doubling time and leads to a mean tumor growth delay of approximately 8.4 days. The regions defined by thresholding the TTP parameter identify two distinct domains correlating significantly with tumor permeability and microvessel density. In the whole tumor volume and the fast-enhancing region, the mean K^{trans} was significantly lower in the treatment group at day 9; in the slow-enhancing region, K^{trans} was not significantly different between the control and treatment cohort at any point during therapy. At day 9, the relative volume of the fast-enhancing region was significantly lower in the treatment group, while that of the slow-enhancing region was significantly higher.

The histogram of the time-to-peak provides useful knowledge about the spatial distribution of K^{trans} and microvascular density. Two regions with distinct kinetic parameters were identified when the TTP map from DCE-MRM was thresholded at 1000 sec. The effect of bevacizumab, as measured by a decrease in K^{trans}, was confined to one of these regions. DCE-MRM studies may contribute unique insights into the response of the tumor microenvironment to therapy.

7.2 Introduction

Tumor neovasculature, often identified by leakiness, heterogeneous blood flow, and abnormal vessel diameter, is structurally and functionally different from healthy vessels. Dynamic contrast-enhanced (DCE) MRI has been widely used to study transfer kinetics between the intra- and the extra-vascular space, providing a set of in-vivo biomarkers useful in diagnosis and assessment of response to therapy (O'Connor, Jackson et al. 2012). The majority of studies measuring the effect of an anti-angiogenic agent have compared the mean value of these biomarkers on manually selected regions of interest (ROIs) or over the entire tumor volume. These measurements include regions in the tumor where the interpretation of the kinetic parameters is unclear (such as in necrotic areas) or where the magnitude of response to therapy may be heterogeneous (Sourbron and Buckley 2011). High spatiotemporal acquisitions, which we will refer to as dynamic contrast-enhanced magnetic resonance microscopy (DCE-MRM), can reveal significant differences in kinetic parameters even at distances less than 500 μm (Subashi, Moding et al. 2013). The incorporation of semi-quantitative kinetic parameters in the analysis of DCE-MRM data may provide a way for identifying tumor subpopulations responding differently to therapy. In this work, we present findings from a longitudinal study in which the histogram of the time-to-peak (TTP) parameter was used to

automatically segment the tumor volume with the aim of examining the spatial distribution of therapeutic effect.

7.3 Materials and Methods

7.3.1 DCE-MRM protocol

Measurements were acquired in a 7 T small animal MRI scanner (Bruker BioSpin MRI GmbH, Ettlingen, Germany) equipped with self-shielded gradient coils having a maximum strength of 450 mT/m and rise time of 110 μsec. An actively detuned volume RF-coil (linear transmit, ID=72 mm) was used in conjunction with a four-element coil ($2x2$ linear array, 10x10 mm loops) for surface receive.

The time-dependent contrast agent concentration $C(t)$ was calculated using:

$$C(t) = \frac{1}{r_1}(R1 - R1_0) \qquad \textbf{Eqn. 35}$$

where $R1_0$ is the native relaxation rate and r_1 is the longitudinal relaxivity of the injected agent. The post-injection relaxation rate is found by (Li, Zhu et al. 2000; Heilmann, Kiessling et al. 2006):

$$R1(t) = -\frac{1}{TR}\ln\left(\frac{1-(A+B)}{1-\cos(\alpha)\,(A+B)}\right) \qquad \textbf{Eqn. 36}$$

$$A = \frac{S(t)-S(0)}{S_0 \sin(\alpha)}, \qquad B = \frac{1-E1_0}{1-\cos(\alpha)E1_0}$$

where $E1_0 = \exp(-TR * R1_0)$, $S(0)$ = pre-injection signal intensity, and $S(t)$ = time-dependent (post-injection) signal intensity.

In the framework of the extended Tofts model (Tofts 1997), the temporal evolution of the contrast agent concentration in the tumor is described by:

$$C(t) = v_p \cdot C_p(t) + K^{trans} \int_0^t C_p(u) \cdot e^{-(K^{trans}/v_e)\cdot(t-u)} du \qquad \textbf{Eqn. 37}$$

where $C_p(t)$ is the arterial input function (AIF), v_p is the fractional volume of the plasma compartment, v_e is the fractional volume of the extravascular-extracellular space (EES), and K^{trans} is the rate constant (measured in ml/min per ml of tissue) for the exchange of the agent across the microvascular endothelium. Eqn. 37 was solved on a pixel-by-pixel basis using the linear least-squares method (Murase 2004) and the population AIF reported by Loveless et al. (Loveless, Halliday et al. 2012).

The pulse sequence and the k-space sampling strategy used in this study have been described elsewhere (Subashi, Moding et al. 2013). Briefly, an interleaved ultra-short-echo radial sampling sequence allowed for the reconstruction of 4D datasets using a sliding-window keyhole approach. The acquisition parameters were: FOV = 20 mm^3, matrix = 128^3, TR/TE = 5/0.02 ms, NEX = 1, $\alpha = 10^o$, and 9.9 sec temporal resolution. The native relaxation rate was measured with the variable flip-angle technique (Fram, Herfkens et al. 1987) using the same acquisition parameters and $\alpha = \{2^o, 10^o\}$.

Animals were positioned in a custom-made MR-cradle, maintained under anesthesia by isoflurane delivery via a nose cone, while body temperature was controlled between 36 °C and 37 °C by circulating warm water. Breathing was monitored through a pneumatic pillow while adjusting isoflurane delivery to maintain a rate of 50-60 breaths/min. Dynamic imaging initiated two minutes prior to contrast agent injection and lasted for approximately 20 min post-injection. An automatic syringe pump (KD Scientific Inc., Holliston, MA) was used to administer Gd-DTPA (Magnevist, Schering AG, Berlin, Germany) as a bolus via a 27 − gauge tail vein catheter at a dose of 0.5 mmol/kg and flow rate of 2.4 mL/min.

7.3.2 Image Analysis

We hypothesized that the analysis of the K^{trans} map based on the TTP map would enable the identification of tumor regions responding to anti-angiogenic therapy. It is already known that TTP is inversely correlated to microvessel density (Yabuuchi, Fukuya et al. 2003). To calculate the TTP parameter, the signal intensity curves were smoothed with an optimized filter designed for the identification of signal amplitude (Gans and Gill 1983). Given a model for the noise power of the acquisition (Subashi, Choudhury et al. 2014), we find that optimal smoothing is achieved with a single pass of a second order Savitzky-Golay filter with a window size of 15 points. Voxels where the peak enhancement was less than 10% of tumor peak enhancement were checked

visually and assigned the maximum TTP if signal outliers biased the smoothing operation. This is justified because it was found that in these voxels the signal intensity was close to the noise floor. Once the maximum was estimated, the time to reach the peak of the signal was calculated on a pixel-by-pixel basis. The TTP map was used to define two regions:

- Region 1 (fast enhancing): 0 sec $\leq TTP \leq$ 1000 sec
- Region 2 (slow enhancing): 1000 sec $< TTP \leq TTP_{max}$

The tumor volume was manually segmented and the mask imported into the kinetic parameter maps obtained from DCE-MRM. The TTP parameter was used to generate two additional masks identifying the regions described above.

7.3.3 Treatment protocol

All animal studies were approved by the Duke University Institutional Animal Care and Use Committee. Female *nu*/*nu* mice with a colorectal adenocarcinoma cell line (LS-174T, Charles River Laboratories, Wilmington, MA), implanted in the mammary fat pad, were followed longitudinally for four weeks. The study design is described diagrammatically in Figure 37. The animals were randomly assigned to a treatment ($n = 8$) or a control ($n = 8$) group and a baseline scan was acquired at day 0. At day 1,

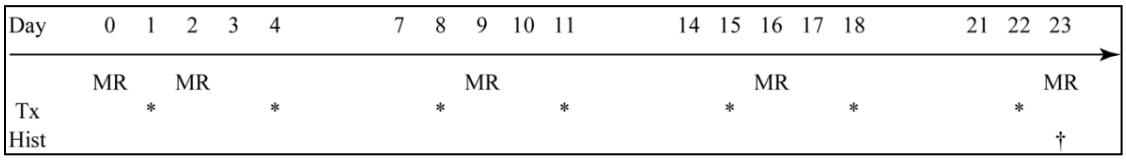

Figure 37: Two cohorts (n=8/group) of *nu/nu* mice with LS-174T implanted in the mammary fat pad were imaged at five time points over the course of four weeks. A baseline scan was acquired at day 0. Treatment (Tx) was first administered at day 1 at a dose of 5 mg/kg (n=8); the control group (n=8) received normal saline at a dose of 5 ml/kg. The first post-treatment imaging experiment was performed at day 2. Thereafter, treatment/placebo was administered at same respective dose twice weekly; imaging experiments were performed weekly. At completion of study, mice were perfusion-fixed for histology (CD31 and HE staining).

bevacizumab (Avastin®, Genentech, San Francisco, CA) was administered via an intraperitoneal injection at a dose of 5 mg/kg; the control group received normal saline (0.9% sodium chloride) at a dose of 5 ml/kg. The first post-treatment imaging experiment was performed at day 2. Thereafter, bevacizumab/placebo was administered at the same respective dose twice weekly; imaging experiments were performed weekly.

At completion of study, the mice were transcardially perfused to allow for a systematic comparison of histologic stains with DCE-MRM parameters. While anesthetized with Nembutal (Oak Pharmaceutical, Lake Forest, IL), saline was delivered transcardially for ~5 min at a flow rate of 8 mL/min followed by 10% buffered formalin for approximately the same time. The fixed specimens were immersed in a 10% formalin solution for 1 day. Given the location of the tumors in this study, whole-body perfusion/fixation was necessary in matching histology slides to MR imaging planes

using anatomical landmarks. Four to six histology slides with a thickness of 5 μm were stained with CD31 or H&E in an alternating sequence. The brown channel intensity from a micrograph of the CD31 slide was used as a surrogate marker for micro-vessel density (Weidner 1995).

7.3.4 Statistical Analysis

Mixed effect modeling was used to calculate tumor growth delay, tumor doubling time (DT), and to assess treatment effect on volume (Demidenko 2010). The mean value of K^{trans} in the tumor volume, region 1, and region 2, was compared with a two-sample $t-$ test. This test was also used to compare the relative volume of the regions defined from the TTP map. K^{trans} values outside the range [0 1] min^{-1} were omitted from the analysis. Significance was determined based on a $P-$ level less than 0.05.

7.4 Results

7.4.1 Biomarker Correlation

Figure 38(a) shows a representative K^{trans} map overlayed on the contrast-enhanced $T1-$ weighted MR image. In Figure 38(b) the K^{trans} map is compared to the TTP map of the same slice demonstrating in red the spatial distribution of region 1 and in blue that of region 2. The temporal evolution of the contrast agent concentration in a single pixel at the core and rim of tumor are shown in Figure 38(c). The fit lines reveal

the effect of smoothing with the optimized Savitzky-Golay filter. The histogram of TTP in the entire tumor volume is depicted in Figure 38(d) with the dashed line representing the threshold used to separate region 1 and region 2.

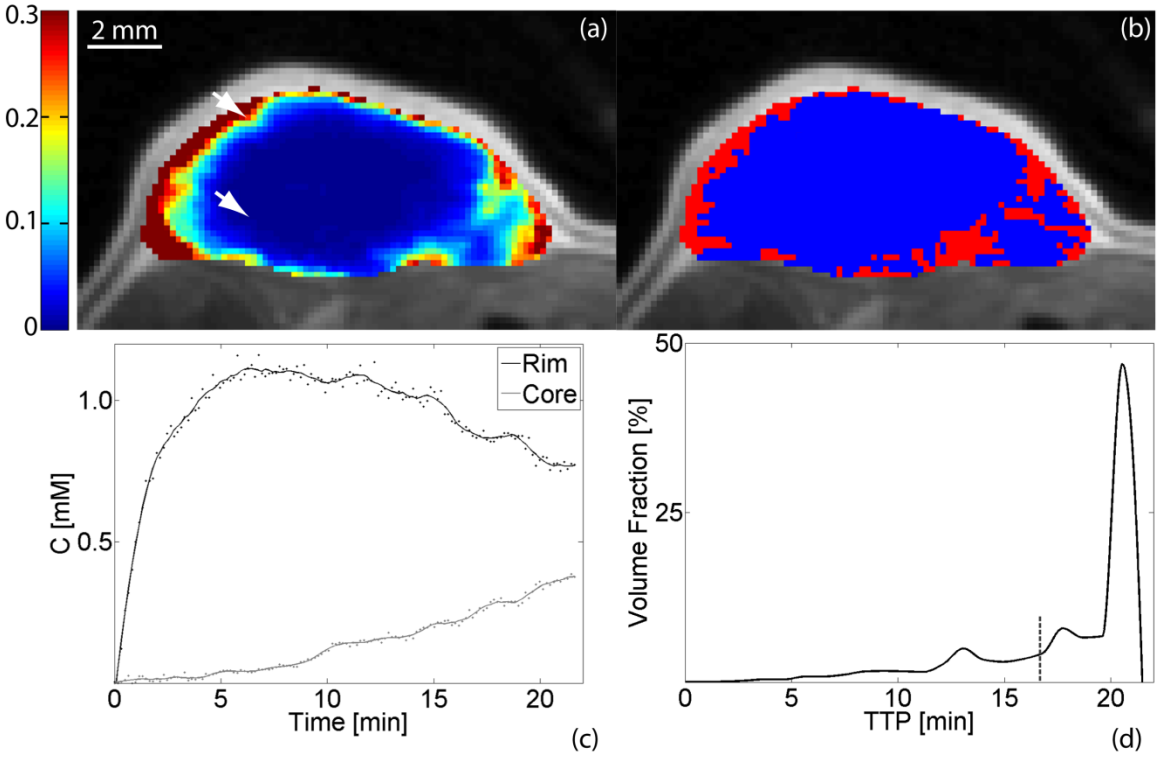

Figure 38: (a) K^{trans} map overlayed on contrast-enhanced MR image (colormap is in units of min^{-1}). (b) TTP map of same slice demonstrating in red the spatial distribution of region 1 (0 sec≤TTP≤1000 sec) and in blue region 2 (1000 sec< TTP≤ TTP_{max}). (c) Temporal evolution of contrast agent concentration in a single pixel at core and rim of tumor (arrows in panel (a)). The lines show the smoothed curve calculated with the optimized Savitzky-Golay filter. (d) Histogram of TTP in tumor volume. Dashed line shows the threshold used to separate region 1 and region 2.

Figure 39 demonstrates the correlation between K^{trans}, TTP regions, CD31, and H&E staining in the same animal (representative mouse from treatment group). A significant correlation was found between K^{trans} and the intensity of the brown channel in a micrograph of a histology slide stained with CD31. The blue and red datapoints are from measurements in manually drawn ROIs in the core and rim of the tumor respectively. A comparison between region 1 and region 2 for all animals in this study shows that K^{trans} is significantly higher in the fast-enhancing regions. The TTP parameter may be used to select for regions with both high permeability and microvascular density.

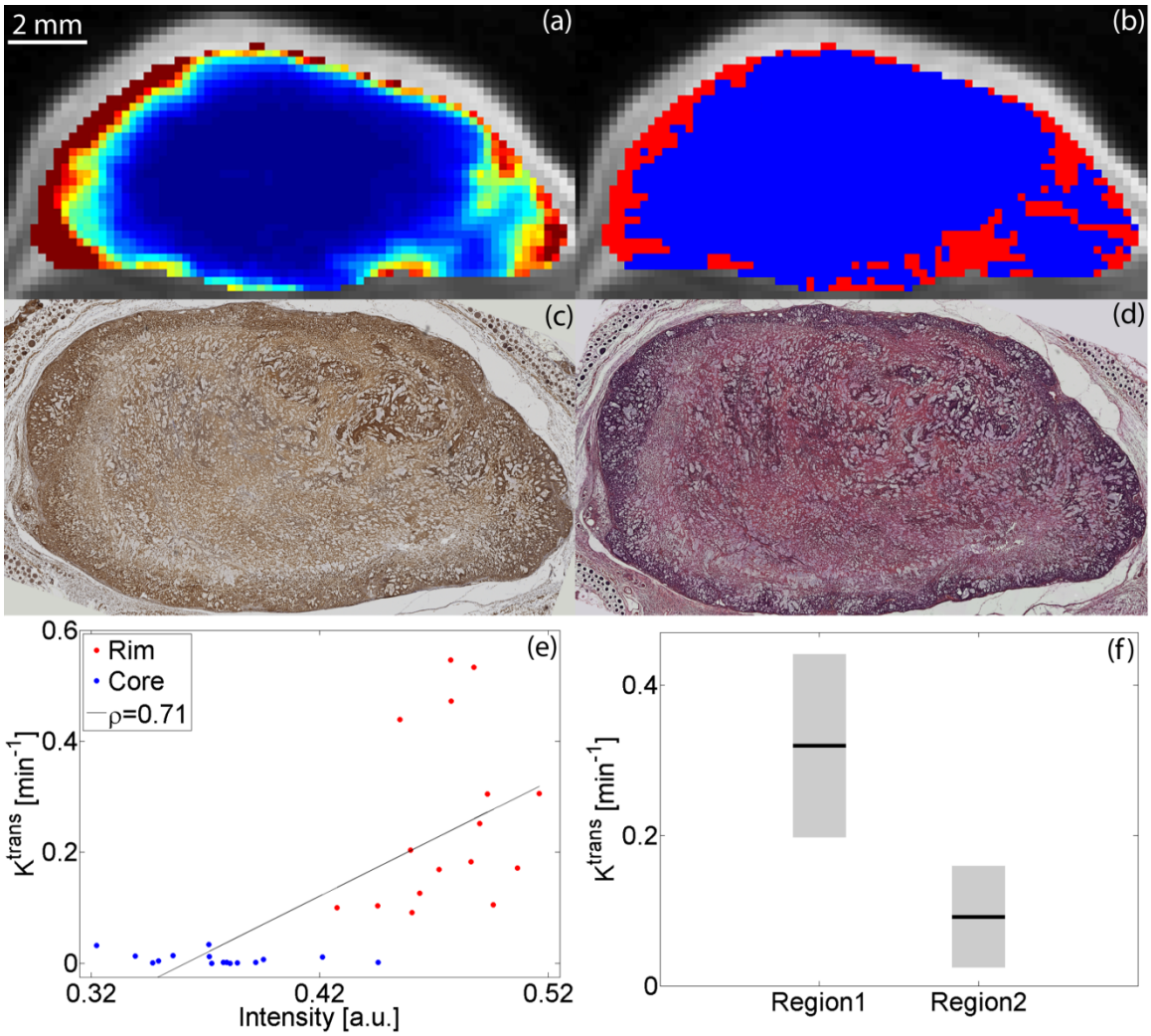

Figure 39: Correlation between (a) K^{trans}, (b) TTP regions, (c) CD31, and (d) H&E staining in a representative animal from the treatment group. (e) A significant correlation was found between K^{trans} and the intensity of the brown channel in a micrograph of a histology slide stained with CD31. The blue and red datapoints are from measurements in manually drawn ROIs in the core and rim of the tumor respectively. (f) A comparison between region 1 and region 2 for all animals in this study shows that K^{trans} is significantly higher (approximately three-fold) in the fast-enhancing regions. TTP selects for regions with high permeability and microvascular density.

The evolution of the TTP histogram, the fast- and slow-enhancing regions, and K^{trans} map are shown in Figure 40 for a representative animal at day 0, 2, 9, and 16. Notice the change in the distribution of TTP as the tumor progresses. Initially (day 0 and 2), the majority of the tumor pixels are found in the fast-enhancing region. By day 9, there is a drastic change in overall enhancement as can be seen in the TTP histogram and the distribution of region 1 and region 2. A comparison of the K^{trans} and TTP maps reveals a clear correlation between high permeability values and fast-enhancing regions and low permeability values and slow-enhancing regions.

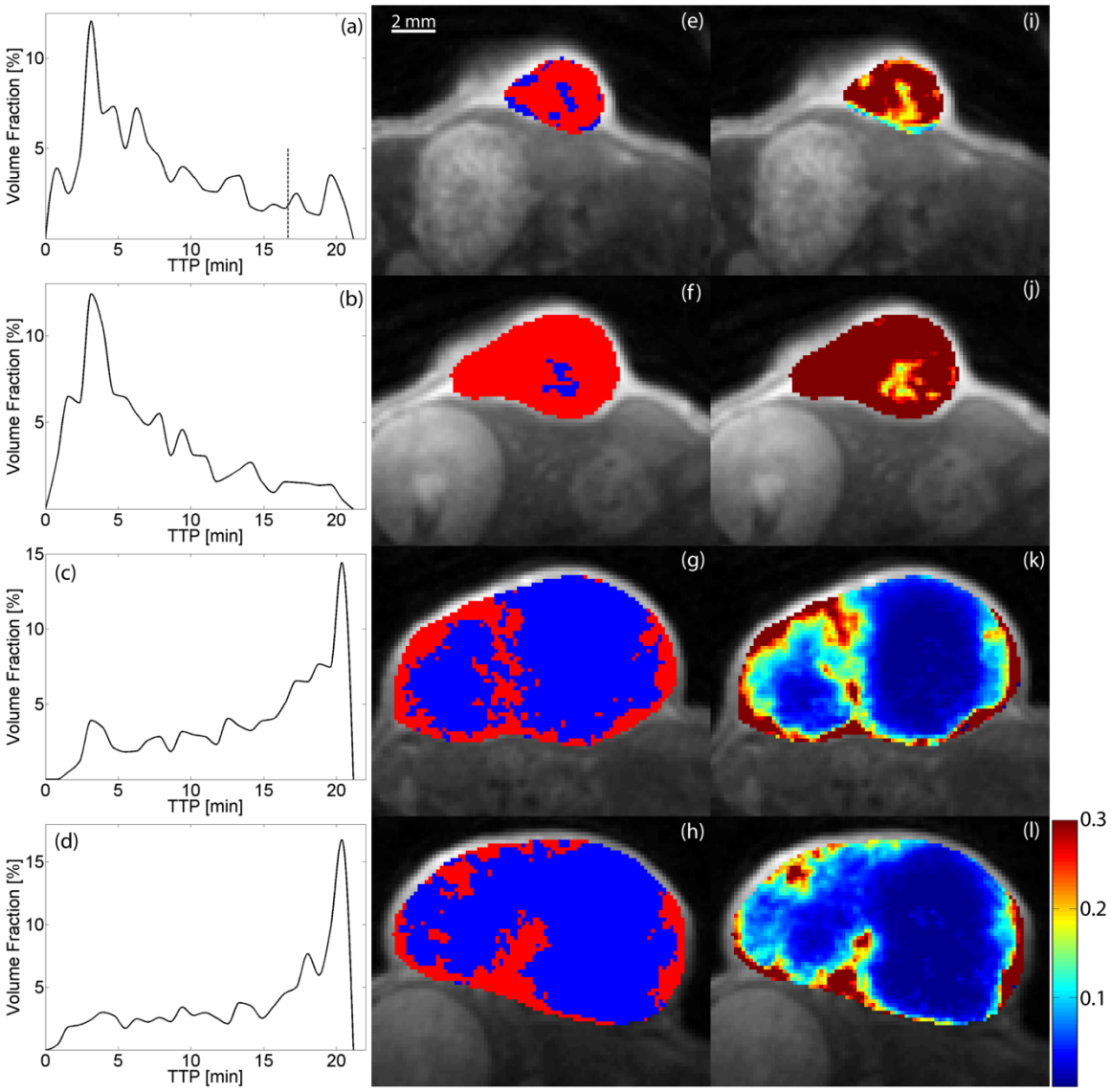

Figure 40: TTP histogram (a-d), fast- and slow-enhancing regions (e-h), and K^{trans} map (i-l) as a function of tumor volume in a representative animal at day 0 (a, e, i), day 2 (b, f, j), day 9 (c, g, k), and day 16 (d, h, l). Notice the change in the distribution of TTP as the tumor progresses. The K^{trans} and TTP maps reveal a clear correlation between high permeability values and fast-enhancing regions and low permeability values and slow-enhancing regions. Dashed line in panel (a) shows the threshold used to separate region 1 and region 2. Colormap is in units of min^{-1}.

7.4.2 Identifying regions of therapeutic effect

The initial tumor volume ($\mu \pm \sigma$) for the treatment and control group was 91 ± 37 μL and 115 ± 41 μL respectively. Figure 41 shows the effect of bevacizumab on tumor volume. The doubling time in the treatment arm was significantly longer than in the control arm. On average, treatment induced a tumor growth delay of approximately 8.4 days and extended the doubling time by more than two-fold (7.6 days vs. 16.1 days).

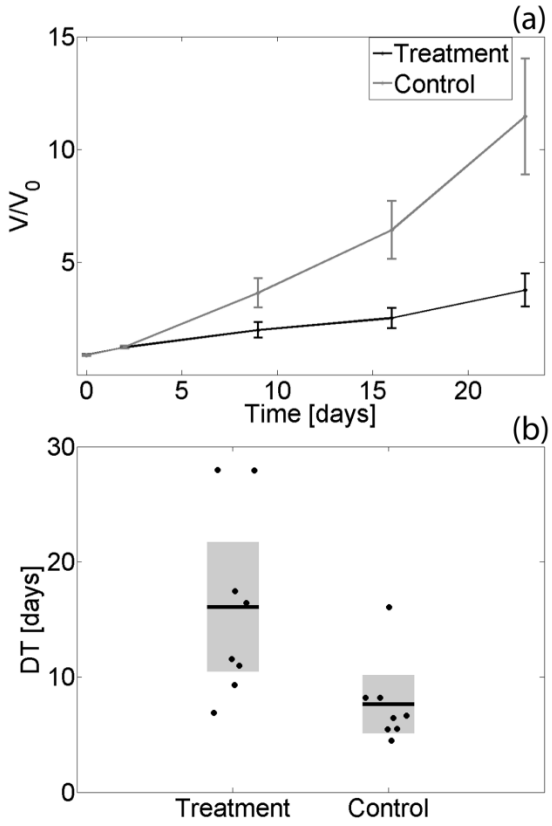

Figure 41: Tumor doubling time was significantly increased treatment group. (a) Relative tumor volume (μ±sem) as a function of time (b) Treatment extended the doubling time by more than two-fold (7.6 days vs. 16.1 days).

The effect of bevacizumab on the permeability parameter and the relative volume of region 1 and 2 is presented in Figure 42. In the fast-enhancing region, the mean K^{trans} is significantly lower in the treatment group only at day 9; in the slow-enhancing region, this parameter is not significantly different between the control and treatment cohort at any point during therapy. Interestingly, at day 9, K^{trans} is significantly lower in the treatment group when the mean is taken over the entire tumor volume. At the same time point, in the treatment group the relative volume of region 1 was found to be significantly lower, while that of region 2 significantly higher. The injection of the contrast agent in three datasets (out of 80) was unsuccessful. The K^{trans} values from those scans were not included in the above analysis.

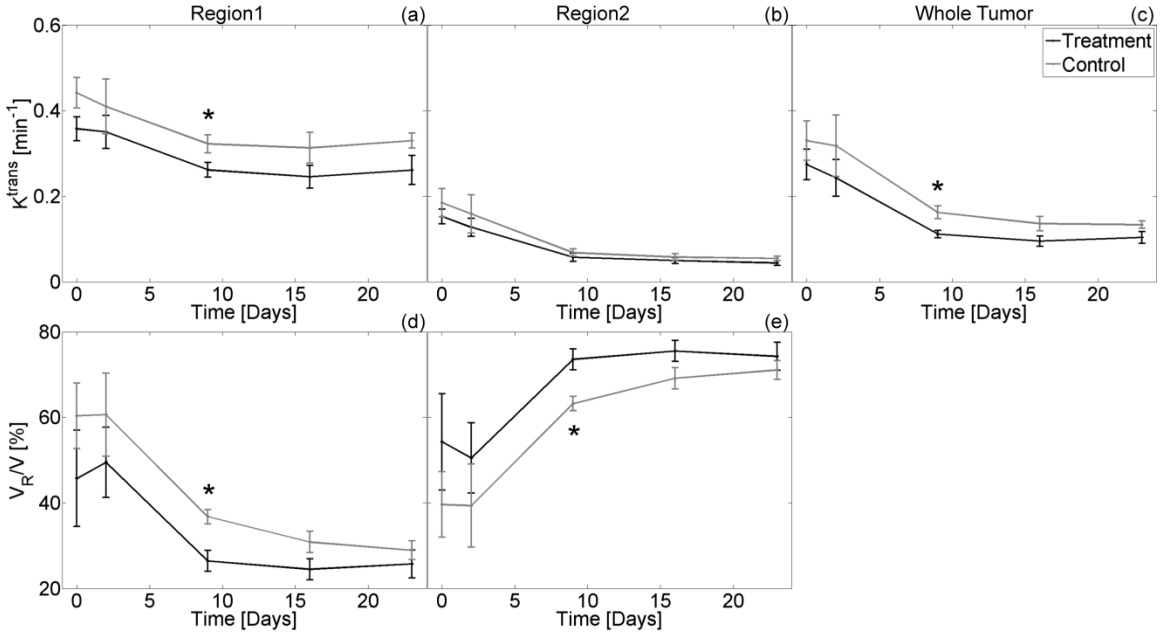

Figure 42: Effect of bevacizumab on the permeability parameter (a-c) and the relative volume of region 1 and 2 (d-e). In the fast-enhancing region, the mean K^{trans} is significantly lower in the treatment group at day 9 (a); in the slow-enhancing region, this parameter is not significantly different between the control and treatment cohort at any point during therapy (b). At day 9, K^{trans} is significantly lower in the treatment group when the mean is taken over the entire tumor volume (c). At the same time point, in the treatment group the relative volume of region 1 was found to be significantly lower (d), while that of region 2 significantly higher (e). V_R=volume of region (1 or 2), V= tumor volume.

7.5 Discussion

One of the main metrics for evaluating treatment response in solid tumors is lesion size (Therasse, Arbuck et al. 2000). Although a decrease in lesion volume, leading to a complete response, would be the most desirable outcome, the mechanism of action in some therapeutic agents may not cause tumor regression. Tumor growth studies that measure a treatment effect remain non-specific in elucidating the purported mechanism

of action. In the recent past, biomarkers from several imaging modalities have provided crucial complementary information to the findings of traditional clinical studies of anticancer therapies (Weissleder 2006; Judenhofer, Wehrl et al. 2008).

In this study, the time-to-peak of MR signal was used to segment the tumor microenvironment into two regions with distinct enhancement kinetics responding differently to an anti-angiogenic therapeutic agent. The regions were defined by setting a threshold of 1000 sec in the histogram of the TTP parameter. The segmented sub-volumes were located in predictable patterns, with the fast- and slow-enhancing regions in the periphery and core of the tumor respectively. As shown in Figure 39(f), the permeability parameter K^{trans} was significantly different in these domains. More importantly, CD31 and H&E staining reveal a similar spatial distribution of microvascular density, cell density, and DCE-MRM parameters. Previous studies have also found a significant correlation between TTP and microvascular density (Yabuuchi, Fukuya et al. 2003). A separation of tumor volume into distinct regions derived from DCE-MRI has also been reported (Marzola, Farace et al. 2003). Other investigators have attempted to use the TTP parameter as a semi-quantitative diagnostic biomarker in discriminating between benign/malignant lesions (Jansen, Newstead et al. 2007), or as a predictor for response to therapy (Zahra, Tan et al. 2009). Here we find that the mean K^{trans} in the fast-enhancing region (as defined by thresholding the TTP parameter) is

significantly lower in the treatment group at day 9 of the regimen. The difference in this region determines the statistical difference in the mean of K^{trans} in the tumor volume, as there was no significant difference in the mean of K^{trans} in the slow-enhancing region. If decrease in mean K^{trans} is assumed to indicate treatment success (O'Connor, Jackson et al. 2012), then the regions determined by the TTP parameter identify the tumor location where the therapeutic agent has its effect. Interestingly, at day 9 the fractional volume of the fast-enhancing region is significantly lower in the treatment group suggesting a direct therapeutic effect in regions of higher microvascular density.

The choice of the TTP threshold equal to 1000 sec was empirical. The threshold was varied continuously until a match between the TTP regions, the K^{trans} map, and the histology slides was observed. Figure 43 demonstrates how the TTP parameter is

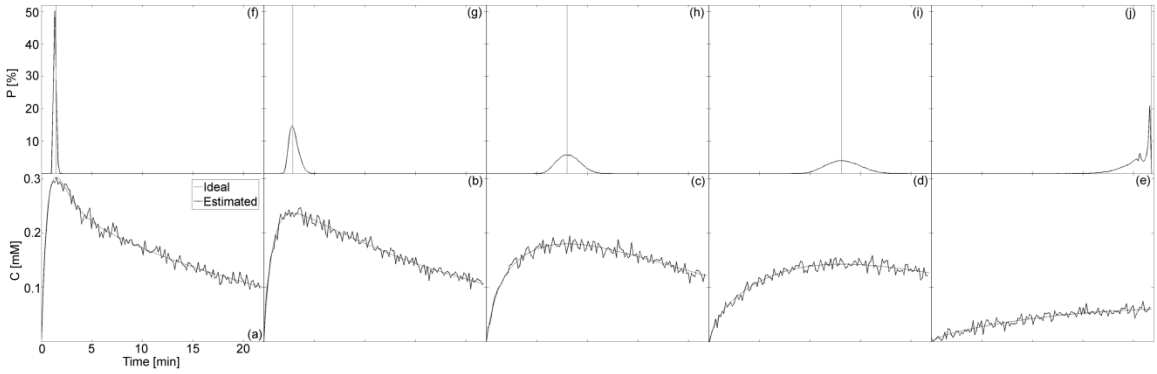

Figure 43: TTP is estimated with a varying degree of precision as its value increases. (a-e) Simulated (gray) concentration curves as K^{trans} is decreased and estimated (black) curves with added noise. Notice the change in TTP as K^{trans} is decreased. (f-j) Ideal value of TTP (delta function in gray) and distribution (black) of estimated TTP after smoothing with optimal Savitzky-Golay filter.

estimated with a varying degree of precision as its value increases. Concentration curves were simulated as K^{trans} was decreased and noise was added as previously described (Subashi, Choudhury et al. 2014). Following the smoothing operation with the Savitzky-Golay filter, it was found that larger TTP values were generally estimated with worse precision. In particular, notice in Figure 43(j) the shape of the TTP histogram when the maximum of the curve is at the last temporal point. The distribution of the parameter in this case, justifies the empirical finding of a threshold equal to 1000 sec. Lastly, the varying standard deviation of the estimated TTP distribution for different ideal TTP values may be an explanation for the irregular shape of the distributions observed in vivo. It is conceivable that an increase in spatial/temporal resolution may help resolve more than two regions in the TTP histogram.

7.6 Conclusions

The histogram of the time-to-peak provides useful knowledge about the spatial distribution of K^{trans} and microvascular density. Two regions with distinct kinetic parameters were identified when the TTP map from DCE-MRM was thresholded at 1000 sec. The effect of bevacizumab, as measured by a decrease in K^{trans}, was confined to one of these regions. DCE-MRM studies may contribute unique insights into the response of the tumor microenvironment to therapy.

8. Summary

Volumetric keyhole imaging with projection acquisition provides a means to increase spatial and temporal resolution and coverage over that provided by existing 2D Cartesian protocols. The technique allows one to measure complex heterogeneity of kinetic parameters with isotropic, microscopic spatial resolution. Current small-animal imaging systems and pulse sequences robust to motion artifacts have the capacity for reproducible quantitative acquisitions with DCE-MRM. In these circumstances, it is feasible to achieve a level of precision limited only by physiologic variability. The incorporation of semi-quantitative kinetic parameters in the analysis of DCE-MRM data provides a way for identifying tumor subpopulations responding differently to therapy.

Appendix A

Table A.1: Experimental protocols used in preclinical pharmacologic studies of bevacizumab and A4.6.1 in human tumor xenografts. Adapted from Gerber et al. (Gerber and Ferrara 2005).

Cell line	Antibody	Dosing regimens	Species	End points	Noteworthy observations
A673	A4.6.1	10-100 μg i.p. twice weekly	Mouse/beige nude	Tumor weight, size, vascularity	96% tumor inhibition; decrease in vessel density
A673	A4.6.1	0.05-5 mg/kg i.p. twice weekly	Mouse/beige nude	Tumor area and weight, serum concentration of A4.6.1	Dose-dependent inhibition of tumor growth >80% at >10 μg/mL
A673	A4.6.1	10-200 μg i.p. twice weekly	Mouse/beige nude	Tumor growth, vascularization, mitotic index tumor cells	Complete inhibition of tumor growth and neovascularization
G55	A4.6.1	10-100 μg i.p. twice weekly	Mouse/beige nude	Tumor weight, size, vascular density	80% tumor inhibition; decrease in vessel density
G55	A4.6.1	600 μg i.p. q2d	Rat/athymic nude	Survival, tumor size, and vascularity	95% increase in survival; decrease in tumor vascularity and growth rates
U87	A4.6.1	98.4 μg i.p. q3d	Mouse/SCID	Tumor growth, vascularization, permeability, vessel diameter	Vessel disappearance; reduction in vessel permeability and diameter

U87	A4.6.1	100 μg i.p. q2d, six doses combination and radiation therapy	Mouse/athymic NCr/Sed *nu/nu*	Tumor growth, vascular density, oxygenation (pO_2), apoptosis of tumor cells, IFP	Decrease in tumor growth and IFP (73% in U87); increase in apoptosis; increase in pO_2 in some tumors
U87	A4.6.1	1 mg i.p. q3d, three doses	Rat/athymic nude	MRI: tumor vascular permeability and tumor growth	Inhibition of microvascular permeability and tumor growth
SK-LMS-1	A4.6.1	10-100 μg i.p. twice weekly	Mouse/beige nude xid	Tumor weight, size, vascular density	70% tumor inhibition; decrease in vessel density
SKOV-3	A4.6.1	100 μg i.p. twice weekly	Mouse/BALB/c *nu/nu*	Tumor weight and ascites formation in the peritoneal cavity	Inhibition of s.c. tumor growth; complete inhibition of ascites formation
SKOV-3	A4.6.1	1 mg i.p. q3d, five doses	Rat/athymic mice	Microvascular permeability and ascites formation	Reduction in tumor microvascular permeability and ascites production
OVCAR3	A4.6.1	5 mg/kg i.p. twice weekly combination with (paclitaxel)	Mouse/athymic	Tumor burden and ascites formation, tumor cell apoptosis	Significant reduction in tumor burden in the combination treatment (83.3%). Complete absence of ascites fluid in the combined or A4.6.1 only group
DU145	A4.6.1	100 μg i.p. twice weekly	Mouse/beige nude xid	Tumor growth and vascularization	Complete inhibition of tumor growth and neovascularization

DU145	A4.6.1	10 + 100 μg i.p. twice weekly	Mouse/CB-17 SCID/SCID	Primary tumor growth and lung metastases	Suppression of primary tumor growth (82%) and lung metastases
CWR22R	Bevacizumab	5 mg/kg i.p. twice weekly combination with chemo (paclitaxel)	Mouse/athymic nude BALB/c	Tumor growth and microvessel density	Inhibition of established tumor growth by 85% ($P < 0.01$). Combination treatment resulted in greater inhibition of tumor growth than either agent alone
LS174T	A4.6.1	98.4 μg i.p. bolus	Mouse/SCID	Tumor growth, vascularization, vascular permeability, and vessel diameter	Vessel appearance; reduction in vessel permeability and diameter
HM7	A4.6.1	10-200 μg i.p. twice weekly	Mouse/athymic	Tumor growth and liver metastases	90% Reduction in tumor size of primary tumor; reduction in liver metastases
LS174T	A4.6.1	100 μg i.p. q2d, six doses combination with radiation therapy	Mouse/athymic NCr/Sed *nu*/*nu*	Tumor growth, vascular density, oxygenation (pO_2), apoptosis of tumor cells, IFP	>70% decrease in tumor growth and IFP increase in tumor cell apoptosis; increase in pO_2 in some tumors
SK-NEP-1	A4.6.1	100 μg i.p. twice weekly	Mouse/nude	Tumor weight and lung metastases	Significant >95% reduction in tumor weight and >40% in lung metastases

SK-NEP-1	A4.6.1	100 μg i.p. twice weekly	Mouse NCr athymic	Tumor weight and growth and vascular architecture	Significant repression of tumor growth
SK-NEP-1	A4.6.1	100 μg i.p. twice weekly, 10 doses combination with chemo (topotecan)	Mouse/athymic	Tumor vasculature, endothelial cell apoptosis, and tumor weight	Significant reduction in tumor growth, vascularity, and lung metastases. Increased endothelial cell apoptosis
HuH-6	A4.6.1	100 μg i.p. twice weekly	Mouse/NCr athymic	Tumor growth and vascularity	Significant inhibition of tumor growth ($P < 0.0003$) decreased vascularity and dilated vessels
NGP-GFP	A4.6.1	100 μg i.p. twice weekly	Mouse/NCr athymic	Tumor weight and growth and vascular architecture	Neuroblastoma less effectively suppressed than Wilms' tumors. Novel vascular structures induced by anti-VEGF in neuroblastoma
NGP-GFP	A4.6.1	100 μg i.p. twice weekly combination with chemo (topotecan)	Mouse/NCr athymic	Tumor weights and vascularity	Tumor weights significantly reduced in topotecan and combination treatment ($P < 0.0007$)
MDA-435	A4.6.1	30 mg/kg i.p. q3d, three doses	Rat/nude	Vascular permeability and tumor growth	58% Reductions in tumor growth; reduction in microvascular permeability

MDA-435	A4.6.1	Bolus 30 mg/kg i.v., one dose	Rat/athymic	24-hour tumor fractional blood volume permeability surface area product	No significant change in vascularity 24 hours after treatment, but significant suppression of vascular permeability
MCF-7, ZR-75, SK-BR-3	A4.6.1	200 μg i.p. q3d combination with chemo (doxorubicin)	Mouse *nu/nu*	Vascularization and tumor growth	Tumor growth and inhibition of angiogenesis
MCF-7	Bevacizumab	0.25 mg/kg i.p. days 7 + 10 combination with chemo (docetaxel) and 2-methoxyestradiol	Mouse/nude	Matrigel invasion angiogenesis assay	Synergistic inhibition of angiogenesis in combination treatment: 75% angiogenesis as single agent or 41% in combination with chemo
P-MEL	A4.6.1	98.4 μg i.p. q3d	Mouse/SCID	Tumor growth, vascularization, vascular permeability, and vessel diameter	Vessel disappearance; reduction in vessel permeability and diameter
AsPC-1, HPAF-2	A4.6.1	100 μg i.p. twice weekly combination with matrix metalloproteinase inhibitor (BB-94)	Mouse/nude mice	Tumor volume, local and distant spread. Microvessel density and ascites formation	Single treatment reduced primary tumor size, metastasis, angiogenesis, and increased survival. Combination treatment resulted in additive effects in HPAF-2 tumor only

PANC-1	A4.6.1	300 μg i.p. q3d	Immunodeficient mice	Angiogenesis, vascular permeability, growth of tumors by intravital microscopy, angiogenic gene expression	Vessel density was significantly decreased, but vessel diameter and permeability were not altered. Tumors were smaller in the treated group

References

Ahearn, T. S., R. T. Staff, et al. (2005). "The use of the Levenberg–Marquardt curve-fitting algorithm in pharmacokinetic modelling of DCE-MRI data." Physics in Medicine and Biology 50(9).

Altbach, M. I., A. Bilgin, et al. (2005). "Processing of radial fast spin-echo data for obtaining T2 estimates from a single k-space data set." Magnetic Resonance in Medicine 54(3): 549-559.

Aychek, T., K. Vandoorne, et al. (2011). "Quantitative analysis of intravenously administered contrast media reveals changes in vascular barrier functions in a murine colitis model." Magnetic Resonance in Medicine 66(1): 235-243.

Backer, M. V., Z. Levashova, et al. (2007). "Molecular imaging of VEGF receptors in angiogenic vasculature with single-chain VEGF-based probes." Nat Med 13(4): 504-509.

Barnes, S. L., J. G. Whisenant, et al. (2013). "Assessing the reproducibility of dynamic contrast enhanced magnetic resonance imaging in a murine model of breast cancer." Magnetic Resonance in Medicine 69(6): 1721-1734.

Barnes, S. L., J. G. Whisenant, et al. (2012). "Practical Dynamic Contrast Enhanced MRI in Small Animal Models of Cancer: Data Acquisition, Data Analysis, and Interpretation." Pharmaceutics 4(3): 442-478.

Barton, K. L., K. Misuraca, et al. (2013). "PD-0332991, a CDK4/6 Inhibitor, Significantly Prolongs Survival in a Genetically Engineered Mouse Model of Brainstem Glioma." PLoS ONE 8(10).

Beatty, P. J., D. G. Nishimura, et al. (2005). "Rapid gridding reconstruction with a minimal oversampling ratio." Medical Imaging, IEEE Transactions on 24(6): 799-808.

Becher, O. J., D. Hambardzumyan, et al. (2010). "Preclinical Evaluation of Radiation and Perifosine in a Genetically and Histologically Accurate Model of Brainstem Glioma." Cancer Research 70(6): 2548-2557.

Becher, O. J. and E. C. Holland (2006). "Genetically Engineered Models Have Advantages over Xenografts for Preclinical Studies." Cancer Research 66(7): 3355-3359.

Bernstein, M., K. King, et al. (2004). Handbook of MRI Pulse Sequences. Burlington, MA, Elsevier Inc.

Bishop, J. E., G. E. Santyr, et al. (1997). "Limitations of the keyhole technique for quantitative dynamic contrast-enhanced breast MRI." Journal of Magnetic Resonance Imaging 7(4): 716-723.

Borgström, P., K. J. Hillan, et al. (1996). "Complete Inhibition of Angiogenesis and Growth of Microtumors by Anti-Vascular Endothelial Growth Factor Neutralizing Antibody: Novel Concepts of Angiostatic Therapy from Intravital Videomicroscopy." Cancer Research 56(17): 4032-4039.

Boucher, Y., M. Leunig, et al. (1996). "Tumor Angiogenesis and Interstitial Hypertension." Cancer Research 56(18): 4264-4266.

Braren, R., J. Altomonte, et al. (2011). "Validation of preclinical multiparametric imaging for prediction of necrosis in hepatocellular carcinoma after embolization." Journal of Hepatology 55(5): 1034-1040.

Brix, G., F. Kiessling, et al. (2004). "Microcirculation and microvasculature in breast tumors: Pharmacokinetic analysis of dynamic MR image series." Magnetic Resonance in Medicine 52(2): 420-429.

Buadu, L. D., J. Murakami, et al. (1996). "Breast lesions: correlation of contrast medium enhancement patterns on MR images with histopathologic findings and tumor angiogenesis." Radiology 200(3): 639-649.

Callaghan, P. T. (1991). Principles of Nuclear Magnetic Resonance Microscopy. New York, Oxford University Press Inc.

Casneuf, V. F., L. Delrue, et al. (2011). "Noninvasive Monitoring of Therapy-Induced Microvascular Changes in a Pancreatic Cancer Model Using Dynamic Contrast-Enhanced Magnetic Resonance Imaging with P846, a New Low-Diffusible Gadolinium-Based Contrast Agent." Radiation Research 175(1): 10-20.

Chan, R. W., E. A. Ramsay, et al. (2012). "The influence of radial undersampling schemes on compressed sensing reconstruction in breast MRI." Magnetic Resonance in Medicine 67(2): 363-377.

Chen, W.-T., T. T.-F. Shih, et al. (2002). "Blood perfusion of vertebral lesions evaluated with gadolinium-enhanced dynamic MRI: In comparison with compression fracture and metastasis." Journal of Magnetic Resonance Imaging 15(3): 308-314.

Cheng, H.-L. M. (2007). "T1 measurement of flowing blood and arterial input function determination for quantitative 3D T1-weighted DCE-MRI." Journal of Magnetic Resonance Imaging 25(5): 1073-1078.

Chinwalla, A. T., L. L. Cook, et al. (2002). "Initial sequencing and comparative analysis of the mouse genome." Nature 420(6915): 520-562.

Chung, C., S. Jalali, et al. (2013). "Imaging Biomarker Dynamics in an Intracranial Murine Glioma Study of Radiation and Antiangiogenic Therapy." International Journal of Radiation Oncology Biology Physics 85(3): 805-812.

Cohen, K. J., R. L. Heideman, et al. (2011). "Temozolomide in the treatment of children with newly diagnosed diffuse intrinsic pontine gliomas: a report from the Children's Oncology Group." Neuro-Oncology 13(4): 410-416.

Collingridge, D. R., V. A. Carroll, et al. (2002). "The Development of [124I]Iodinated-VG76e: A Novel Tracer for Imaging Vascular Endothelial Growth Factor in Vivo Using Positron Emission Tomography." Cancer Research 62(20): 5912-5919.

Cooley, J. W. and J. W. Tukey (1965). "An Algorithm for the Machine Calculation of Complex Fourier Series." Mathematics of Computation 19(90): 297-301.

Daniel, B. L., Y. F. Yen, et al. (1998). "Breast disease: dynamic spiral MR imaging." Radiology 209(2): 499-509.

Demidenko, E. (2010). "Three endpoints of in vivo tumour radiobiology and their statistical estimation." International Journal of Radiation Biology 86(2): 164-173.

Deoni, S. C. L., B. K. Rutt, et al. (2003). "Rapid combined T1 and T2 mapping using gradient recalled acquisition in the steady state." Magnetic Resonance in Medicine 49(3): 515-526.

Dougherty, L., G. Isaac, et al. (2007). "High frame-rate simultaneous bilateral breast DCE-MRI." Magnetic Resonance in Medicine 57(1): 220-225.

Duerk, J. L., J. S. Lewin, et al. (1996). "Application of keyhole imaging to interventional MRI: A simulation study to predict sequence requirements." Journal of Magnetic Resonance Imaging 6(6): 918-924.

Dutt, A. and V. Rokhlin (1993). "Fast Fourier Transforms for Nonequispaced Data." SIAM Journal on Scientific Computing 14(6): 1368-1393.

Eccles, C. D. and P. T. Callaghan (1986). "High-resolution imaging. The NMR microscope." Journal of Magnetic Resonance (1969) 68(2): 393-398.

Egeland, T. A. M., J.-V. Gaustad, et al. (2011). "Magnetic resonance imaging of tumor necrosis." Acta Oncologica 50(3): 427-434.

Engelbrecht, M. R., H. J. Huisman, et al. (2003). "Discrimination of Prostate Cancer from Normal Peripheral Zone and Central Gland Tissue by Using Dynamic Contrast-enhanced MR Imaging." Radiology 229(1): 248-254.

Epstein, F. J. and J.-P. Farmer (1993). "Brain-stem glioma growth patterns." Journal of Neurosurgery 78(3): 408-412.

Fangusaro, J. (2012). "Pediatric High Grade Glioma (HGG): a Review and Update on Tumor Clinical Characteristics and Biology." Frontiers in Oncology 2.

Farace, P., F. Merigo, et al. (2011). "DCE-MRI using small-molecular and albumin-binding contrast agents in experimental carcinomas with different stromal content." European Journal of Radiology 78(1): 52-59.

Farrar, C. T., W. S. Kamoun, et al. (2011). "Sensitivity of MRI Tumor Biomarkers to VEGFR Inhibitor Therapy in an Orthotopic Mouse Glioma Model." PLoS ONE 6(3).

Ferrara, N. and W. J. Henzel (1989). "Pituitary follicular cells secrete a novel heparin-binding growth factor specific for vascular endothelial cells." Biochemical and Biophysical Research Communications 161(2): 851-858.

Folkman, J. (1971). "Tumor Angiogenesis: Therapeutic Implications." New England Journal of Medicine 285(21): 1182-1186.

Fram, E. K., R. J. Herfkens, et al. (1987). "Rapid calculation of T1 using variable flip angle gradient refocused imaging." Magnetic Resonance Imaging 5(3): 201-208.

Fukumura, D., L. Xu, et al. (2001). "Hypoxia and Acidosis Independently Up-Regulate Vascular Endothelial Growth Factor Transcription in Brain Tumors in Vivo." Cancer Research 61(16): 6020-6024.

Gans, P. and J. B. Gill (1983). "Examination of the Convolution Method for Numerical Smoothing and Differentiation of Spectroscopic Data in Theory and in Practice." Applied Spectroscopy 37(6): 515-520.

Geirnaerdt, M. J. A., P. C. W. Hogendoorn, et al. (2000). "Cartilaginous Tumors: Fast Contrast-enhanced MR Imaging." Radiology 214(2): 539-546.

Gerber, H.-P. and N. Ferrara (2005). "Pharmacology and Pharmacodynamics of Bevacizumab as Monotherapy or in Combination with Cytotoxic Therapy in Preclinical Studies." Cancer Research 65(3): 671-680.

Glover, G. H., C. E. Hayes, et al. (1985). "Comparison of linear and circular polarization for magnetic resonance imaging." Journal of Magnetic Resonance (1969) 64(2): 255-270.

Glover, G. H. and J. M. Pauly (1992). "Projection Reconstruction Techniques for Reduction of Motion Effects in MRI." Magnetic Resonance in Medicine 28(2): 275-289.

Gmitro, A. F. and A. L. Alexander (1993). "Use of a projection reconstruction method to decrease motion sensitivity in diffusion-weighted MRI." Magnetic Resonance in Medicine 29(6): 835-838.

Gudbjartsson, H. and S. Patz (1995). "The rician distribution of noisy mri data." Magnetic Resonance in Medicine 34(6): 910-914.

Gulliksrud, K., K. M. Øvrebø, et al. (2011). "Differentiation between hypoxic and non-hypoxic experimental tumors by dynamic contrast-enhanced magnetic resonance imaging." Radiotherapy and Oncology 98(3): 360-364.

Haacke, E. M., R. W. Brown, et al. (1999). Magnetic Resonance Imaging: Physical Principles and Sequence Design, Wiley.

Han, M., B. L. Daniel, et al. (2008). "Accelerated bilateral dynamic contrast-enhanced 3D spiral breast MRI using TSENSE." Journal of Magnetic Resonance Imaging 28(6): 1425-1434.

Hargrave, D., N. Chuang, et al. (2008). "Conventional MRI cannot predict survival in childhood diffuse intrinsic pontine glioma." Journal of Neuro-Oncology 86(3): 313-319.

Heilmann, M., F. Kiessling, et al. (2006). "Determination of Pharmacokinetic Parameters in DCE MRI: Consequence of Nonlinearity Between Contrast Agent Concentration and Signal Intensity." Investigative Radiology 41(6): 536-543.

Henderson, E., B. K. Rutt, et al. (1998). "Temporal sampling requirements for the tracer kinetics modeling of breast disease." Magnetic Resonance Imaging 16(9): 1057-1073.

Henkelman, R. M. (1985). "Measurement of signal intensities in the presence of noise in MR images." Medical Physics 12(2): 232-233.

Hillman, G. G., V. Singh-Gupta, et al. (2009). "Dynamic contrast-enhanced magnetic resonance imaging of vascular changes induced by sunitinib in papillary renal cell carcinoma xenograft tumors." Neoplasia 11(9): 910-920.

Hipp, S. J., E. Steffen-Smith, et al. (2011). "Predicting outcome of children with diffuse intrinsic pontine gliomas using multiparametric imaging." Neuro-Oncology 13(8): 904-909.

Hoge, R. D., R. K. S. Kwan, et al. (1997). "Density compensation functions for spiral MRI." Magnetic Resonance in Medicine 38(1): 117-128.

Hotz, H. G., O. J. Hines, et al. (2003). "Evaluation of Vascular Endothelial Growth Factor Blockade and Matrix Metalloproteinase Inhibition as a Combination

Therapy for Experimental Human Pancreatic Cancer." Journal of Gastrointestinal Surgery 7(2): 220-228.

Hu, X. (1994). "On the "keyhole" technique." Journal of Magnetic Resonance Imaging 4(2): 231-231.

Hugo, J. W. L. A., K. Jaspers, et al. (2011). "The precision of pharmacokinetic parameters in dynamic contrast-enhanced magnetic resonance imaging: the effect of sampling frequency and duration." Physics in Medicine and Biology 56(17).

Jackson, J. I., C. H. Meyer, et al. (1991). "Selection of a convolution function for Fourier inversion using gridding." Medical Imaging, IEEE Transactions on 10(3): 473-478.

Jacob, H. J., D. M. Brown, et al. (1995). "A genetic linkage map of the laboratory rat, Rattus norvegicus." Nat Genet 9(1): 63-69.

Jalali, S., C. Chung, et al. (2014). "MRI biomarkers identify the differential response of glioblastoma multiforme to anti-angiogenic therapy." Neuro-Oncology 16(6): 868-879.

Jansen, S. A., G. M. Newstead, et al. (2007). "Pure Ductal Carcinoma in Situ: Kinetic and Morphologic MR Characteristics Compared with Mammographic Appearance and Nuclear Grade." Radiology 245(3): 684-691.

Jayson, G. C., J. Zweit, et al. (2002). "Molecular Imaging and Biological Evaluation of HuMV833 Anti-VEGF Antibody: Implications for Trial Design of Antiangiogenic Antibodies." Journal of the National Cancer Institute 94(19): 1484-1493.

Jiayu, S., L. Yanhui, et al. (2009). "Least-Square NUFFT Methods Applied to 2-D and 3-D Radially Encoded MR Image Reconstruction." Biomedical Engineering, IEEE Transactions on 56(4): 1134-1142.

John, R. and H. Ross (2010). The Global Economic Cost of Cancer. Atlanta, GA, American Cancer Society.

Johnson, G. A., A. Badea, et al. (2010). "Waxholm Space: An image-based reference for coordinating mouse brain research." NeuroImage 53(2): 365-372.

Johnson, G. A., H. Benveniste, et al. (1993). "Histology by magnetic resonance microscopy." Magnetic resonance quarterly 9(1): 1-30.

Johnson, G. A., E. Calabrese, et al. (2012). "A multidimensional magnetic resonance histology atlas of the Wistar rat brain." NeuroImage 62(3): 1848-1856.

Johnson, J. and T. Wilson (1966). "A model for capillary exchange." American Journal of Physiology -- Legacy Content 210(6): 1299-1303.

Johnson, K. O. and J. G. Pipe (2009). "Convolution kernel design and efficient algorithm for sampling density correction." Magnetic Resonance in Medicine 61(2): 439-447.

Jones, R. A., O. Haraldseth, et al. (1993). "K-space substitution: A novel dynamic imaging technique." Magnetic Resonance in Medicine 29(6): 830-834.

Judenhofer, M. S., H. F. Wehrl, et al. (2008). "Simultaneous PET-MRI: a new approach for functional and morphological imaging." Nat Med 14(4): 459-465.

Kermode, A. G., P. S. Tofts, et al. (1988). "Early lesion of multiple sclerosis." The Lancet 332(8621): 1203-1204.

Kershaw, L. E. and D. L. Buckley (2006). "Precision in measurements of perfusion and microvascular permeability with T1-weighted dynamic contrast-enhanced MRI." Magnetic Resonance in Medicine 56(5): 986-992.

Khuong-Quang, D.-A., P. Buczkowicz, et al. (2012). "K27M mutation in histone H3.3 defines clinically and biologically distinct subgroups of pediatric diffuse intrinsic pontine gliomas." Acta Neuropathologica 124(3): 439-447.

Kim, H., K. Folks, et al. (2011). "DCE-MRI Detects Early Vascular Response in Breast Tumor Xenografts Following Anti-DR5 Therapy." Molecular Imaging and Biology 13(1): 94-103.

Kim, K. J., B. Li, et al. (1992). "The Vascular Endothelial Growth Factor Proteins: Identification of Biologically Relevant Regions by Neutralizing Monoclonal Antibodies." Growth Factors 7(1): 53-64.

Kim, K. J., B. Li, et al. (1993). "Inhibition of vascular endothelial growth factor-induced angiogenesis suppresses tumour growth in vivo." Nature 362(6423): 841-844.

Kirsch, D. G., D. M. Dinulescu, et al. (2007). "A spatially and temporally restricted mouse model of soft tissue sarcoma." Nat Med 13(8): 992-997.

Klement, G., S. Baruchel, et al. (2000). "Continuous low-dose therapy with vinblastine and VEGF receptor-2 antibody induces sustained tumor regression without overt toxicity." The Journal of Clinical Investigation 105(8): R15-R24.

Korpanty, G., J. G. Carbon, et al. (2007). "Monitoring Response to Anticancer Therapy by Targeting Microbubbles to Tumor Vasculature." Clinical Cancer Research 13(1): 323-330.

Kuhl, C. K., P. Mielcareck, et al. (1999). "Dynamic Breast MR Imaging: Are Signal Intensity Time Course Data Useful for Differential Diagnosis of Enhancing Lesions?" Radiology 211(1): 101-110.

Landis, C. S., X. Li, et al. (2000). "Determination of the MRI contrast agent concentration time course in vivo following bolus injection: Effect of equilibrium transcytolemmal water exchange." Magnetic Resonance in Medicine 44(4): 563-574.

Larson, A. C. and O. P. Simonetti (2001). "Real-time cardiac cine imaging with SPIDER: Steady-state projection imaging with dynamic echo-train readout." Magnetic Resonance in Medicine 46(6): 1059-1066.

Larsson, C., M. Kleppestø, et al. (2012). "Sampling requirements in DCE-MRI based analysis of high grade gliomas: Simulations and clinical results." Journal of Magnetic Resonance Imaging.

Lauterbur, P. C. (1973). "Image Formation by Induced Local Interactions: Examples Employing Nuclear Magnetic Resonance." Nature 242(5394): 190-191.

Law, M., S. Yang, et al. (2003). "Glioma Grading: Sensitivity, Specificity, and Predictive Values of Perfusion MR Imaging and Proton MR Spectroscopic Imaging Compared with Conventional MR Imaging." American Journal of Neuroradiology 24(10): 1989-1998.

Lee, C.-G., M. Heijn, et al. (2000). "Anti-Vascular Endothelial Growth Factor Treatment Augments Tumor Radiation Response under Normoxic or Hypoxic Conditions." Cancer Research 60(19): 5565-5570.

Lewis, P. W., M. M. Müller, et al. (2013). "Inhibition of PRC2 Activity by a Gain-of-Function H3 Mutation Found in Pediatric Glioblastoma." Science 340(6134): 857-861.

Li, K.-L., X. P. Zhu, et al. (2000). "Improved 3D quantitative mapping of blood volume and endothelial permeability in brain tumors." Journal of Magnetic Resonance Imaging 12(2): 347-357.

Lober, R., Y.-J. Cho, et al. (2014). "Diffusion-weighted MRI derived apparent diffusion coefficient identifies prognostically distinct subgroups of pediatric diffuse intrinsic pontine glioma." Journal of Neuro-Oncology 117(1): 175-182.

Loveless, M. E., J. Halliday, et al. (2012). "A quantitative comparison of the influence of individual versus population-derived vascular input functions on dynamic contrast enhanced-MRI in small animals." Magnetic Resonance in Medicine 67(1): 226-236.

Lowe, M. J. and J. A. Sorenson (1997). "Spatially filtering functional magnetic resonance imaging data." Magnetic Resonance in Medicine 37(5): 723-729.

Macovski, A. (1996). "Noise in MRI." Magnetic Resonance in Medicine 36(3): 494-497.

Marzola, P., P. Farace, et al. (2003). "In vivo mapping of fractional plasma volume (fpv) and endothelial transfer coefficient (Kps) in solid tumors using a macromolecular contrast agent: Correlation with histology and ultrastructure." International Journal of Cancer 104(4): 462-468.

Matsubayashi, R., Y. Matsuo, et al. (2000). "Breast Masses with Peripheral Rim Enhancement on Dynamic Contrast-enhanced MR Images: Correlation of MR Findings with Histologic Features and Expression of Growth Factors." Radiology 217(3): 841-848.

Maxwell, R. J., J. Wilson, et al. (2002). "Evaluation of the anti-vascular effects of combretastatin in rodent tumours by dynamic contrast enhanced MRI." NMR in Biomedicine 15(2): 89-98.

McConville, P., D. Hambardzumyan, et al. (2007). "Magnetic Resonance Imaging Determination of Tumor Grade and Early Response to Temozolomide in a Genetically Engineered Mouse Model of Glioma." Clinical Cancer Research 13(10): 2897-2904.

Medved, M., G. Karczmar, et al. (2004). "Semiquantitative analysis of dynamic contrast enhanced MRI in cancer patients: Variability and changes in tumor tissue over time." Journal of Magnetic Resonance Imaging 20(1): 122-128.

Melnyk, O., M. Zimmerman, et al. (1999). "Neutralizing Anti-Vascular Endothelial Growth Factor Antibody Inhibits Further Growth of Established Prostate Cancer and Metastases in a Pre-Clinical Model." The Journal of Urology 161(3): 960-963.

Mesiano, S., N. Ferrara, et al. (1998). "Role of Vascular Endothelial Growth Factor in Ovarian Cancer: Inhibition of Ascites Formation by Immunoneutralization." The American Journal of Pathology 153(4): 1249-1256.

Meyer, C. H., B. S. Hu, et al. (1992). "Fast Spiral Coronary Artery Imaging." Magnetic Resonance in Medicine 28(2): 202-213.

Mistry, N. N., J. Pollaro, et al. (2008). "Pulmonary perfusion imaging in the rodent lung using dynamic contrast-enhanced MRI." Magnetic Resonance in Medicine 59(2): 289-297.

Mitsouras, D., R. V. Mulkern, et al. (2007). "Basis function cross-correlations for Robust k-space sample density compensation, with application to the design of radiofrequency excitations." Magnetic Resonance in Medicine 57(2): 338-352.

Mordenti, J., K. Thomsen, et al. (1999). "Efficacy and Concentration-Response of Murine Anti-VEGF Monoclonal Antibody in Tumor-Bearing Mice and Extrapolation to Humans." Toxicologic Pathology 27(1): 14-21.

Murase, K. (2004). "Efficient method for calculating kinetic parameters using T1-weighted dynamic contrast-enhanced magnetic resonance imaging." Magnetic Resonance in Medicine 51(4): 858-862.

Nishimura, D. G., J. I. Jackson, et al. (1991). "On the nature and reduction of the displacement artifact in flow images." Magnetic Resonance in Medicine 22(2): 481-492.

Noebauer-Huhmann, I. M., P. Szomolanyi, et al. (2010). "Gadolinium-Based Magnetic Resonance Contrast Agents at 7 Tesla: In Vitro T1 Relaxivities in Human Blood Plasma." Investigative Radiology 45(9): 554-558.

Noll, D. C. (1997). "Multishot rosette trajectories for spectrally selective MR imaging." Medical Imaging, IEEE Transactions on 16(4): 372-377.

O'Connor, J. P. B., A. Jackson, et al. (2012). "Dynamic contrast-enhanced MRI in clinical trials of antivascular therapies." Nat Rev Clin Oncol 9(3): 167-177.

O'Donnell, M. and W. A. Edelstein (1985). "NMR imaging in the presence of magnetic field inhomogeneities and gradient field nonlinearities." Medical Physics 12(1): 20-26.

Østergaard, L., R. M. Weisskoff, et al. (1996). "High resolution measurement of cerebral blood flow using intravascular tracer bolus passages. Part I: Mathematical approach and statistical analysis." Magnetic Resonance in Medicine 36(5): 715-725.

Ostrom, Q. T., H. Gittleman, et al. (2013). "CBTRUS Statistical Report: Primary Brain and Central Nervous System Tumors Diagnosed in the United States in 2006-2010." Neuro-Oncology 15(suppl 2): 1-56.

Padhani, A. R. and J. E. Husband (2001). "Dynamic Contrast-enhanced MRI Studies in Oncology with an Emphasis on Quantification, Validation and Human Studies." Clinical Radiology 56(8): 607-620.

Padhani, A. R. and K. A. Miles (2010). "Multiparametric Imaging of Tumor Response to Therapy." Radiology 256(2): 348-364.

Paigen, K. (1995). "A miracle enough: the power of mice." Nat Med 1(3): 215-220.

Parker, G. J. M., C. Roberts, et al. (2006). "Experimentally-derived functional form for a population-averaged high-temporal-resolution arterial input function for dynamic contrast-enhanced MRI." Magnetic Resonance in Medicine 56(5): 993-1000.

Patlak, C. S., R. G. Blasberg, et al. (1983). "Graphical Evaluation of Blood-to-Brain Transfer Constants from Multiple-Time Uptake Data." J Cereb Blood Flow Metab 3(1): 1-7.

Paugh, B. S., A. Broniscer, et al. (2011). "Genome-Wide Analyses Identify Recurrent Amplifications of Receptor Tyrosine Kinases and Cell-Cycle Regulatory Genes in Diffuse Intrinsic Pontine Glioma." Journal of Clinical Oncology 29(30): 3999-4006.

Peters, D. C., F. R. Korosec, et al. (2000). "Undersampled projection reconstruction applied to MR angiography." Magnetic Resonance in Medicine 43(1): 91-101.

Peters, D. C., R. J. Lederman, et al. (2003). "Undersampled projection reconstruction for active catheter imaging with adaptable temporal resolution and catheter-only views." Magnetic Resonance in Medicine 49(2): 216-222.

Pipe, J. G. (1999). "Motion correction with PROPELLER MRI: Application to head motion and free-breathing cardiac imaging." Magnetic Resonance in Medicine 42(5): 963-969.

Pipe, J. G. and P. Menon (1999). "Sampling density compensation in MRI: Rationale and an iterative numerical solution." Magnetic Resonance in Medicine 41(1): 179-186.

Plaks, V., S. Sapoznik, et al. (2011). "Functional Phenotyping of the Maternal Albumin Turnover in the Mouse Placenta by Dynamic Contrast-Enhanced MRI." Molecular Imaging and Biology 13(3): 481-492.

Puget, S., C. Philippe, et al. (2012). "Mesenchymal Transition and PDGFRA Amplification/Mutation Are Key Distinct Oncogenic Events in Pediatric Diffuse Intrinsic Pontine Gliomas." PLoS ONE 7(2).

Rasche, V., R. Proksa, et al. (1999). "Resampling of data between arbitrary grids using convolution interpolation." Medical Imaging, IEEE Transactions on 18(5): 385-392.

Riederer, S. J., T. Tasciyan, et al. (1988). "MR fluoroscopy: Technical feasibility." Magnetic Resonance in Medicine 8(1): 1-15.

Roemer, P. B., W. A. Edelstein, et al. (1990). "The NMR phased array." Magnetic Resonance in Medicine 16(2): 192-225.

Rose, C. J., S. J. Mills, et al. (2009). "Quantifying spatial heterogeneity in dynamic contrast-enhanced MRI parameter maps." Magnetic Resonance in Medicine 62(2): 488-499.

RSNA, D.-M. T. C. (2012) "Quantitative Imaging Biomarkers Alliance: DCE MRI Quantification. Version 1.0. QIBA, July, 1, 2012. Available from: http://rsna.org/QIBA.aspx."

Rubenstein, J. L., J. Kim, et al. (2000). "Anti-VEGF Antibody Treatment of Glioblastoma Prolongs Survival But Results in Increased Vascular Cooption." Neoplasia 2(4): 306.

Schabel, M. C. and D. L. Parker (2008). "Uncertainty and bias in contrast concentration measurements using spoiled gradient echo pulse sequences." Physics in Medicine and Biology 53(9): 2345.

Scheffler, K. and J. Hennig (1998). "Reduced circular field-of-view imaging." Magnetic Resonance in Medicine 40(3): 474-480.

Schiffman, J. D., J. G. Hodgson, et al. (2010). "Oncogenic BRAF Mutation with CDKN2A Inactivation Is Characteristic of a Subset of Pediatric Malignant Astrocytomas." Cancer Research 70(2): 512-519.

Schwartzentruber, J., A. Korshunov, et al. (2012). "Driver mutations in histone H3.3 and chromatin remodelling genes in paediatric glioblastoma." Nature 482(7384): 226-231.

Song, H. K. and L. Dougherty (2000). "k-Space weighted image contrast (KWIC) for contrast manipulation in projection reconstruction MRI." Magnetic Resonance in Medicine 44(6): 825-832.

Song, H. K. and L. Dougherty (2004). "Dynamic MRI with projection reconstruction and KWIC processing for simultaneous high spatial and temporal resolution." Magnetic Resonance in Medicine 52(4): 815-824.

Sourbron, S. P. and D. L. Buckley (2011). "On the scope and interpretation of the Tofts models for DCE-MRI." Magnetic Resonance in Medicine 66(3): 735-745.

St. Lawrence, K. S. and T.-Y. Lee (1998). "An Adiabatic Approximation to the Tissue Homogeneity Model for Water Exchange in the Brain: I. Theoretical Derivation." J Cereb Blood Flow Metab 18(12): 1365-1377.

Stantz, K., M. Cao, et al. (2011). "Monitoring the Longitudinal Intra-tumor Physiological Impulse Response to VEGFR2 Blockade in Breast Tumors Using DCE-CT." Molecular Imaging and Biology 13(6): 1183-1195.

Stevens, A. J., J. J. Jensen, et al. (2011). "The Role of Public-Sector Research in the Discovery of Drugs and Vaccines." New England Journal of Medicine 364(6): 535-541.

Stollberger, R. and P. Wach (1996). "Imaging of the active B1 field in vivo." Magnetic Resonance in Medicine 35(2): 246-251.

Strouthos, C., M. Lampaskis, et al. (2010). "Indicator dilution models for the quantification of microvascular blood flow with bolus administration of ultrasound contrast agents." Ultrasonics, Ferroelectrics and Frequency Control, IEEE Transactions on 57(6): 1296-1310.

Sturm, D., H. Witt, et al. (2012). "Hotspot Mutations in H3F3A and IDH1 Define Distinct Epigenetic and Biological Subgroups of Glioblastoma." Cancer cell 22(4): 425-437.

Subashi, E., K. R. Choudhury, et al. (2014). "An analysis of the uncertainty and bias in DCE-MRI measurements using the spoiled gradient-recalled echo pulse sequence." Medical Physics 41(3).

Subashi, E., E. J. Moding, et al. (2013). "A comparison of radial keyhole strategies for high spatial and temporal resolution 4D contrast-enhanced MRI in small animal tumor models." Medical Physics 40(2).

Suga, M., T. Matsuda, et al. (1999). "Keyhole method for high-speed human cardiac cine MR imaging." Journal of Magnetic Resonance Imaging 10(5): 778-783.

Sugahara, T., Y. Korogi, et al. (1998). "Correlation of MR imaging-determined cerebral blood volume maps with histologic and angiographic determination of vascularity of gliomas." American Journal of Roentgenology 171(6): 1479-1486.

Sweeney, C. J., K. D. Miller, et al. (2001). "The Antiangiogenic Property of Docetaxel Is Synergistic with a Recombinant Humanized Monoclonal Antibody against Vascular Endothelial Growth Factor or 2-Methoxyestradiol but Antagonized by Endothelial Growth Factors." Cancer Research 61(8): 3369-3372.

Therasse, P., S. G. Arbuck, et al. (2000). "New Guidelines to Evaluate the Response to Treatment in Solid Tumors." Journal of the National Cancer Institute 92(3): 205-216.

Tofts, P. S. (1997). "Modeling tracer kinetics in dynamic Gd-DTPA MR imaging." Journal of Magnetic Resonance Imaging 7(1): 91-101.

Tofts, P. S., G. Brix, et al. (1999). "Estimating kinetic parameters from dynamic contrast-enhanced t1-weighted MRI of a diffusable tracer: Standardized quantities and symbols." Journal of Magnetic Resonance Imaging 10(3): 223-232.

Tofts, P. S. and A. G. Kermode (1991). "Measurement of the blood-brain barrier permeability and leakage space using dynamic MR imaging. 1. Fundamental concepts." Magnetic Resonance in Medicine 17(2): 357-367.

Treier, R., A. Steingoetter, et al. (2007). "Optimized and combined T1 and B1 mapping technique for fast and accurate T1 quantification in contrast-enhanced abdominal MRI." Magnetic Resonance in Medicine 57(3): 568-576.

Van Vaals, J. J., M. E. Brummer, et al. (1993). "“Keyhole” method for accelerating imaging of contrast agent uptake." Journal of Magnetic Resonance Imaging 3(4): 671-675.

Vautier, J., M. Heilmann, et al. (2010). "2D and 3D radial multi-gradient-echo DCE MRI in murine tumor models with dynamic R*2-corrected R1 mapping." Magnetic Resonance in Medicine 64(1): 313-318.

Verdecchia, A., S. Francisci, et al. (2007). "Recent cancer survival in Europe: a 2000–02 period analysis of EUROCARE-4 data." The Lancet Oncology 8(9): 784-796.

Villringer, A., B. R. Rosen, et al. (1988). "Dynamic imaging with lanthanide chelates in normal brain: Contrast due to magnetic susceptibility effects." Magnetic Resonance in Medicine 6(2): 164-174.

Warren, K. (2012). "Diffuse intrinsic pontine glioma: Poised for progress." Frontiers in Oncology 2.

Warren, K. E. (2004). "NMR Spectroscopy and Pediatric Brain Tumors." The Oncologist 9(3): 312-318.

Watson, K. D., X. Hu, et al. (2011). "Novel Ultrasound and DCE-MRI Analyses After Antiangiogenic Treatment With a Selective VEGF Receptor Inhibitor." Ultrasound in Medicine and Biology 37(6): 909-921.

Weidner, N. (1995). "Current pathologic methods for measuring intratumoral microvessel density within breast carcinoma and other solid tumors." Breast Cancer Research and Treatment 36(2): 169-180.

Weis, S. M. and D. A. Cheresh (2011). "Tumor angiogenesis: molecular pathways and therapeutic targets." Nat Med 17(11): 1359-1370.

Weissleder, R. (2006). "Molecular Imaging in Cancer." Science 312(5777): 1168-1171.

Wong, S. T. S. and M. S. Roos (1994). "A strategy for sampling on a sphere applied to 3D selective RF pulse design." Magnetic Resonance in Medicine 32(6): 778-784.

Woutjan, B., V. Brendan, et al. (2010). "Pixel-based subsets for rapid multi-pinhole SPECT reconstruction." Physics in Medicine and Biology 55(7): 2023.

Wu, G. (2012). "Somatic histone H3 alterations in pediatric diffuse intrinsic pontine gliomas and non-brainstem glioblastomas." Nat Genet 44(3): 251-253.

Xiong, J., P. T. Fox, et al. (1999). "The effects of K-space data undersampling and discontinuities in keyhole functional MRI." Magnetic Resonance Imaging 17(1): 109-119.

Yabuuchi, H., T. Fukuya, et al. (2003). "Salivary Gland Tumors: Diagnostic Value of Gadolinium-enhanced Dynamic MR Imaging with Histopathologic Correlation." Radiology 226(2): 345-354.

Yamashita, Y., T. Baba, et al. (2000). "Dynamic Contrast-enhanced MR Imaging of Uterine Cervical Cancer: Pharmacokinetic Analysis with Histopathologic Correlation and Its Importance in Predicting the Outcome of Radiation Therapy." Radiology 216(3): 803-809.

Yankeelov, T. E., J. J. Luci, et al. (2008). "Incorporating the effects of transcytolemmal water exchange in a reference region model for DCE-MRI analysis: Theory, simulations, and experimental results." Magnetic Resonance in Medicine 59(2): 326-335.

Yankeelov, T. E., J. J. Luci, et al. (2005). "Quantitative pharmacokinetic analysis of DCE-MRI data without an arterial input function: a reference region model." Magnetic Resonance Imaging 23(4): 519-529.

Yen, Y.-F., K. F. Han, et al. (2000). "Dynamic breast MRI with spiral trajectories: 3D versus 2D." Journal of Magnetic Resonance Imaging 11(4): 351-359.

Yuan, F., Y. Chen, et al. (1996). "Time-dependent vascular regression and permeability changes in established human tumor xenografts induced by an anti-vascular endothelial growth factor/vascular permeability factor antibody." Proceedings of the National Academy of Sciences 93(25): 14765-14770.

Zahra, M. A., L. T. Tan, et al. (2009). "Semiquantitative and Quantitative Dynamic Contrast-Enhanced Magnetic Resonance Imaging Measurements Predict Radiation Response in Cervix Cancer." International Journal of Radiation Oncology*Biology*Physics 74(3): 766-773.

Zhang, J., G. Wu, et al. (2013). "Whole-genome sequencing identifies genetic alterations in pediatric low-grade gliomas." Nat Genet 45(6): 602-612.

Zhang, Y., H. P. Hetherington, et al. (1998). "A novel k-space trajectory measurement technique." Magnetic Resonance in Medicine 39(6): 999-1004.

Zhi-Pei, L. and P. C. Lauterbur (1994). "An efficient method for dynamic magnetic resonance imaging." Medical Imaging, IEEE Transactions on 13(4): 677-686.

Zhou, X., Z.-P. Liang, et al. (1998). "A fast spin echo technique with circular sampling." Magnetic Resonance in Medicine 39(1): 23-27.

Zhu, X. P., K. L. Li, et al. (2000). "Quantification of endothelial permeability, leakage space, and blood volume in brain tumors using combined T1 and T2* contrast-enhanced dynamic MR imaging." Journal of Magnetic Resonance Imaging 11(6): 575-585.

Zwart, N. R., K. O. Johnson, et al. (2011). "Efficient sample density estimation by combining gridding and an optimized kernel." Magnetic Resonance in Medicine.

Biography

Ergys Subashi

Born

September 30, 1983
Tirana, Albania

Education

Duke University, Durham, NC
Ph.D. Medical Physics, 2014

Worcester Polytechnic Institute, Worcester, MA
B.S. Physics, 2008
Minor in Mathematics

University of Tirana Medical School, Tirana, Albania
Completed first year of medical school, 2004

Scholarly Societies

American Association of Physicists in Medicine, 2009 – Present
International Society for Magnetic Resonance in Medicine, 2011 – Present

Publications

Subashi, E., Cordero, F., Halvorson, K. G., Qi, Y., Becher, O. J., Johnson, G. A. "Tumor Location and Histone H3.3K27M Mutation Significantly Influence the Blood-Brain Barrier Permeability in a Genetic Mouse Model of Pediatric High-Grade Glioma" *Journal of Neuro-Oncology,* Under review.

Subashi, E., Choudhury, K. R., Johnson, G. A. "An Analysis of the Uncertainty and Bias in DCE-MRI Measurements Using the Spoiled Gradient-Recalled Echo Pulse Sequence" *Medical Physics*, **41(3)**, (2014)

Subashi, E., Moding, E. J., Cofer, G. P., MacFall, J. R., Kirsch, D. G., Qi, Y., Johnson, G. A. "A Comparison of Radial Keyhole Strategies for High Spatial and Temporal Resolution 4D Contrast-Enhanced MRI in Small Animal Tumor Models" *Medical Physics*, **40(2)**, (2013)

Badea, C.T., Johnston, S.M., **Subashi, E.**, Qi, Y., Hedlung, L.W., Johnson, G.A., "Lung Perfusion Imaging in Small Animals Using 4D Micro-CT at Heartbeat Temporal Resolution," *Medical Physics,* **37(1),** (2010)

Garcia, R. and **Subashi, E.**, Fukuto, M., "Thin-Thick Coexistence Behavior of 8CB Liquid Crystalline Films on Silicon," *Physical Review Letters,* **100(19)**, (2008)

Garcia, R., Osborne, K., **Subashi, E.**, "Validity of the "Sharp-Kink Approximation" for Water and Other Fluids," *Journal of Physical Chemistry, B,* **112(27)**, (2008).

Conference Proceedings

Xie, L., **Subashi, E.,** Qi, Y., Johnson, G. A. "4D Contrast Enhanced MRI of the Developing Kidney", *International Society for Magnetic Resonance in Medicine Annual Meeting*, Milan, Italy, May 2014.

Subashi, E., Moding, E. J., MacFall, J. R., Kirsch, D. G., Qi, Y., Johnson, G. A. "A Method for Identifying Tumor Sub-Regions with Similar Enhancement Characteristics Based on Volumetric High Resolution DCE-MRI", *International Society for Magnetic Resonance in Medicine Annual Meeting*, Salt Lake City, Utah, April 2013.

Subashi, E., Gewalt, S.L., Cofer, G.P., Qi, Y., Johnson, G.A. "4D Contrast-Enhanced MRI: Functional Imaging of Tumor Microenvironment," *Duke University Radiology/Radiation Oncology Retreat*, Durham, NC, March 2011. **Poster awarded second place for best research.**

Subashi, E., Garcia, R., "Absence of Uniform Nematic Phase for Thin 8CB Films," *The American Physical Society Annual Meeting*, Denver, CO, March 2007.

Subashi, E., Garcia, R., "Water as a Wetting Agent for Liquid Crystal Films," *The American Physical Society Annual Meeting*, Baltimore, MD, March 2006.

Subashi, E., Garcia, R., "Dewetting Mechanism of Thin Liquid Crystal Films," *24th New England Complex Fluids Symposium*, Waltham, MA, September 2005.